



**HAL**  
open science

# Theoretical study of electron collisions with NO<sub>2</sub> and N<sub>2</sub>O molecules for control and reduction of atmospheric pollution

Hainan Liu

► **To cite this version:**

Hainan Liu. Theoretical study of electron collisions with NO<sub>2</sub> and N<sub>2</sub>O molecules for control and reduction of atmospheric pollution. Theoretical and/or physical chemistry. Université Paris-Saclay, 2020. English. NNT: 2020UPAST030 . tel-03153639

**HAL Id: tel-03153639**

**<https://theses.hal.science/tel-03153639>**

Submitted on 26 Feb 2021

**HAL** is a multi-disciplinary open access archive for the deposit and dissemination of scientific research documents, whether they are published or not. The documents may come from teaching and research institutions in France or abroad, or from public or private research centers.

L'archive ouverte pluridisciplinaire **HAL**, est destinée au dépôt et à la diffusion de documents scientifiques de niveau recherche, publiés ou non, émanant des établissements d'enseignement et de recherche français ou étrangers, des laboratoires publics ou privés.

# Theoretical study of electron collisions with NO<sub>2</sub> and N<sub>2</sub>O molecules for control and reduction of atmospheric pollution

**Thèse de doctorat de l'Université Paris-Saclay**

École doctorale n° 573, Approches interdisciplinaires:  
fondements, applications et innovation (INTERFACES)

Spécialité de doctorat: Physique

Unité de recherche: Université Paris-Saclay, CentraleSupélec, CNRS,  
Laboratoire SPMS, 91190, Gif-sur-Yvette, France)

Référent: : CentraleSupélec

**Thèse présentée et soutenue à Gif-sur-Yvette, le 25 novembre  
2020, par**

**Hainan LIU**

## Composition du jury:

<b>Christophe LAUX</b> Professeur, Université Paris Saclay	Président
<b>Alexander ALIJAH</b> Professeur, Université de Reims Champagne-Ardenne, Reims	Rapporteur & Examineur
<b>Zsolt MEZEI</b> Senior Researcher, HDR, Hungarian Academy of Science	Rapporteur & Examineur
<b>Nicolas DOUGUET</b> Maître de Conférences, Kennesaw State University	Examineur
<b>Pietro CORTONA</b> Professeur, Université Paris Saclay	Directeur
<b>Mehdi AYOZ</b> Maître de Conférences, Université Paris Saclay	Coencadrante
<b>Viatcheslav KOKOOLINE</b> Professeur, Université de Floride Centrale	Coencadrante
<b>Samantha FONSECA</b> Maître de Conférences, Rollins College	Invitée



THEORETICAL STUDY OF ELECTRON COLLISIONS WITH NO<sub>2</sub> AND N<sub>2</sub>O MOLECULES  
FOR CONTROL AND REDUCTION OF ATMOSPHERIC POLLUTION

by

HAINAN LIU

A thesis submitted in partial fulfilment of the requirements  
for the degree of Doctor of Philosophy  
in the Laboratory of Structures, Propriétés et Modélisation des Solides (SPMS)  
in CentraleSupélec  
at Université Paris-Saclay

Fall Term  
2020

© 2020 Hainan LIU

## ABSTRACT

This thesis presents theoretical investigations on electron scattering with two polyatomic molecules of atmospheric pollution interest, the  $\text{NO}_2$  and  $\text{N}_2\text{O}$  molecules. Regarding the  $\text{NO}_2$  molecule, we study the vibrational excitation between the lowest levels within the ground electronic states of this molecule. The calculation is carried out by an approach that combines the normal modes approximation for the vibrational states of the  $\text{NO}_2$ , the UK R-matrix code to obtain electron–molecule S-matrix for fixed geometries of the target and the vibrational frame transformation to evaluate the scattering matrices for vibrational transitions. To our knowledge, the vibrational excitation cross section calculated in this thesis is reported for the first time for  $\text{NO}_2$  molecule. The uncertainty estimation of the results is thus performed to validate the present theoretical approach.

Similarly, the vibrational excitation cross sections of  $\text{N}_2\text{O}$  molecule are determined. The obtained results are in reasonable agreement with experimental data. The rate coefficient of vibrational excitation are obtained from the cross-sections for temperatures in the 10–10000 K range. The rotational structure of the target neutral molecules is neglected in the present approach, which implies that the obtained cross-sections and rate coefficients should be viewed as averaged over initial rotational states and summed over final rotational states of the corresponding initial and final vibrational levels.

Finally, the dissociative electron attachment (DEA) of  $\text{NO}_2$  are also studied in this thesis. This process competes with vibrational excitation at the scattering energy range below the first electronic excited state of the target. The DEA cross section is calculated by the method based on the Bardsley-O'Malley theory developed for diatomic molecules and generalized to complex polyatomic molecules by Chi Hong Yuen *et al.* afterwards compared with available experimental measurements. The obtained results could be used in plasma modeling for control and reduction of

atmospheric pollution.

## ACKNOWLEDGMENTS

This project would not have been possible within the period of a PhD thesis without the help of many supporting hands. At this place I wish to thank all who contributed to this work in some way.

In accordance with tradition, I must first thank my parents for their endless love, encouragement, and believing in me throughout the period of the PhD and my life in general. I cannot thank them enough for what they have done for me. I honestly believe that I have the best parents in the world and I will be grateful forever. I am a lucky daughter because you have always been there for me and I am sorry for being miles away from you. The thesis is entirely dedicated to you!

Special thanks should also be given to my supervisors Prof. Cortona and Dr. Ayouz for accepting me as a PhD student in one of the best universities in the world—Université Paris Saclay.

I would like to thank Prof. Cortona for his support, his patience and time in answering my research and daily life questions. Thanks for allowing me to work independently. Thank you for all help, it has been a real pleasure working with you.

I would like to thank Dr. Ayouz for his dedicated guidance over the past three years, his unfailingly good humour, enthusiasm and providing me opportunity to work collaborate with external research groups. Without his encouragement, advice and persistent helps, this dissertation would not have been possible. I appreciate all his contributions of time, patience and ideas to make my PhD experience productive.

I would also like to express the deep appreciation to Prof. Viatcheslav Kokoouline at University of Central Florida, who supervised me in all the projects and during my diploma time. Most of the conclusions obtained in this thesis are entirely due to his help and insights. He has the attitude and the substance of a genius. He always make himself available to help me whenever I needed and

was struggling with the theory.

I am really happy that I was able to go to the United States as a exchange student at Rollins college and work together with Dr. Fonseca and Dr. Douguet. This was one of the most stimulating months in my life. I would like to give my gratitude to them for discussions and assistance during my stays at Rollins college. Also thank all the new friends I got in Orlando for their friendship, hospitality, care during my visit.

Very special thanks must go to Chi Hong Yuen at University of Central Florida. Thanks for his very useful discussions and friendship during my PhD. The dissociative electron attachment work presented here were in collaboration with him. Some of the theory, the conclusions and the observations presented here were his idea. I thank him for allowing me to collaborate with him and to present the work in my thesis.

I also thank SPMS lab for providing me a comfortable working environment and supporting me to attend international research conference. Many thanks to my colleagues who helped me a lot and all of my friends for sharing this experience with me. I apologize to them as I will not try to do a list of them here because it might be very long.

Finally, I'd like to thank my boyfriend, Xianwu, for his love, support and encouragement, in which I found the strength to pull through the most difficult time. Throughout the course of my PhD I always felt I was in safe hands with regards to any matter, no matter how trivial. Without his help, patience and advice, completing this degree would have been a near impossible task. Words cannot describe how lucky I am to have him in my life. I love you, and look forward to our lifelong journey!

I gratefully acknowledge the funding sources that made my PhD work possible. This thesis was supported China Scholarship Council, the Thomas Jefferson Fund of the Office for Science and

Technology of the Embassy of France in the United States and the National Science Foundation, Grant No. PHY-1806915. It has also received funding from the program “Accueil des chercheurs étrangers” of CentraleSupélec and “Séjour à l’étranger 2019” of école doctorale INTERFACES of Université Paris-Saclay.

## TABLE OF CONTENTS

LIST OF FIGURES . . . . .	xi
LIST OF TABLES . . . . .	xx
CHAPTER 1: INTRODUCTION . . . . .	1
CHAPTER 2: THEORETICAL BACKGROUND . . . . .	6
2.1 Target Molecule Properties . . . . .	6
2.1.1 Theoretical methods for solving the electronic Schrödinger equation . . . . .	6
2.1.2 Symmetry point groups . . . . .	13
2.1.3 Normal mode approximation . . . . .	17
2.1.4 Quantum chemistry software . . . . .	20
2.2 Scattering Theory . . . . .	21
2.2.1 General quantum scattering . . . . .	21
2.2.2 R-matrix theory . . . . .	25
2.2.3 Vibrational frame transformation . . . . .	34
CHAPTER 3: CROSS SECTIONS AND RATE COEFFICIENTS FOR VIBRATIONAL	

(DE-) EXCITATION OF NO <sub>2</sub> BY ELECTRON IMPACT . . . . .	39
3.1 Introduction . . . . .	39
3.2 The Properties Of The NO <sub>2</sub> Molecule And Scattering Calculations . . . . .	41
3.3 Cross Sections And Rate Coefficients . . . . .	48
3.4 Uncertainty Estimation . . . . .	57
3.5 Conclusions . . . . .	63
CHAPTER 4: CROSS SECTIONS AND RATE COEFFICIENTS FOR VIBRATIONAL (DE-) EXCITATION OF N <sub>2</sub> O BY ELECTRON IMPACT . . . . .	65
4.1 Introduction . . . . .	65
4.2 Theoretical Approach And Computational Details . . . . .	67
4.3 Renner-Teller Coupling In N <sub>2</sub> O Vibrational Excitation By Electron . . . . .	76
4.4 Cross Sections And Rate Coefficients . . . . .	79
4.5 Uncertainty Estimation . . . . .	82
4.6 Conclusions . . . . .	83
CHAPTER 5: DISSOCIATIVE ELECTRON ATTACHMENT OF NO <sub>2</sub> . . . . .	85
5.1 Introduction . . . . .	85
5.2 Resonance Calculation And Theory of Resonant Capture . . . . .	87

5.3 Results and Discussion . . . . . 93

5.4 Conclusion And Further Works . . . . . 98

CHAPTER 6: CONCLUSION AND PERSPECTIVES . . . . . 99

APPENDIX A: Quantemol-N . . . . . 102

APPENDIX B: Gauss–Legendre quadrature . . . . . 105

APPENDIX C: The simple VE formulation . . . . . 108

APPENDIX D: La synthèse . . . . . 111

LIST OF REFERENCES . . . . . 114

## LIST OF FIGURES

Figure 2.1: Sketch of illustrating the CAS orbital partitions. . . . .	13
Figure 2.2: The symmetry elements of NO <sub>2</sub> . . . . .	15
Figure 2.3: Schematic illustration of the general electron scattering event with spherical symmetric potential. Scattering of waves; incoming plane wave generates outgoing spherical wave. $\theta$ is the scattering angle (the angle between the Z-axis and the direction of the scattered particle). . . . .	22
Figure 2.4: A diagram showing the R-matrix sphere surrounding an NO <sub>2</sub> molecule. Space is separated into the ‘inner’ and ‘outer’ regions by a sphere of radius $a$ . . . . .	27
Figure 3.1: The sketch of three normal modes of NO <sub>2</sub> : bending ( $\nu_1$ ), symmetric stretching ( $\nu_2$ ), and asymmetric stretching ( $\nu_3$ ). The red balls represent the O atoms and the blue balls represent the N atoms. The arrows indicate the force vectors. . . . .	42
Figure 3.2: The uncertainty estimation of NO <sub>2</sub> property calculations using MOLPRO. For example, the numbers in brackets (17e, 12o) indicates the CAS that 17 electrons are kept free in 12 active orbitals . . . . .	44

Figure 3.3: Potential energy curves for the ground electronic state of NO<sub>2</sub> as a function of the (a) bending; (b) symmetric stretching; (c) asymmetric stretching modes. The abscissa axes in the figure represent dimensionless normal coordinates. In each panel, only one mode is varied, while the other modes are kept fixed at their equilibrium positions. Red solid curves are the actual potential energies obtained from the UKRmol suite, while black dashed curves represent energies calculated in the harmonic approximation. Horizontal dashed lines denote energies of vibrational states. . . . . 45

Figure 3.4: The largest value of  $|S_{l'\lambda',l\lambda}|^2$  with respect to all possible allowed combinations of  $l\lambda, l'\lambda'$  as a function of the difference  $\Delta l = l' - l$  for all four singlet irreducible representations (irreps) of the  $e^-$ -NO<sub>2</sub> complex. The lowest value of  $l$  is 0 for <sup>1</sup>A<sub>1</sub>, 1 for <sup>1</sup>B<sub>1</sub> and <sup>1</sup>B<sub>2</sub>, 2 for <sup>1</sup>A<sub>2</sub>. For <sup>1</sup>A<sub>1</sub> (solid red line with circles), the couplings between the  $s$  and  $f$ ,  $s$  and  $g$  partial waves are very small. For <sup>1</sup>B<sub>1</sub> (solid green line with triangles) and <sup>1</sup>B<sub>2</sub> (solid blue line with squares), since  $s$ -wave scattering is forbidden by symmetry, only couplings between  $p, d, f$  and  $g$  partial waves are shown. For <sup>1</sup>A<sub>2</sub> (solid pink line with stars),  $s$  and  $p$  partial wave scatterings are not allowed. . . . . 48

Figure 3.5: The figures show dominant (absolute value squared) elements  $|S_{l'\lambda',l\lambda}|^2$  of the scattering matrix as a function of the electron scattering energy at the NO<sub>2</sub> equilibrium. Black lines: couplings between channels with  $\Delta l = 0$ . Color lines: couplings between channels with  $\Delta l = 1$  . . . . . 49

Figure 3.6: Calculated cross sections as functions of the electron scattering energy for the vibrational excitation of NO<sub>2</sub> being initially in the lowest vibrational state  $v_i = 0$  for the three normal modes (see the text for detailed discussion): (a) cross sections for  $v'_i = 1, 2 \leftarrow v_i = 0$  transitions for bending mode; (b) for symmetric stretching mode; (c) for asymmetric stretching mode. . . . . 50

Figure 3.7: The figure shows dominant (absolute value squared) elements  $|S_{l'\lambda',l\lambda}|^2$  of the scattering matrix as a function of normal coordinate  $q_3$  (asymmetric stretching mode) at 0.3 eV scattering energy. Solid curve: singlet for NO<sub>2</sub> + e<sup>-</sup> system. Dashed curve: triplet for NO<sub>2</sub> + e<sup>-</sup> system. The corresponding symmetry is indicated in parentheses. The numbers indicate different partial waves  $l', \lambda' \leftarrow l, \lambda$ . . . . . 51

Figure 3.8: Comparison between the presently calculated  $v_1 = 0 \rightarrow v'_1 = 1$  cross sections (red curves) for bending mode and that one calculated from Equation (2.61) (green curves) with two normal coordinate values of  $q_1$  at 0.2 and 1 respectively. 52

Figure 3.9: The figures show dominant elements  $S_{l'\lambda',l\lambda}$  of the scattering matrix as a function of normal coordinate  $q_1$  (bending mode) at 0.3 eV scattering energy. Upper figure: S-matrix elements for triplet. Lower figure: S-matrix elements for singlet. Solid curve: the real parts of S-matrix elements. Dashed curve: the imaginary parts of S-matrix elements. The numbers indicate different partial waves  $l', \lambda' \leftarrow l, \lambda$ . . . . . 53

Figure 3.10 The figure shows the derivatives of dominant elements  $S_{l'\lambda',l\lambda}$  versus the normal coordinate  $q_1$  at 0.3 eV scattering energy. Solid curve: the real parts of S-matrix elements. Dashed curve: the imaginary parts of S-matrix elements. The numbers indicate different partial waves  $l', \lambda' \leftarrow l, \lambda$ . . . . . 54

Figure 3.11 Spin- and thermally-averaged rate coefficients for (de-)excitation transitions between the three lowest vibrational states of the bending mode. Vibrational excitations are labeled by  $v_i' \leftarrow v_i$ . Corresponding de-excitations are shown by dashed lines of the same color. The figure also demonstrates the quality of the fit of Equation (3.3): Fitted curves are shown by stars with the same color for each transition. . . . . 55

Figure 3.12 Variation of the computed permanent dipole moment of  $\text{NO}_2$  versus different basis sets (panel (a)) and CAS (panel (b)). CAS1: 7 electrons are kept free in the active space including 7 orbitals; CAS2: 9 electrons are kept free in the active space including 8 orbitals; CAS3: 11 electrons are kept free in the active space including 9 orbitals; CAS4 (CAS used in this work): 13 electrons are kept free in the active space including 10 orbitals; CAS5: 15 electrons are kept free in the active space including 11 orbitals. The blue dashed line indicates the experimental value of the dipole moment. (c) The eigenphase sums of scattering of the  $^3B_1$  symmetry of the  $e^- - \text{NO}_2$  complex as a function of the electron scattering energy for different CAS's. The inset enlarges the region where a sharper energy-dependence is observed around 1.6 eV corresponding to a resonance. . . . . 59

Figure 3.13 The figure compares selected values of the  ${}^1A_1$  scattering matrix elements (absolute value squared) before (solid color lines) and after (dashed lines of the same color) the unitary transformation that eliminates the long-range dipolar coupling between asymptotic channels in the  $e^-$ -NO<sub>2</sub> scattering matrix in the body frame. See the detailed discussion in the text. Each curve is labeled at the left of the figure with the pair of indexes ( $l'\lambda' \leftarrow l\lambda$ ), corresponding to the final channels and initial channel. The results for other irreps are not displayed but the situation is very similar to the  ${}^1A_1$  symmetry. . . . . 62

Figure 4.1: The three normal modes for N<sub>2</sub>O. The red balls represent the O atoms and the blue balls represent the N atoms. The arrows indicate the force vectors. . . . . 68

Figure 4.2: The three axes of the molecular coordinate system are chosen along the principal axes on the inertia of the molecule. . . . . 69

Figure 4.3: The integrands of Equation (2.53) for the NO stretching mode for three among the largest matrix elements  $0,0 \leftarrow 0,0$ ,  $1,1 \leftarrow 1,1$ ,  $2,-2 \leftarrow 2,-2$  as an example. Each figure shows the integrand for one matrix element for three energies 0.3 eV, 0.4 eV and 1.6 eV. . . . . 71

Figure 4.4: Potential energy curves for the ground electronic state of  $\text{N}_2\text{O}$  as a function of the (a) bending, (b) NO stretching and (c) NN stretching normal-mode coordinates. The abscissa axes in the figures represent dimensionless normal mode coordinates. In each panel, only one mode is varied, while the other modes are kept fixed at their equilibrium positions. Red solid curves are the actual potential energies obtained from the R-matrix code, while black dashed curves represent energies calculated in the harmonic approximation, i.e. simply  $\sim \frac{\hbar\omega_i}{2}q_i^2$ . Horizontal dashed lines denote the energies of vibrational states. . . . . 74

Figure 4.5: Sum of eigenphases as a function of the electron scattering energy for equilibrium geometry and displacements  $q_i = \pm 0.8668$  (dimensionless) along each normal mode. Due to the symmetry of bending mode, the eigenphase sum of  $q_1 = +0.8668$  and  $q_1 = -0.8668$  are the same. The curves are color coded according the different symmetries of the  $e^- + \text{N}_2\text{O}$  system. . . . . 75

Figure 4.6: Largest S-matrix elements (absolute value squared,  $|S_{l'\tilde{\lambda}',l\tilde{\lambda}}|^2$ ) computed at the  $\text{N}_2\text{O}$  equilibrium geometry as a function of the scattering energy. Upper panel shows the couplings between channels with  $\Delta l = 0$  in dashed curves. Bottom panel shows the coupling between channels with  $\Delta l = 1$  in solid curves. 76

Figure 4.7: Largest fixed-nuclei S-matrix elements as a function of the bending coordinate  $q_1$ , computed for scattering energy 0.26 eV. The upper (lower) panel shows the real (imaginary) part of the S-matrix elements. Couplings  $l'\tilde{\lambda}' \leftarrow l\tilde{\lambda}$  between different partial waves, represented by real harmonics  $Y_{l,\tilde{\lambda}}$ , are labeled by curves of different colors. . . . . 78

Figure 4.8: Comparison of the present theoretical results with available experimental cross sections for the vibrational  $v_i = 0 \rightarrow v'_i = 1$  excitation of the (a) bending, (b) NO stretching, and (c) NN stretching modes. The experimental results are taken from Hayashi [129, 130] (solid line with circles), Allan and Skalicky [121] (solid line with triangles), and Nakamura [122] (dashed-dotted line). . . . . 80

Figure 4.9: Thermally-averaged rate coefficients for (de-)excitation transitions between the ground and first excited vibrational states of the bending mode (blue curves), NO stretching mode (black curves) and NN stretching mode (red curves). Vibrational (de-)excitations are labeled by  $v'_i \leftarrow v_i$ . To give an idea of the uncertainty of the present results, we also plotted the results of calculations with Model 2 (dotted lines) and Model 3 (thin lines). The three calculations produce curves which are almost indistinguishable in the figure. . 81

Figure 5.1: Schematics of DEA of  $\text{NO}_2(X^2A_1)$  depicting the break up channel  $\text{O}^-(^2P) + \text{NO}(X^2\Pi)$ . The graph shows the molecular potential energy curves as a function of the normal coordinate introduced in Section 2.1.3 (the reason why the abscissa is  $q_2$  will be discussed below). The neutral molecule captures an incoming electron with a certain kinetic energy (red arrow) and the system forms a temporary negative molecular ion  $\text{NO}_2^{-*}(^1,^3B_1)$  that eventually dissociates. It should be noted that the  $\text{NO}_2^{-*}(^3B_1)$  and  $\text{NO}_2^{-*}(^1B_1)$  states have the same dissociation limits.  $q_\varepsilon$  denotes the Frank-Condon point.  $q_E$  denotes the classical turning point and  $q_s$  denotes the stabilization point.  $E$  is total energy and  $\varepsilon$  is incident energy. The nuclei wave function  $\xi(q_2)$  and  $\eta_2(q_2)$  of  $\text{NO}_2^{-*}(^3B_1)$  and  $\text{NO}_2(X^2A_1)$  are illustrated by the green and black dotted curves respectively. . . . . 88

Figure 5.2: The derivative of the eigenphase sums (for  $\text{NO}_2 + e^-$  system) with respect to electron scattering energy for  $^3B_1$  (red curve) and  $^1B_1$  (blue curve) symmetries at equilibrium. The maximum of the derivative is used to obtain the width of the resonance according to Equation (5.4). . . . . 90

Figure 5.3: The capture coordinate determination. Only  $q_2$  normal coordinate is relevant for electron capture process. . . . . 91

Figure 5.4: The anionic potential energy  $U_d$  (green curve), neutral potential energy  $U_n$  (black curve) and  $^3B_1$  resonance energy  $\Delta$  (circles) ( $^1B_1$  in squares) and its linear approximation (red straight line) along  $q_2$  for  $\text{NO}_2$  at  $q_1 = q_3 = 0$ . The first excited electronic state of  $\text{NO}_2$  (pink solid curve) obtained from Quantemol-N is also displayed in this figure. It indicates the DEA process is carried out below the first excited state of the target molecule. . . . . 94

Figure 5.5: The width of the $^3B_1$ (red crosses) and $^1B_1$ (blue triangles) resonances against its position with different values of $q_2$ for $NO_2$ at $q_1 = q_3 = 0$ . Straight lines are the corresponding fitting part using Equation (5.9) . . . . .	95
Figure 5.6: The calculated survival probability of the $^3B_1$ (red curve) and $^1B_1$ (solid curve) resonances with respect to electron scattering energy. . . . .	96
Figure 5.7: Comparison between the experimental DEA cross section for $NO_2$ by Rangwala <i>etal.</i> (red solid curve) and the present theoretical results (black solid curve). . . . .	97

## LIST OF TABLES

Table 2.1: Basis sets used for NO <sub>2</sub> in this thesis. . . . .	9
Table 2.2: Partial correlation table between $C_{\infty v}$ , $C_{2v}$ and $C_s$ . In infinite group $C_{\infty v}$ , Greek capital letters are used to denote the irreducible representation. The superscripts + and – are attached to symbols for representations which are symmetric and antisymmetric with respect to the vertical mirror plane inversion. One-dimensional representations that are symmetric with respect to rotation by $2\pi/n$ about the principal $C_n$ axis are designated $A$ , while those antisymmetric in this respect are designated $B$ in $C_{2v}$ point group. Subscripts 1 and 2 are usually attached to $A$ 's and $B$ 's to designate those which are, respectively, symmetric and antisymmetric with respect to a $C_2$ axis perpendicular to the principle $C_n$ axis, or in the absence of this element, to a $\sigma_v$ plane. Primes and double primes are attached to all letters, when appropriate, to indicate those which are, respectively, symmetric and antisymmetric with respect to horizontal mirror plane $\sigma_h$ . . . . .	16
Table 3.1: Structure and vibrational frequencies of NO <sub>2</sub> obtained in this study and compared with experimental data. $\omega_1$ , $\omega_2$ and $\omega_3$ are the frequencies of bending mode, symmetric stretching mode and asymmetric stretching mode, respectively. The numbers such as (17, 12) in the parentheses indicate 17 electron are kept free in 12 active orbitals. . . . .	43
Table 3.2: Vertical excitation energies (in eV) of NO <sub>2</sub> using CI model at equilibrium geometry . . . . .	46

Table 3.3: Parameters $a_0$ , $a_1$ and $a_2$ of the polynomial $P_{v_i'v_i}^{fit}(x)$ of Equation (3.3) and (3.4) between the three lowest vibrational states of bending mode. The pairs of the final and initial vibrational levels for each normal mode are at the second line in each header of the three tables. The third line in each header gives the threshold energies $\Delta_{v_i'v_i}$ in Equation (3.5). . . . .	56
Table 3.4: Same as Table 3.3 for symmetric stratching mode . . . . .	57
Table 3.5: Same as Table 3.3 for asymmetric stretching mode. The $\Delta v = 1$ transitions for asymmetric stretching mode are forbidden by symmetry. . . . .	57
Table 3.6: Coefficients from the curves fitting $ S_{l'l',l\lambda} ^2 = \beta E^\alpha$ and $ \tilde{S}_{l'l',l\lambda} ^2 = \beta' E^{\alpha'}$ ( $E$ is in eV). . . . .	61
Table 4.1: Energies $\hbar\omega_i$ (in eV) of N <sub>2</sub> O normal modes obtained in the present study and compared with experimental data from Ref. [94]. . . . .	72
Table 4.2: Parameters $a_0$ , $a_1$ and $a_2$ of the polynomial $P_{v_i'v_i}^{fit}(x)$ in Equation (3.3) and (3.4) for transitions between the ground and first vibrational states in each normal mode. We specify the excitation threshold energies $\Delta_{v_i'v_i}$ of Equation (3.5) in the second column. The threshold $\Delta_{v_i'v_i} = 0$ for de-excitation process. . . . .	82

Table 4.3: The explicit characteristics of different Models used in uncertainty estimation for N<sub>2</sub>O. The second row is the basis sets. The numbers on the left side hand in parentheses indicate the number of active electrons. The numbers on the right side hand in parentheses indicate the number of active orbitals. For example, Model 1 means that the calculation is carried out using cc-pVTZ basis set and the CAS is 12 electrons are kept free in 10 active orbitals. . . . . 83

Table B.1: Gauss–Legendre nodes and weights . . . . . 107

## CHAPTER 1: INTRODUCTION

Electron-molecule collisions play a vital role in many active areas of modern research. In atmospheric physics, they occur naturally in the upper atmosphere of the Earth and other planets [1] through auroras [2–5] and lightning [6]. In considering the biological effects of ionising radiation, the majority of energy deposited in cells is found to be channeled into the production of secondary electrons with kinetic energies between 1–20 eV [7]. Along with damage caused directly by the radiation, these energetic electrons can themselves collide with molecules and cause damage to cells and may play a part in genetic mutation [8]. Electron collisions also underlie the development of many plasma-based technologies such as magnetohydrodynamic power generation [9], electron lasers [10, 11], ignition of internal combustion engines [12], as well as plasma etching [13] and thin film deposition [14].

Computer modeling and performance optimization of the plasma environments listed above require a detailed understanding of the relevant electron collision processes occurring in the plasma themselves. At electron impact energies below the molecular ionization limit, some of the especially important processes between electron and neutral molecules are listed<sup>1</sup> here:

Elastic scattering



Rotational excitation



---

<sup>1</sup>Unless otherwise specified AB is a generic polyatomic molecule.

where  $j$  denotes the rotational state of the target.

Vibrational excitation (VE)



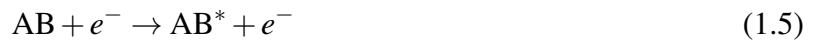
where  $v$  denotes the vibrational state of the target.

Dissociative electron attachment (DEA)



where  $AB^{-*}$  is a temporary negative ion state.

Electronic excitation



where the asterisk denotes an electronically excited state.

The specific data for these reactions needed by researchers are the relevant cross sections. Cross section (denoted by a  $\sigma$  with various subscripts and superscripts) is a measure of the probability for a reaction to occur between two systems and is an energy dependent quantity. It is defined more rigorously in Equation (2.23) of Chapter 2. Since the dynamical description of an ensemble of particles colliding with each other in plasma numerical modeling, such as the direct simulation Monte Carlo (DSMC) method [15] are on the macro-scale, cross-sections are often thermally averaged to give a reaction rate-coefficient. This describes the rate of a process as a function of temperature. The rate-coefficients then offer detailed information about the distribution of each rotational, vibrational and electronic excited state that affect thermodynamics, transport coefficients and ki-

netics of the plasma. For instance, the time-resolved molecular vibrational distribution function (VDF) determines the vibrational-state population of the molecules in non-equilibrium plasma and is important to construct accurate kinetic evolution of the plasma. It relies on the rate constants of vibrational excitations and can be expressed by [16]:

$$\frac{\partial n_v}{\partial t} = n_e \sum_v [\alpha_{v',v} n_{v'} - \alpha_{v,v'} n_v] \quad (1.6)$$

where  $n_e$  is the electron density,  $\alpha_{v,v'}$  is the rate constant for the  $v \rightarrow v'$  vibrational-excitation process.

Besides the academic research and industrial field studies mentioned above, electron-molecule collisions are also important to know more about the mechanism of pollution control using non-equilibrium plasma technology<sup>2</sup> [17–22]. Non-equilibrium plasma is a promising tool for abating environmental pollutants such as nitrogen oxides  $\text{NO}_x$  (  $\text{NO}$ ,  $\text{NO}_2$  ) and nitrous oxide  $\text{N}_2\text{O}$  produced by coal-based power plants which can have detrimental effects on the human respiratory system and the environment. Although the plasma technology can reduce more than 90 %  $\text{NO}_x$  [23], it is still in early stage for commercialization since detailed understanding of how it works is still unavailable. Therefore, providing the accurate cross sections of collisions between low-energy<sup>3</sup> electron and common atmospheric pollutant  $\text{NO}_2$  and  $\text{N}_2\text{O}$  is the major theme of this thesis.

Cross sections can be obtained by theoretically calculating or experimentally measuring. Mainly three experimental branches exist by which electron scattering cross sections can be determined. These are: molecular beam experiments [24, 25] which are specifically powerful tool for investigating electron-molecule differential cross-sections; single collision experiments [26] are used to

---

<sup>2</sup>A non-equilibrium plasma is one in which the mean electron energy, or temperature, is considerably higher than that of the bulk-gas molecules

<sup>3</sup>The low energy region is defined as the incident electron energy below the ionization threshold of the target molecule.

determine total cross sections and also state-specific integral cross sections and differential cross sections; and swarm experiments that can provide very accurate elastic momentum transfer cross sections [27]. The details of these branches are described by Brunger and Buckman [28]. Whilst an experimental measurement could be considered to give the most exact representation of a cross-section or reaction rate-coefficient, it is usually expensive, time consuming and can still produce limitations in the results. For example, the measurements of differential cross-sections using single collision experiments may need to be supplemented in the forwards and backwards scattering regions as these un-accessed parts of the integrand which quite often make a significant contribution to the integral. Experimentalists also have the particular problems in obtaining a unique set of low-energy electron-molecule scattering cross-sections from swarm experiments. Not to mention there are many molecules whose cross sections by electron impact have not been measured, or contradictions exist between the published cross sections. Thus, in order to fill these gaps and supplement or verify the experimental results, theoretical study of cross-sections and reaction rates for processes relevant to pollution abatement are strongly needed.

The main focus of the thesis is theoretical studies of vibrational excitations of  $\text{NO}_2$  and  $\text{N}_2\text{O}$  molecule (see Equation (1.3), (3.1) and (4.1)). Vibrational excitation is specifically important process at the electron impact energy below electronic-excitation thresholds of target molecules. However, sparsity of data of these processes is a great hindrance to nitrogen- and oxygen-containing plasma kinetic modeling. Another process that competes with vibrational excitation but is of particular importance for depollution is dissociative electron attachment (Equation (1.4)), which is considered to be a major route to molecular break-up in cool plasma. In DEA process, specific ionic and neutral fragments are produced by neutral molecules destruction through a resonance state at low energy. If one makes use of the resonances of the electron-molecule system to dissociate  $\text{NO}_x$  directly, then it is possible to significantly reduce the power consumption for pollution control using the non-equilibrium plasma technology. However, theoretical study of DEA process

involving polyatomic molecule is extremely difficult. We will give a brief discuss for DEA of  $\text{NO}_2$  (Equation (5.1)) using a simplified model [29] in this thesis. Other processes such as electronic excitation (Equation(1.5)) will be considered in a near future and we will give an idea on the treatment of those processes.

This thesis will be organized as follows. The next chapter will describe all theory relevant to the calculations presented in this thesis. A general overview of scattering theory will be given in the context of its specific application in one implementation of the R-matrix scattering method [30] provided from the UK polyatomic R-matrix suite [31]. Chapter 3 will compute the cross sections and rate-coefficients for vibrational (de-)excitation of  $\text{NO}_2$  by low-energy electron impact. Chapter 4 will discuss the computation of vibrational excitation of  $\text{N}_2\text{O}$  and the role of Renner-Teller coupling. Finally Chapter 5 will give a brief overview of the model applied to treat the electron attachment of polyatomic molecules and the actual computation of the DEA cross-section of  $\text{NO}_2$ . In Chapter 6. the thesis will conclude with a summary of the results obtained and any future work that could result from the research that was carried out here such as improving the DEA result of  $\text{NO}_2$  and calculating the electronic excitation cross section of  $\text{N}_2\text{O}$ .

## CHAPTER 2: THEORETICAL BACKGROUND

This chapter gives the tools and the theoretical background required to follow the manuscript and analyze the obtained results.

First of all, the Born–Oppenheimer (BO) approximation is used to treat the motion of electrons and nuclei in a target molecule separately. Molecular electronic structure calculations are then carried out with appropriate basis sets and levels of theory. Symmetry rules implemented to simplify the structure calculation is introduced conceptually. On the other hand, the nuclear dynamics, i.e. solving the Schrödinger equation for nuclei is described under the normal modes approximation. These later are obtained from the electronic structure calculations. The practical implementation of the target properties calculation through quantum chemistry software, MOLPRO, is shown in the last part of section 2.1

Section 2.2 is devoted to the scattering part. We present the basic quantum scattering concepts in section 2.2.1 to give a brief idea. Section 2.2.2 gives an introduction to R-matrix theory, which is the most widely used method for electron-molecule collisions in the fixed-nuclei (FN) approximation. To determine the vibrational excitation cross sections, section 2.2.3 introduces the theory of vibrational frame transformations.

### 2.1 Target Molecule Properties

#### *2.1.1 Theoretical methods for solving the electronic Schrödinger equation*

All molecular properties are, in principle, calculable by solving the Schrödinger equation for the molecule. Because of the great mathematical difficulties involved in solving the molecular

Schrödinger equation, one must make the Born–Oppenheimer approximation in which it is supposed that the nuclei, being so much heavier than an electron, move relatively slowly and may be treated as stationary while the electrons move in their field. We can therefore think of the nuclei as being fixed at arbitrary locations, and then solve the Schrödinger equation for electrons alone, viz.,

$$\hat{H}_{el}\psi = E\psi \quad (2.1)$$

The electronic energy  $E$  is usually referred as *potential energy surface*  $U$  (a function of the molecular geometry) because it provides the potential for nuclear motion equation (see Equation (2.10)). It forms the central concept in the application of the electronic structure methods to the study of molecular structures, properties, and reactivities [32].

In fact, it's hard to obtain the solution of electronic Schrödinger equation (2.1) for many-electron systems. Hence a simpler, albeit more approximate method has been adopted whereby the individual electrons could be separated (the many-electron wave function  $\psi$  would be a product of one electron wave function  $\phi_i$ ), and the one-electron wave functions, i.e. Molecular orbitals (MOs) are constructed from linear combination of the basis functions, conventionally called atomic orbitals (MOs = LCAO, Linear Combination of Atomic Orbitals),

$$\phi_i = \sum_j c_{ij}g_j, \quad (2.2)$$

where  $c_{ij}$  is combination coefficient. The set of functions usually refers to the *basis set*. There are two types of basis functions usually employed in molecular orbital calculations: Slater Type Orbitals (STOs) and Gaussian Type Orbitals (GTOs). STOs come from hydrogen-like wave function. With STOs one can obtain the best possible representation of the molecular orbitals as STOs reproduce more the interaction between electron and molecule. However, most quantum chemistry calculations use Gaussian functions as the basis functions which provide an approximation of

the more accurate Slater type orbitals (STOs) and are more numerically efficient to compute. A primitive set of GTOs is written as,

$$g_j^{abc} = N_{abc} x^a y^b z^c e^{-\alpha r^2}, \quad (2.3)$$

where

$$r^2 = x^2 + y^2 + z^2, \quad (2.4)$$

$x$ ,  $y$  and  $z$  are Cartesian coordinate of electrons and  $N_{abc}$  is a normalization constant. Here  $a, b, c$  are not quantum number, but simply the integral exponents. The sum of the exponents is used analogously to the angular momentum quantum number for atoms. When  $a + b + c = 0$ , the GTO is called an s-type Gaussian, when  $a + b + c = 1$ , p-type, when  $a + b + c = 2$ , d-type and so on.  $\alpha$  is known as the orbital exponent which controls the width of the orbital (large  $\alpha$  gives tight function, small  $\alpha$  gives diffuse function) and could be either optimized variationally or by fitting the GTO to an STO. A basis set is therefore built out of a linear combination of different primitive Gaussians centered on the same atom and having different values of  $\alpha$  which is known as contracted Gaussians.

Many Gaussian basis sets have been devised in molecular calculations. Some of the most widely used are the basis sets devised by Pople and co-workers [33]. These basis sets include the STO-3G, 3-21G, 3-21G\*, 6-31G\*, 6-31G\*\*, etc., where the numbers and symbols are related to the number of basis functions on each atom. For example, an STO-3G basis set is that an atomic orbital (a single STO) is described by the linear combination of 3 primitive Gaussian functions (Equation (2.3)). And the correlation consistent basis sets (such as cc-pVDZ, cc-pVTZ, cc-pVQZ, ...) devised by Dunning and co-workers [34] are also widely used. For details of these basis sets, see Levine [35], Section 15.4.

One should also note that the more atomic orbitals we allow into our basis, the closer our basis will come to ‘spanning’ the true molecular orbital space. The quality of a result can therefore be assessed by running calculations with an increasingly larger basis set. The basis sets (in MOLPRO style) for N and O atoms used in this thesis are listed in Table 2.1. Using an uncontracted atomic

Table 2.1: Basis sets used for NO<sub>2</sub> in this thesis.

Basis set	N	O
cc-pVDZ	$9s4p1d \rightarrow 3s2p1d$	$9s4p1d \rightarrow 3s2p1d$
DZP	$9s5p1d \rightarrow 4s2p1d$	$9s5p1d \rightarrow 4s2p1d$
6-311G*	$11s5p1d \rightarrow 4s3p1d$	$11s5p1d \rightarrow 4s3p1d$
cc-pVTZ	$10s5p2d1f \rightarrow 4s3p2d1f$	$10s5p2d1f \rightarrow 4s3p2d1f$
cc-pVQZ	$12s6p3d2f1g \rightarrow 5s4p3d2f1g$	$12s6p3d2f1g \rightarrow 5s4p3d2f1g$

basis set as the starting point for the development of contracted versions suitable for the treatment of molecular systems is common practice. In Table 2.1, the uncontracted basis sets are specified on the left hand side of the arrow and the resulting contracted versions are on the right hand side of the arrow. If proper care is taken during the contraction process, calculations using the contracted basis sets can be performed with similar accuracy but dramatically reduced computational cost.

If the individual electron is assumed moving in a mean field of all other electrons and the overall wave function is antisymmetric (change sign upon swapping any two electrons), it is convenient to express the many-electron wave function  $\psi$  of Equation (2.1) as a Slater determinant,

$$\psi_{\text{HF}} = \frac{1}{\sqrt{N!}} \begin{vmatrix} \phi_1(1) & \phi_2(1) & \cdots & \phi_N(1) \\ \phi_1(2) & \phi_2(2) & \cdots & \phi_N(2) \\ \vdots & \vdots & \ddots & \vdots \\ \phi_1(N) & \phi_2(N) & \cdots & \phi_N(N) \end{vmatrix} \quad (2.5)$$

where  $N$  is the total number of electrons and spin-orbitals  $\phi_i$  are orthonormal. The electronic

energy can therefore be obtained by calculating the expectation values of electronic Hamiltonian over Slater determinants (electronic states),

$$E_{\text{HF}} = \frac{\langle \Psi_{\text{HF}} | \hat{H}_{el} | \Psi_{\text{HF}} \rangle}{\langle \Psi_{\text{HF}} | \Psi_{\text{HF}} \rangle}. \quad (2.6)$$

Having selected a basis set (2.2) to construct a determinant as an initial trial wave function, the variational principle can be used to derive the *Hartree-Fock* (HF) equation,

$$\hat{F}_i \phi_i = \varepsilon_i \phi_i, \quad (2.7)$$

by minimizing the energy of Equation (2.6). Here  $\varepsilon_i$  is the eigenenergy of the fock operator  $\hat{F}_i$  for  $i^{\text{th}}$  MO. The thorough mathematics and proofs are given by Roothaan [36]. This equation states that the MOs which give the ground state are all eigenfunctions of the Fock operator,

$$\hat{F}_i = \hat{h}_i + \sum_j^N (\hat{J}_j - \hat{K}_j). \quad (2.8)$$

The Fock operator is an effective one-electron energy operator, describing the kinetic energy of an electron and the attraction to all the nuclei ( $\hat{h}_i$ ), as well as the repulsion to all the other electrons (via the  $\hat{J}$  and  $\hat{K}$  operators). The eigenvalues of Equation (2.7),  $\varepsilon_i$  are the orbital energies. An iterative procedure is used to solve the HF equation until the set of  $\phi_i$  and  $\varepsilon_i$  agree (when 2 successive values of  $\varepsilon_i$  are small than a fixed value  $1 \times 10^{-7}$  in MOLPRO), that is, a self-consistent field has been achieved. This method is the Hartree Fock self-consistent field (HFSCF) method.

However, the HF wave function is usually considered to contain no electron correlation effects because electrons in HF model do not instantaneously interact with each other, as they do in reality. Each electron only interacts with the average, or mean, field created by all other electrons. The difference between the exact (non-relativistic) energy and the HF energy (calculated with a complete

basis),  $E_{\text{corr}} = E_{\text{exact}} - E_{\text{HF}}$ , is thus defined as the *correlation energy*. A distinction is sometimes made between dynamic, and non-dynamic or static correlation energy. Dynamic correlation energy is the energy to keep the electrons sufficiently far apart. Classically speaking, each electron moves in a way so that it avoids locations in a close proximity to the instantaneous positions of all other electrons. The failure of the HF model to correctly reproduce such motion of electrons is the first source of  $E_{\text{corr}}$ . This type of correlation is called *dynamic correlation* since it is directly related to electron dynamics. Another reason why  $E_{\text{HF}}$  may differ from  $E_{\text{exact}}$  is that there are additional (near-)degenerate configurations which contribute strongly to the nature of the wave function. The wave function in the HF model with single Slater determinant would give a poor representation in that case. Since this kind of correlation is not related to electron dynamics, it is usually called as the *static correlation*, or non-dynamic correlation. More details about electron correlation can be found in Section 5.4.1 of Ref. [37] for example.

It is therefore clear that the HF model is of limited accuracy to describe the target properties due to the neglect of the electron correlation. Nowadays, HF is mainly used as a starting point for correlated wave-function method. Of the correlated methods, the Configuration Interaction (CI) treatment is the conceptually simplest one. The correlation effects can be taken into account by constructing the wave function as a linear combination of multiple determinants, i.e.,

$$\psi_{\text{CI}} = \sum_i a_i \psi_i = a_0 \psi_{\text{HF}} + \sum_{i=1} a_i \psi_i, \quad (2.9)$$

where the coefficients  $a_i$  reflect the weight of each determinant in the expansion and also ensure normalization. Each Slater determinant  $\psi_i$ , or spin-adapted *Configuration State Functions* (CSFs) is typically constructed from Hartree-Fock orbitals such that  $\psi_0$  is the ground-state Hartree-Fock determinant of Equation (2.5). Depending on how many electrons are "excited" out of the HF configuration at a time, we have single, double, triple,... excitation in the CI description. The total

number of determinants that can be generated depends on the size of the basis set: The larger the basis, the more virtual (unoccupied) MOs, and the more excited determinants can be constructed. If all possible determinants in a given basis set are included, all the electron correlation (in a given basis) is (or can be) recovered. This method is called Full CI. It is the most complete solution to the Schrödinger Equation (2.1) but can be applied to only the smallest systems in practice.

The correlation method used in the present thesis is Multi Configuration Self Consistent Field (MCSCF) method. It can be considered as a CI method where one optimises both the coefficients in front of the different configurations in Equation (2.9) and the MOs of Equation (2.2) for each determinant. The MCSCF optimization is iterative like the SCF procedure and is believed to be “sufficiently” accurate for most of the interesting properties of a chemical system. If the number of determinants or CSFs used in the expansion are defined by dividing the orbitals into the subspaces drawn in Figure 2.1, we have a Complete Active Space Self Consistent Field (CASSCF) wavefunction, which has been popularized by Roos *et al.* [38]. The CASSCF is the most commonly applied MCSCF method. The doubly occupied core orbitals constitute the inactive space. Typically, the active space consists of some of the highest occupied orbitals and lowest unoccupied orbitals (virtual orbitals) from an HF calculation. Within this orbital space, a full-CI expansion is considered. The MOs to include in the active space must be decided manually, by considering the problem at hand and the computational expense.

The methods described so far consider only CSFs generated by exciting electrons from a single determinant. This corresponds to have an HF type wave function as the reference. However, an MCSCF wave function may also be chosen as the reference. In that case, excitation of one or two electrons out of all the determinants that enter the MCSCF are involved, defining the Multi-Reference Configuration Interaction (MRCI) method. Compared with the single-reference CI, the number of configurations is increased by a factor roughly equal to the number of configurations included in the MCSCF. MRCI can generate very accurate wave functions, but are also computa-

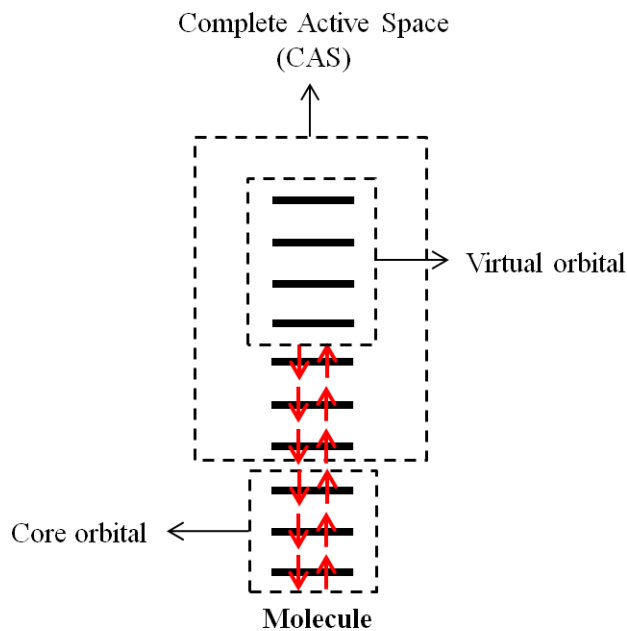


Figure 2.1: Sketch of illustrating the CAS orbital partitions.

tionally very intensive.

Methods that include electron correlation require a multi-determinant wave function, since HF is the best single-determinant wave function. Multi-determinant methods are computationally much more involved than the HF model, but can generate results that systematically approach the exact solution of the Schrödinger equation. Note that “exact” in this context is not the same as the experimental value, because the relativistic effects are neglected.

### 2.1.2 Symmetry point groups

An important tool in setting up an electronic structure calculation and interpreting the results is symmetry. The symmetry of a molecule is most easily described by using one of the standard designations like  $C_{2v}$ ,  $C_{\infty v}$ ,  $C_s$ , etc., which are used in various places in this thesis. These are

called *point groups*. The classification is according to the presence of symmetry elements and corresponding symmetry operations. Excellent expositions of symmetry are given by Levine [35] for example.

A symmetry operation transforms an object into a position that is physically indistinguishable from the original position and preserves the distances between all pairs of points in the object. Typical symmetry operations include rotations ( $\hat{C}_n$ ), reflections ( $\hat{\sigma}$ ), and inversions ( $\hat{i}$ ). A symmetry element is a geometrical entity with respect to which a symmetry operation is performed such as the line ( $C_n$ ), plane ( $\sigma$ ), or point ( $i$ ). The “hat” distinguishes symmetry operations from symmetry elements. For instance, a rotation  $\hat{C}_n$  (a symmetry operation) is carried out around an axis  $C_n$  (the corresponding symmetry element) by  $2\pi/n$  degrees, where  $n$  is an integer. And the inversion operation ( $\hat{i}$ ) moves a point at  $(x, y, z)$  to  $(-x, -y, -z)$  along origin  $i$ . We shall see that we can classify molecules by identifying all their symmetry elements, and grouping together molecules that possess the same set of symmetry elements.

A molecule whose symmetry elements are a  $C_n$  axis (where  $n$  can be 2 or 3 or 4 or . . .) and  $n$  planes of symmetry that each containing the  $C_n$  axis belongs to the point group  $C_{nv}$ . The  $v$  stands for “vertical.” A vertical symmetry plane (symbol  $\sigma_v$ ) is one that contains the highest-order axis of symmetry of the molecule. The  $\text{NO}_2$  molecule has symmetry elements: a  $C_2$  axis and two planes of symmetry that contain this axis (see Figure 2.2), so its point group is  $C_{2v}$ . The symmetry operations of  $\text{NO}_2$  are  $\hat{E}$ ,  $\hat{C}_2(z)$ ,  $\hat{\sigma}(xz)$ , and  $\hat{\sigma}(yz)$ .

In a linear molecule with no center of symmetry (for example,  $\text{N}_2\text{O}$ ), the molecular axis is a  $C_\infty$  axis, since rotation about this axis by any angle is a symmetry operation. Also, any plane that contains the molecular axis is a symmetry plane, and there are infinite number of such vertical symmetry planes. Hence linear molecules with no center of symmetry belong to group  $C_{\infty v}$ .

A molecule with only a symmetry plane (molecular plane) belongs to  $C_s$ . Such as the asymmetry

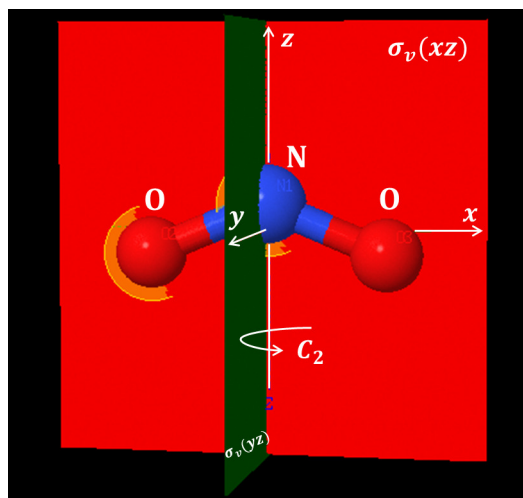


Figure 2.2: The symmetry elements of  $\text{NO}_2$  .

stretching mode of  $\text{NO}_2$  (see Figure 3.1) and bent shape of  $\text{N}_2\text{O}$  at bending mode (see Figure 4.1).

The symmetry operations are  $\hat{E}$  and  $\hat{\sigma}$ .

Each of the symmetry operations mentioned above can be described by a matrix in group theory [39]. A set of matrices that can be combined among themselves in a manner parallel to the way in which a group of symmetry operations combination is defined as the *group representation*. Each representation can be split into a sum of *irreducible representations* in a unique way (irreducible means it cannot be deconstructed into smaller representations), and one of the most important ways of studying a finite group is to find all its irreducible representations. Partial correlation of irreducible representation for  $C_{\infty v}$ ,  $C_{2v}$ , and  $C_s$  point groups is shown in Table 2.2. It should be noted that the complete correlations to an infinite group are not possible, because there are infinite number of irreducible representations.

*Irreducible representation* is used in discussing the symmetry of wave functions. For example, each electronic state of  $\text{NO}_2$  can be classified as belonging to one of the irreducible representations  $A_1$  ,  $A_2$  ,  $B_1$  , or  $B_2$  of the  $C_{2v}$  point group. Recall that atomic terms ( $^1S$ ,  $^3P$ , etc.) are

Table 2.2: Partial correlation table between  $C_{\infty v}$ ,  $C_{2v}$  and  $C_s$ . In infinite group  $C_{\infty v}$ , Greek capital letters are used to denote the irreducible representation. The superscripts  $+$  and  $-$  are attached to symbols for representations which are symmetric and antisymmetric with respect to the vertical mirror plane inversion. One-dimensional representations that are symmetric with respect to rotation by  $2\pi/n$  about the principal  $C_n$  axis are designated  $A$ , while those antisymmetric in this respect are designated  $B$  in  $C_{2v}$  point group. Subscripts 1 and 2 are usually attached to  $A$ 's and  $B$ 's to designate those which are, respectively, symmetric and antisymmetric with respect to a  $C_2$  axis perpendicular to the principle  $C_n$  axis, or in the absence of this element, to a  $\sigma_v$  plane. Primes and double primes are attached to all letters, when appropriate, to indicate those which are, respectively, symmetric and antisymmetric with respect to horizontal mirror plane  $\sigma_h$ .

$C_{\infty v}$	$C_{2v}$	$C_s$
$\Sigma^+$	$A_1$	$A'$
$\Pi$	$B_1 \oplus B_2$	
$\Sigma^-$	$A_2$	$A''$
$\Pi$	$B_1 \oplus B_2$	

specified by giving the spin multiplicity  $2S + 1$  (where  $S$  is the total spin angular momentum quantum number) as a left superscript on the letter ( $S, P, D, \dots$ ) specifying the total electronic orbital angular momentum. A molecular electronic term is specified by giving the spin multiplicity as a left superscript on the irreducible representation such as  $^1A_1, ^3A_1, ^1B_1$ , etc.

In addition, each MO of a molecule can be classified according to one of the irreducible representations of the molecular point group. Lowercase letters are used for the symmetry species of MOs. The MOs belonging to a given symmetry species are numbered in order of increasing orbital energy. For example, the lowest MOs of  $\text{NO}_2$  are labeled as  $1a_1, 2a_1, 1b_2$ , etc. The electron configuration of a molecule is specified by giving the number of electrons in each shell, where a shell is a set of MOs with the same energy. Using group theory, the solution of the Hartree-Fock equation is considerably simplified since it enables one to deal separately with MOs of different symmetry species.

### 2.1.3 Normal mode approximation

Most of this chapter deals with the electronic Schrödinger Equation (2.1) for molecule, but this section will examine the nuclear motion of polyatomic molecules. After finding the electronic energy  $E$  of Equation (2.1) by BO approximation, one could formulate and solve a Schrödinger Equation for nuclear motion, using it as the potential energy  $U$  ( $U$  also includes the energy of nuclear repulsion) for nuclear motion<sup>1</sup>.

In the case of polyatomic molecules, if we expand the potential energy  $U$  in a multi-dimensional Taylor expansion truncated at second order around equilibrium, the nuclear Schrödinger equation for an  $N$  atom system is given by

$$\left[ -\sum_i^{3N} \frac{\hbar^2}{2m_i} \frac{\partial^2}{\partial x_i^2} + \frac{1}{2} (\mathbf{x} - \mathbf{x}_{eq})^T \frac{d^2 U}{d\mathbf{x}^2} (\mathbf{x} - \mathbf{x}_{eq}) \right] \Xi(\mathbf{x}) = E_{nuc} \Xi(\mathbf{x}). \quad (2.10)$$

Where  $N$  is the number of atoms,  $m_i$  is the atomic mass,  $\mathbf{x}$  is the vector of atomic coordinates (N atoms each with coordinates  $(x, y, z)$  can be represented by a single vector of  $3N$  coordinates  $\mathbf{x} = \{x_1 x_2 x_3 \cdots x_{3N}\}$ ),  $\mathbf{x}_{eq}$  defines the equilibrium structure, and  $\Xi(\mathbf{x})$  is the nuclear wave function.

While Equation (2.10) has a well-defined potential energy function, it is quite difficult to solve it in the indicated coordinates. If we use the mass-weighted coordinates,

$$\tilde{x}_i = \sqrt{m_i} (x_i - x_{eqi}) \Rightarrow \frac{\partial^2}{\partial \tilde{x}_i^2} = \frac{1}{m_i} \frac{\partial^2}{\partial x_i^2}, \quad (2.11)$$

Equation (2.10) can now be written as

$$\left[ -\sum_i^{3N} \frac{\hbar^2}{2} \frac{\partial^2}{\partial \tilde{x}_i^2} + \sum_{i,j}^{3N} \frac{1}{2} \mathcal{H}_{ji} \tilde{x}_i \tilde{x}_j \right] \Xi(\tilde{\mathbf{x}}) = E_{nuc} \Xi(\tilde{\mathbf{x}}). \quad (2.12)$$

---

<sup>1</sup>We could also add non BO coupling to improve BO approximation Schrödinger equation

where  $\mathcal{H}_{ij}$  is defined as the *mass – weighted Hessian*

$$\mathcal{H}_{ij} = \frac{1}{\sqrt{m_i}\sqrt{m_j}} \frac{\partial^2 U}{\partial x_i \partial x_j}. \quad (2.13)$$

If we find a matrix  $\mathbf{D}$  that diagonalizes the mass-weighted Hessian, yielding eigenvalues  $\omega_i^2$  [40] and eigenvectors  $\mathbf{Q}$ , Equation (2.12) can be rewritten in diagonal form as

$$\left[ -\sum_i^{3N} \frac{\hbar^2}{2} \frac{\partial^2}{\partial Q_i^2} + \frac{1}{2} \mathbf{Q}^T (\mathbf{D}^{-1} \mathcal{H} \mathbf{D}) \mathbf{Q} \right] \Xi(\mathbf{Q}) = E_{nuc} \Xi(\mathbf{Q}). \quad (2.14)$$

That is,

$$\left[ -\sum_i^{3N} \frac{\hbar^2}{2} \frac{\partial^2}{\partial Q_i^2} + \sum_i^{3N} \frac{1}{2} \omega_i^2 Q_i^2 \right] \Xi(\mathbf{Q}) = E_{nuc} \Xi(\mathbf{Q}). \quad (2.15)$$

The new set of coordinate  $\mathbf{Q}$  is defined by the linear combination of the mass-weighted Cartesian coordinates as  $\mathbf{Q} = \mathbf{D}^T \tilde{\mathbf{X}}$ . Clearly, the kinetic energy operator is still diagonal in these coordinates, and the  $3N$ -dimensional Schrödinger equation (2.10) can therefore be separated into  $3N$  uncoupled one-dimensional Schrödinger equations which are just in the form of a standard harmonic oscillator<sup>2</sup> with unit mass. For a nonlinear molecule composed of  $N$  atoms, there should be  $3N - 6$  ( $3N - 5$  for a linear molecule) nonzero eigenvalues  $\omega_i^2$  of the Hessian matrix, providing the normal, or fundamental, frequencies of vibration [41]. The associated eigenvectors  $\mathbf{Q}$  are the *normal coordinates*<sup>3</sup> of vibration *normal modes* of the molecule, which give the directions and relative amplitudes of the atomic displacements in each mode.

Generally, it is convenient to introduce the dimensionless normal coordinate  $q_i = Q_i \sqrt{\frac{\omega}{\hbar}}$  which will be used later in our calculation. The normal mode Hamiltonian in Equation (2.15) can thus be

---

<sup>2</sup>Hamiltonian for a one-dimensional harmonic oscillator is  $\hat{H}(x) = -\frac{\hbar^2}{2m} \frac{\partial^2}{\partial x^2} + \frac{1}{2} m \omega^2 x^2$ , where  $m$  stands for the molecular mass and  $\omega = \sqrt{\frac{k}{m}}$  is, in classical mechanics, the characteristic frequency of the oscillations.  $k$  is the force constant, i.e., the second derivative of the energy with respect to  $x$  at  $x_{eq}$  in the present case.

<sup>3</sup> $\mathbf{Q} = \{Q_1, Q_2, Q_3 \dots\}$ , corresponding to different modes

written in a neater expression

$$\hat{H}(\mathbf{q}) = \frac{\hbar\omega_i}{2} \left( -\sum_i^{3N} \frac{\partial^2}{\partial q_i^2} + \sum_i^{3N} q_i^2 \right). \quad (2.16)$$

The nuclear energy, in other words the vibrational energy of a polyatomic molecule is then approximately the sum of  $3N - 6$  or  $3N - 5$  (linear molecules) uncoupled harmonic-oscillator energies,

$$E_{nuc} \approx \sum_i^{3N-6(5)} \left( v_i + \frac{1}{2} \right) \hbar\omega_i. \quad (2.17)$$

Where  $\omega_i$  is the frequency of the  $i^{th}$  normal mode and  $v_i$  is its quantum number. For the ground vibrational level  $v_i$  equals zero and has the zero-point energy  $\frac{1}{2}\hbar\omega_i$  (anharmonicity neglected). The nuclear wave function being a product of harmonic oscillator functions,

$$\Xi(\mathbf{q}) = \prod_i^{3N-6(5)} \eta_{v_i}(q_i), \quad (2.18)$$

where the harmonic vibrational function  $\eta_{v_i}$  with  $v_i$  quanta can be expressed as

$$\eta_{v_i}(q_i) = \left( \frac{1}{\pi} \right)^{\frac{1}{4}} \frac{1}{\sqrt{2^{v_i} v_i!}} e^{-\frac{q_i^2}{2}} H_{v_i}(q_i). \quad (2.19)$$

$H_{v_i}$  in Equation (2.19) is the Hermite polynomial. Thus the wave function of the ground vibrational state is

$$\eta_{v_i=0}(q_i) = \left( \frac{1}{\pi} \right)^{\frac{1}{4}} e^{-\frac{q_i^2}{2}}. \quad (2.20)$$

The normal mode approximation is accurate for the lower vibrational levels. As  $v_i$  increases, the nuclei spend more time in regions far from their equilibrium separation. For such regions the potential energy deviates substantially from that of a harmonic oscillator and the harmonic-oscillator approximation becomes poor.

In a words, the main goal of electronic calculation of target is to compute the molecular properties (such as equilibrium geometry and permanent dipole moments), normal mode frequency  $\omega_i$  and Hessian Equation (2.13) needed in the molecular motion section.

#### 2.1.4 Quantum chemistry software

In practice, we use the quantum chemistry software-MOLPRO [42,43] to compute the target properties. MOLPRO is an *ab initio* and density functional program designed for highly accurate calculations on small- and medium-size molecules and includes electron-correlation methods. Its execution is controlled by an input file. In general, each input record begins some keywords containing the basic information of geometry specification, symmetry, basis set, calculation method, etc. For full details about each command, consult the MOLPRO users manual [44]. The tools implemented in properties calculation of NO<sub>2</sub> and N<sub>2</sub>O are described in later Section 3.2 and Section 4.2.

The first step of structure calculation usually is the geometry optimization. A very efficient way to find the equilibrium geometry involves calculating the derivatives of the electronic energy with respect to each of the nuclear coordinates (this set of derivatives is called the energy gradient) for an initially guessed geometry. One then uses the values of these derivatives to change the nuclear coordinates to new values that are likely to be closer to the equilibrium geometry, and one then calculates the wave function, energy, and energy gradient at the new geometry. This process is repeated until the components of the energy gradient are all very close to zero, indicating that the energy minimum has been found. After a geometry optimization, harmonic vibrational frequencies  $\omega_i$  and normal modes  $Q_i$  can be obtained by diagonalizing the Hessian matrix (2.13) mentioned in Section 2.1.3 which is related to the coefficient of the restoring force  $k$ . It should be noted that normal mode frequencies should be calculated at the same level (e.g. CASSCF/cc-pVTZ, ...)

as used for the geometry optimization because accurate calculation of the curvature of the PES at a stationary point requires that the second derivatives (Hessian matrix 2.13) be found at the same level as used to create the surface on which the point sits. Obviously, the output results of interest here are the equilibrium geometry and harmonic frequency (see Table 3.1 as an example). Good agreement between those results and corresponding experimental data are the most important criterion for accurate description of the target molecule structure.

Another important indicator for the efficacy of structure calculation is the permanent dipole moment of target molecule. It is a measure of asymmetry in the molecular charge distribution and can be evaluated via an expectation value of the wavefunction over the dipole moment operator  $\hat{\mu}$  in MOLPRO:

$$\mu = \frac{\langle \psi | \hat{\mu} | \psi \rangle}{\langle \psi | \psi \rangle}. \quad (2.21)$$

It is easy to evaluate this equation once the electronic wavefunction  $\psi$  is known. Therefore, the most important thing is to get a reasonably accurate approximation to  $\psi$  using the appropriate basis set and method as introduced in Section 2.1.1.

## 2.2 Scattering Theory

### 2.2.1 General quantum scattering

Since the electronic structure and vibrational levels of the target molecule can be obtained by tools introduced in Section 2.1, the following content will be devoted to the scattering part. Scattering events can occur between different kinds of particles. In this thesis, we have considered scattering between a low-energy electron and neutral molecules ( $\text{NO}_2$  and  $\text{N}_2\text{O}$ ) in the vibrational

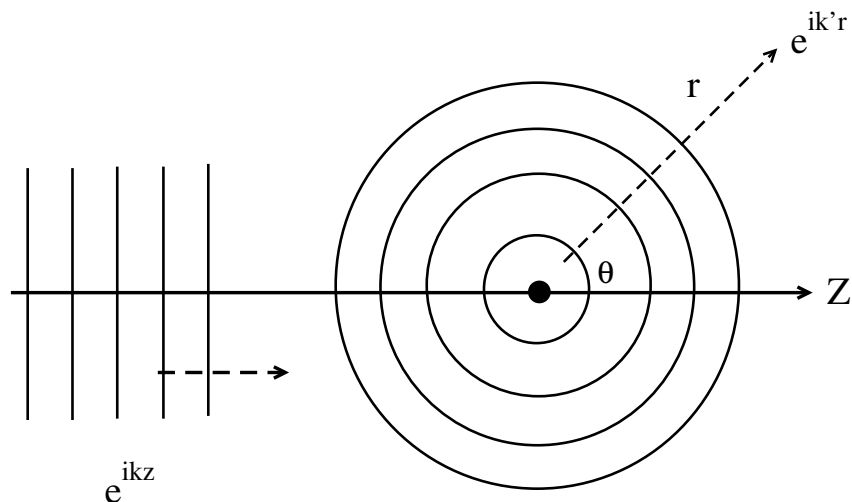


Figure 2.3: Schematic illustration of the general electron scattering event with spherical symmetric potential. Scattering of waves; incoming plane wave generates outgoing spherical wave.  $\theta$  is the scattering angle (the angle between the Z-axis and the direction of the scattered particle).

(de-)excitation and DEA studies. First of all, it is necessary to briefly remind some basic concepts of general quantum scattering to know more about the scattering part. Detailed derivation can be found in Refs. [45, 46] for example.

For simplicity, consider a short-range spherical interaction potential  $U(r)$ , where  $r$  now denotes the radial distance between the electron and the target, the scattering processes between an incoming electron and a molecular target can be shown schematically in Figure 2.3. The entry channel consists of the target in its initial state and an incoming electron with wave number  $\mathbf{k}$  traveling along the collision axis. The exit channel can be the target in its final state and the electron traveling with a different wave number and in a direction  $\mathbf{k}'$ . At large  $r$ , the scattered wave function should consist of an incoming plane wave in the entrance channel  $i$  and outgoing spherical waves in the energetically available exit channels  $j$ . If the incoming plane wave is taken as traveling along the axis (the z-axis) the boundary condition for scattering from channel  $i$  to channel  $j$  can be written

as

$$\psi(r, \theta) \underset{r \rightarrow \infty}{\sim} \delta_{ij} e^{ik_i z} + \frac{f_{ij}(\theta) e^{ik_j r}}{r}, \quad (2.22)$$

where the azimuthal angle  $\varphi$  dependence has been omitted due to the cylindrical symmetry around the collision axis. The function  $f_{ij}(\theta)$  is the *scattering amplitude* which tells us the probability of scattering in a given direction and  $k_i$  is the asymptotic wave number. The *cross section*  $\sigma_{ij}$  for the reaction is obtained by integrating the *differential cross section*,  $d\sigma_{ij} = |f_{ij}(\theta)|^2 d\Omega$ , given by the absolute square of the scattering amplitude, over all solid angles<sup>4</sup>, viz.,

$$\sigma_{ij} = \frac{2\pi k_j}{k_i} \int_0^\pi |f_{ij}(\theta)|^2 \sin\theta d\theta. \quad (2.23)$$

As discussed in Chapter 1, it is the most useful scattering quantity for experimentalists and theoreticians in plasma modeling. It describes the likelihood of two particles interacting under certain conditions.

To determine the scattering amplitudes,  $f_{ij}(\theta)$ , the asymptotic form of the scattered wave function, Equation (2.22), is expanded in terms of Legendre polynomials and radial wave functions. The radial wave functions in the asymptotic limit can be written as a linear combination of an incoming wave and an outgoing wave multiplied by a *Scattering matrix* (S-matrix) element,  $S_{ij}$ , which measures the response of the target. When this expression is inserted into the partial wave expansion<sup>5</sup>, and the final expansion is compared with the asymptotic boundary condition, Equation (2.22), the

---

<sup>4</sup>Solid angle  $d\Omega = \sin\theta d\theta d\varphi$ .

<sup>5</sup>Since we are assuming the potential is spherically symmetric, the angular momentum is conserved. Each partial wave (labeled by a particular  $l = 0, 1, 2, 3, \dots$ ) scatters independently.

following expression for the scattering amplitude  $f_{ij}(\theta)$  is obtained,

$$f_{ij}(\theta) = \frac{i}{2(k_i k_j)^{\frac{1}{2}}} \sum_{l=0}^{\infty} (2l+1) P_l(\cos\theta) (S_{ij,l} - \delta_{ij}), \quad (2.24)$$

where  $l$  is the angular momentum of electron,  $P_l(\cos\theta)$  is the Legendre polynomial and  $\delta_{ij}$  is delta function. The S-matrix element  $S_{ij,l}$  is defined by

$$S_{ij,l} = e^{2i\delta_{ij,l}}. \quad (2.25)$$

The quantity  $\delta_{ij,l}$  here is denoted as the *phase shift*, which measures a phase delay (advance) between incident and scattered waves passing through the target scattering center. It can be used to obtain the resonance which is a nearly bound state forming when the electron is temporarily trapped by the target at certain energy. The resonance gives rise to a sharp variation in the cross section and more information about it can be found in Section 5.2.

Inserting the expression for  $f_{ij}(\theta)$  into that for the cross section, Equation (2.23), and using orthogonality of the Legendre polynomials,

$$\int_0^\pi P_l(\cos\theta) P_{l'}(\cos\theta) \sin\theta d\theta = \left( \frac{2}{2l+1} \right) \delta_{ll'}, \quad (2.26)$$

yields

$$\sigma_{ij} = \sum_{l=0}^{\infty} \sigma_{ij,l}. \quad (2.27)$$

where

$$\sigma_{ij,l} = \frac{\pi}{k_i^2} (2l+1) |S_{ij,l} - \delta_{ij}|^2. \quad (2.28)$$

Consider a totally elastic collision in one of the channels  $i$ . The cross section for this channel,  $\sigma_e = \sigma_{ii,l}$ , becomes

$$\sigma_e = \frac{\pi}{k^2}(2l+1)|S_l - 1|^2, \quad (2.29)$$

where  $S_l = S_{ij,l}$  and the quantity  $1 - S_l = T_l$  is the transition, or T-matrix. In an actual electron-molecule scattering event (for example the calculations in the present thesis, i.e. the  $e^- + \text{NO}_2$  and  $e^- + \text{N}_2\text{O}$  collisions), the interaction potential,  $U(r)$ , is non-spherical and the S (or T) matrix will have both  $l$  and  $\lambda$  indices where  $\lambda$  is the projection of  $l$ . It should also be noted that the eigenphase sums are more widely studied in actual scattering calculation. As a function of energy, the eigenphase sums is given by:

$$\delta(E) = \sum_{l,\lambda} \delta_{l,\lambda}(q_i, E). \quad (2.30)$$

Consequently, the most important task for scattering calculation is to obtain the accurate scattering quantities such as eigenphase sums and S (or T) matrix. There are a variety of theoretical procedures developed for computing these quantities of low-energy electron-molecule scattering, such as the Complex Kohn variational method [47], the Schwinger multi-channel method [48] and the R-matrix method [49]. The former two methods are variational approaches, while R-matrix method employed in the present scattering calculation is a bound state approach [50] and this method will be outlined later in Section 2.2.2.

### 2.2.2 R-matrix theory

Collisions between the low-energy electron and molecules are the major interactions determining the behavior of the plasma. Most of them are difficult and expensive to make the relevant measure-

ments in the laboratory. There is thus an increasing demand of computational procedures for obtaining reliable cross sections and rate constants for key processes. The R-matrix method is one of the most effective tools for calculating those important data. It was initially introduced by Wigner and Eisenbud [51, 52] in the 1940s for nuclear scattering processes. In the early 1970s the method was extended to treat a number of electron-atom [53–55] and electron-diatomic molecule scattering [56–58]. Until the 1990s, the polyatomic codes were developed for general electron-molecule scattering by Nestmann *et al.* [59] and Morgan *et al.* [60, 61]. Comprehensive reviews of the method and of recent work are given by Burke [62] and Tennyson [30]. This section will start with a short overview of the R-matrix methods, described without mathematics. This may be useful to get a feeling for the R-matrix methods, without embarking on all the mathematical details. The overview is followed by a more detailed mathematical description of the method, including some key derivation and references which provide more details to understand how the R-matrix method treats the electron-molecule scattering.

The main idea of R-matrix approach is to divide the configuration space into an inner and an outer regions by a sphere of radius  $a$  (between  $10 a_0$  and  $15 a_0$ ) around the molecular center-of-mass, see Figure 2.4. In the inner region  $r \leq a$  ( $r$  is the radial coordinate of the scattered electron), the scattering electron is considered to be indistinguishable from the electrons of the target, hence the exchange and correlations effects between the target electrons and scattered electrons has to be considered. In the outer region, the scattering electron can be distinguished and the interactions between it and the target can be described by long-range potentials [50]. The R-matrix is then calculated at the boundary between the inner and outer regions, and propagated from  $a$  to about  $100 a_0$ . Finally, the reaction matrix and scattering matrix can be extracted from the R-matrix.

We are now in a position to derive the formal definition of the R-matrix. An electron-target scattering problem is defined as an  $N + 1$  electron problem where  $N$  is the number of target electrons and  $+1$  is the scattering electron. The scattering process can thus be described by the electronic

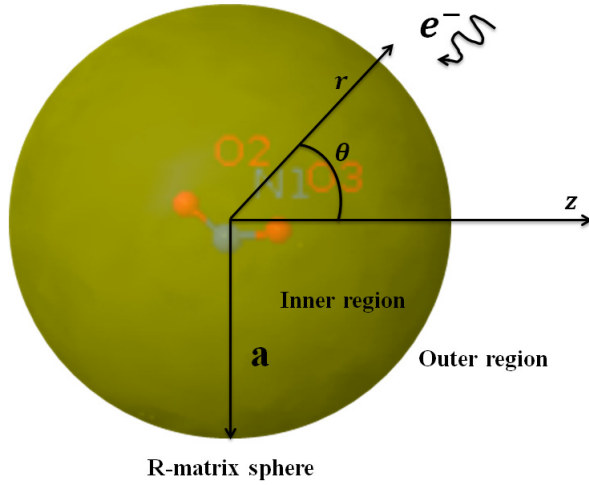


Figure 2.4: A diagram showing the R-matrix sphere surrounding an NO<sub>2</sub> molecule. Space is separated into the ‘inner’ and ‘outer’ regions by a sphere of radius  $a$ .

Schrödinger equation 2.1 with the Hamiltonian  $\hat{H}_{N+1}$

$$(\hat{H}_{N+1} - E) |\psi\rangle = 0. \quad (2.31)$$

In order to solve this equation in a finite volume, i.e. inside the sphere drawn in Figure 2.4, an extra term  $\hat{L}_B$  derived by Bloch [63] has to be included to keep the hermicity of  $\hat{H}_{N+1}$  which is broken by inserting the boundary  $r = a$  in the coordinate space. By adding the Bloch operator to Equation (2.31) and rearranging, a formal solution of the Schrödinger equation for  $r \leq a$  can be found as follows

$$|\psi\rangle = (\hat{H}_{N+1} + \hat{L}_B - E\hat{1})^{-1} \hat{L}_B |\psi\rangle. \quad (2.32)$$

The operator  $\hat{H}_{N+1} + \hat{L}_B$  will be referred to as the inner region Hamiltonian below which only satisfied at discrete values of the energy,  $E$ . Denoting the energy of each solution  $E_k$  and its associated wave function  $\psi_k$  (subscript  $k$  denotes the  $k^{th}$  inner region wavefunction), these satisfy

the equation:

$$\langle \psi_k | \hat{H}_{N+1} + \hat{L}_B | \psi_{k'} \rangle = E_k \delta_{kk'}. \quad (2.33)$$

Therefore, eigenstates  $\psi_k$  of the system form a complete basis set here. Appealing to the closure relation:

$$\sum_k | \psi_k \rangle \langle \psi_k | = \hat{1}, \quad (2.34)$$

Equation (2.32) is rewritten

$$\begin{aligned} | \psi \rangle &= \sum_{k,k'} | \psi_k \rangle \langle \psi_k | (\hat{H}_{N+1} + \hat{L}_B - E \hat{1})^{-1} | \psi_{k'} \rangle \langle \psi_{k'} | \hat{L}_B | \psi \rangle \\ &= \sum_k \frac{| \psi_k \rangle \langle \psi_k | \hat{L}_B | \psi \rangle}{E_k - E}. \end{aligned} \quad (2.35)$$

Now let us use a channel basis function  $| \Phi_j^N Y_{l_j}^{\lambda_j} \Theta_{\frac{1}{2}} \rangle$  (see Equation 2.59 in Ref. [50] for more details), where  $\Phi_j^N$  is the  $N$ -electron target wave function for channel  $j$ ,  $\Theta_{\frac{1}{2}}$  is the electron spin function which describe the spin motion of the scattered electron,  $Y_{l_j}^{\lambda_j}$  is spherical harmonic with azimuthal and magnetic quantum numbers  $l_j, \lambda_j$  associated with channel  $j$  and define the reduced radial function

$$F_j(a) = \langle \Phi_j^N Y_{l_j}^{\lambda_j} \Theta_{\frac{1}{2}} | \psi \rangle, \quad (2.36)$$

the (energy-independent) boundary amplitude of the  $k^{th}$  inner region function for the  $j^{th}$  channel,

$$w_{jk}(a) = \langle \Phi_j^N Y_{l_j}^{\lambda_j} \Theta_{\frac{1}{2}} | \psi_k \rangle, \quad (2.37)$$

substituting the expression of Bloch operator  $\hat{L}_B$  and projecting the inner region total wave function

(2.35) onto the channel basis function  $|\Phi_j^N Y_{l_j}^{\lambda_j}\rangle$ , gives the following expression ,

$$F_i(a) = \frac{1}{2} \sum_k \frac{w_{ik}(a)}{E_k - E} \sum_j w_{jk}(a) \left[ r \frac{dF_j}{dr} - bF_j \right] \Big|_{r=a} . \quad (2.38)$$

The standard form of the R-matrix on the boundary  $R_{ij}(a, E)$  is defined as

$$R_{ij}(a, E) = \frac{1}{2} \sum_k \frac{w_{ik}(a) w_{jk}(a)}{E_k - E} . \quad (2.39)$$

Obviously, the R-matrix makes a link between the reduced radial function and the derivative of the reduced radial function. It provides the boundary condition for the Schrödinger equation appropriate for the outer region. Since the required values to construct R-matrix are the eigenenergies  $E_k$ , and the associated surface amplitudes,  $w_{ik}(a)$ , of the inner region wave functions  $\psi_k$ , the precise structure of the trial wavefunction employed by the UK R-matrix package to represent the inner region wavefunctions will be discussed further below.

In the inner region, the  $N + 1$  electron wavefunction is constructed using the standard close-coupling (CC) expansion [64],

$$\psi_k = \hat{A} \sum_{ij} a_{ijk} \Phi_i^N(\mathbf{X}_1 \cdots \mathbf{X}_N) u_{ij}(\mathbf{X}_{N+1}) + \sum_i b_{ik} \chi_i^{N+1}(\mathbf{X}_1 \cdots \mathbf{X}_N) . \quad (2.40)$$

The functions are labeled as  $N$  or  $N + 1$  according to whether they refer to the target or the compound scattering system respectively.  $\Phi_i^N$  is the wavefunction of the  $i^{\text{th}}$  target state, and  $u_{ij}$  denotes the extra continuum orbitals used to represent the  $j^{\text{th}}$  scattering electron. The continuum orbitals are constructed from continuum basis functions [64, 65] with a partial wave expansion (similarly to Equation (2.24)) up to some maximum value of  $l$ . For the partial wave of the scattering electron,  $l_{\text{max}} = 4$  ( $s, p, d, f, g$ ) is defaulted in the R-matrix calculation. Considering  $\lambda$  could be the value from  $-l$  to  $l$ , we will have  $\sum_0^4 (2l + 1) = (l_{\text{max}} + 1)^2$ , i.e. 25 partial waves in this thesis. These par-

tial waves belong to different symmetries in Table 2.2, and target virtual orbitals. It should also be noted that, the electrons represented by the space-spin coordinates,  $\mathbf{X}_i$ , must obey the Pauli principle which is met by the use of the antisymmetrization operator  $\hat{A}$ . The first summation runs over the electronic target states. It describes a situation in which the scattering electron is restricted to only the continuum orbitals and the target electrons restricted to only target orbitals, the configurations that arise are known as ‘target + continuum’ configurations. The second summation in the above expression represents short-range polarization effects. It runs over configurations  $\chi_i^{N+1}$ , where all electrons are placed in orbitals associated with the target. These square-integrable functions  $\chi_i^{N+1}$  are zero on the R-matrix boundary and are hence known as ‘ $L^2$ ’ -functions <sup>6</sup> [66]. The variational coefficients  $a_{ijk}$  and  $b_{ik}$  can be obtained by diagonalizing the  $N + 1$  electron Hamiltonian.

On the R-matrix boundary, Equation (2.40) can be simplified as

$$\psi_k|_a = \sum_{ij} a_{ijk} \Phi_i^N u_{ij}(a). \quad (2.41)$$

Because the scattering electron is now distinct from the target electrons there is no requirement for an antisymmetrisation operator. Additionally, the ‘ $L^2$ ’ -functions in the Equation (2.40) vanish as there are no longer exchange or correlation effects with the target electrons. Substituting Equation (2.41) into definition (2.37), gives the following expression:

$$w_{ik}(a) = \sum_j u_{ij}(a) a_{ijk}. \quad (2.42)$$

We can find that in practice the continuum orbitals are also used to compute the surface amplitudes rather than the integral given in Equation (2.37).

---

<sup>6</sup> $L^2$  configuration means all the electrons are in non-continuum, short range orbitals.

In outer region, the wave function can be written as:

$$\psi = \sum_{i=1}^n \Phi_i^N(\mathbf{X}_1 \cdots \mathbf{X}_N) F_i(r_{N+1}) Y_{l_i}^{\lambda_i}(\theta, \phi) \Theta_{\frac{1}{2}} \quad (2.43)$$

where the summation runs over the all  $n$  channels and terms in the above equation have already been defined above. Substituting this wavefunction into the Schrödinger Equation (2.31) and projecting onto the channel basis functions result in a set of coupled differential equations for the reduced radial functions,

$$\left[ -\frac{d^2}{dr^2} + \frac{l_i(l_i+1)}{r^2} - k_i^2 \right] F_i(r) = 2 \sum_{j=1}^n U_{ij}(r) F_j(r). \quad (2.44)$$

To solve the outer region problem, outer region potentials and information about asymptotic channels of the problem are needed. The long range potentials in the outer region,  $U_{ij}(r)$ , is defined by

$$U_{ij}(r) = \sum_{\beta=0}^{\infty} \frac{\alpha_{ij}^{\beta}}{r^{\beta+1}}. \quad (2.45)$$

The coefficients  $\alpha_{ij}$  of expansion dictate the coupling between the channels  $i$  and  $j$  defined in terms of the Clebsch-Gordan coefficients and target moment. In general, only the first few terms in the expansion over  $\beta$  play a significant role in the outer region collision. For neutral targets such as  $\text{NO}_2$  and  $\text{N}_2\text{O}$ ,  $\beta$  is 1.

Asymptotic channel  $i$  describes a state of the target molecule and a partial wave (see Section 2.2.1) of the scattering electron,  $(l_i, m_i)$ . If the target state associated with channel  $i$  has energy  $E_i^N$ , then the wave number of the scattering electron associated with this channel is given by

$$k_i^2 = 2(E - E_i^N). \quad (2.46)$$

By convention, the lowest target state is taken to be zero. Channels are described as being open, or closed depending on whether  $k_i^2$  is positive or negative (respectively). Normalization to energy, the outer region solutions asymptotically approach the following results:

$$\lim_{r \rightarrow \infty} F_{ij}(r) \sim \begin{cases} \frac{1}{\sqrt{k_i}}(\sin\theta_i\delta_{ij} + \cos\theta_i K_{ij}) & \text{if } E_i \geq 0 \\ 0 & \text{otherwise} \end{cases} \quad (2.47)$$

where channel angle  $\theta_i$ , for neutral target, has the form

$$\theta_i = k_i r - \frac{1}{2} l_i \pi. \quad (2.48)$$

With the asymptotic expansion techniques [67, 68] and propagating the R-matrix (2.39) from  $a$  to  $100 a_0$  (beyond  $100 a_0$  the non-coulombic potential can be ignored) [69, 70], the critical parameter in Equation (2.47), the K-matrix elements  $K_{ij}$ , can be obtained. K-matrix is a symmetric matrix whose dimension is the number of open channels. Many of the other scattering matrices and observables are defined in terms of the K-matrix. For example, it provides another way to express the phase shift of Equation (2.30)

$$\delta(E) = \sum_i \arctan(K_{ii}^D). \quad (2.49)$$

$\delta(E)$  is the *eigenphase sums* over all partial waves,  $K_{ii}^D$ <sup>7</sup> are the eigenvalues of the K-matrix. Eigenphase is a quantity analogous to the phase shift mentioned in Section 2.2.1. It is very useful for studying the convergence of the calculations and comparing different models. Examples of this quantity can be seen in Figure 3.12. By fitting the eigenphase to a Breit-Wigner form (Equation (5.3)) we can obtain the resonance position and width. The information of resonance is the key to many potential problems such as the Dissociative Electron Attachment (DEA) process which will

---

<sup>7</sup>D stands for diagonal.

be discussed in Chapter 5.

The S-matrix (the S-matrix element is  $S_{l'\lambda,l\lambda}$ ) mentioned in Equation (2.25) is also related to the K-matrix by the equation

$$\hat{S} = \frac{\hat{1} + i\hat{K}}{\hat{1} - i\hat{K}}, \quad (2.50)$$

$\hat{S}$  can be diagonalized by the real orthogonal transformation which also diagonalizes K-matrix. Hence we can write

$$\mathbf{A}^T \mathbf{S} \mathbf{A} = \exp(2i\mathbf{\Delta}) = \mathbf{\Lambda}. \quad (2.51)$$

where the diagonal elements of  $\mathbf{\Lambda}$  have the same form with Equation (5.3) in potential scattering Section 2.2.1 and can be expressed in terms of the eigenphases, as follows:

$$\Lambda_{ii} = \exp(2i\delta_i), \quad i = 1, \dots, n_a \quad (2.52)$$

where  $\delta_i$  is a real eigenphase, and  $n_a$  is the number of open channels of the energy  $E$ . The cross sections can then be derived from the scattering matrix.

In the practice, running an R-matrix calculation is complicated, especially for a fresh PhD student. Users have to make a large number of choices covering issues such as the implementation of symmetry rules, target basis set, continuum basis set, the R-matrix interaction radius, models for the inner region scattering problem, reference configurations for CI expansions, resonance fitting etc. Therefore, an expert system Quantemol-N with a friendly and intuitive graphical user interface was developed to address this problem. The Quantemol-N software can not only make *ab initio* scattering calculations accessible to the non-specialists, but also make it much easier and quicker for specialists to perform such calculations. UKRmol suite with Quantemol-N interface is used in

this thesis to obtain relevant scattering quantities in the FN approximation. A tutorial system was created in Quantemol-N to show how to set up calculation and yield results quickly. More details can be found by clicking on the ‘?’ button on the displaying panel in software and Ref. [71]. A briefly guidance of the main procedure associated with the cases of this thesis and some points have not been emphasized in other literatures can be found in Appendix A.

### 2.2.3 Vibrational frame transformation

The S-matrix constructed in R-matrix theory represents the electron-molecule scattering only if the nuclei are seen to be stationary from the perspective of the scattering electron (referred as fixed-nuclei (FN) S-matrix in the following). However, as the distance between the scattering electron and the target increases, the *speed* of the scattering electron will be decelerated due to the attenuation of the target attraction. The FN approximation may no longer be valid when the collision energy is comparable to the vibrational energy of the molecule. Therefore, the vibrational motion has to be taken into account to advance the FN approximation in low-energy collision.

One way to involve the possibility of nuclear motion during the full collision process is by applying the theory of vibrational frame transformation [72–74],

$$S_{v_i l' \lambda', v_i l \lambda} = \left\langle \eta_{v_i}(q_i) | S_{l' \lambda', l \lambda}(q_i) | \eta_{v_i}(q_i) \right\rangle, \quad (2.53)$$

where different normal modes are assumed to be uncoupled. In the above expression,  $q_i$  is normal coordinate for mode  $i$ ; index  $v_i$  denote the vibrational quantum number for each normal mode  $\{v_1, v_2, \dots\}$ ;  $\eta_{v_i}$  is the vibrational wave functions of different normal modes as mentioned in Equation (2.19).  $S_{l' \lambda', l \lambda}$  is an element of the fixed-nuclei scattering matrix obtained from R-matrix with initial channel  $l \lambda$  and exit channel  $l' \lambda'$ ,  $l$  being the electron angular momentum and  $\lambda$  its projection

on the molecular axis. This formalism allows us to use the fixed-nuclei matrix to construct a physically meaningful matrix describing the amplitude of scattering from a particular vibrational state  $v_i$  of the target to another one  $v'_i$ . The two matrices are considered as two equivalent forms of the same scattering operator in two different representation bases (or say the frame transformation as a change of basis from the molecular reference frame to the laboratory reference frame). Furthermore,  $S_{l'\lambda',l\lambda}$  has the same energy channel while we are below the ionization threshold. Equation (2.53) implies two origins for the energy one with respect to the state  $v_i$  and the other to  $v'_i$ . Thus there is an uncertainty on the origin of the energy we should take :  $\varepsilon_{v_i}$  or  $\varepsilon_{v'_i}$ , where  $\varepsilon_{v_i} = E - E_{v_i}$ ; The problem could be fixed if  $S(q_i, \varepsilon_{v_i}) \approx S(q_i, \varepsilon_{v'_i})$ . In other words, one requires the  $S_{l'\lambda',l\lambda}$  to be independent on the scattering energy within the spacing of vibrational levels. For convenience, using S-matrix from vibrational frame transformation (2.53) we introduce the quantities

$$P_{v'_i v_i} = \sum_{l'\lambda',l\lambda} \left| S_{v'_i l'\lambda', v_i l\lambda} - \delta_{v'_i l'\lambda', v_i l\lambda} \right|^2, \quad (2.54)$$

which could interpreted as the probability of excitation of the vibrational mode  $i$ . Using  $P_{v'_i v_i}$ , similarly to Equation (2.28), the vibrational excitation cross section can then be written as [75]

$$\sigma_{v'_i v_i} = \frac{\pi}{k^2} P_{v'_i v_i} = \frac{\pi \hbar^2}{2m\varepsilon} \sum_{l'\lambda',l\lambda} \left| S_{v'_i l'\lambda', v_i l\lambda} - \delta_{v'_i l'\lambda', v_i l\lambda} \right|^2, \quad (2.55)$$

where  $k_{v'_i} \approx k_{v_i} = k$  is the wave vector of the scattering electron ( $\varepsilon$  is electron scattering energy) and  $m$  is the reduced mass of the electron–target system. This cross section should be viewed as averaged over initial rotational states and summed over final rotational states of corresponding vibrational levels<sup>8</sup>.

Very often, at low energy scattering, one can use the Taylor expansion to expand the fixed-nuclei

---

<sup>8</sup>Neglecting the rotational structure would correspond to an experiment for which the energy resolution is worse than a typical energy splitting between rotational levels.

S-matrix obtained from R-matrix theory,  $S_{l'\lambda',l\lambda}(\mathbf{q})$  at the first order along normal coordinates as,

$$S_{l'\lambda',l\lambda}(\mathbf{q}) = S_{l'\lambda',l\lambda}(\mathbf{q}_{eq}) + \sum_i \frac{\partial S_{l'\lambda',l\lambda}(q_i)}{\partial q_i} q_i. \quad (2.56)$$

where  $\mathbf{q}_{eq}$  is the equilibrium configuration of the target and keep in mind the following identity

$$q_i = \frac{1}{\sqrt{2}}(\hat{a} + \hat{a}^\dagger), \quad (2.57)$$

$$\langle \eta_{v'_i}(q_i) | \eta_{v_i}(q_i) \rangle = \delta_{v'_i v_i}, \quad (2.58)$$

where  $\hat{a}$  is the creation operator, and  $\hat{a}^\dagger$  is the annihilation operator. It follows

$$\begin{aligned} S_{v'_i l' \lambda', v_i l \lambda} &\approx S_{l' \lambda', l \lambda}(\mathbf{q}_{eq}) \delta_{v'_i v_i} + \frac{\partial S_{l' \lambda', l \lambda}(q_i)}{\partial q_i} \left\langle \eta_{v'_i}(q_i) \left| \frac{1}{\sqrt{2}}(\hat{a} + \hat{a}^\dagger) \right| \eta_{v_i}(q_i) \right\rangle. \\ &= S_{l' \lambda', l \lambda}(\mathbf{q}_{eq}) \delta_{v'_i v_i} + \frac{1}{\sqrt{2}} \frac{\partial S_{l' \lambda', l \lambda}(q_i)}{\partial q_i} (\sqrt{v_i} \delta_{v'_i, v_i-1} + \sqrt{v_i+1} \delta_{v'_i, v_i+1}). \end{aligned} \quad (2.59)$$

by substituting Equations (2.56, 2.57, 2.58) into Equation (2.53).

As the probability defined in Equation (2.54), the excitation probabilities for the corresponding vibrational transitions can now be written as

$$P_i = \frac{g_i}{2} \sum_{l' \lambda', l \lambda} \left| \frac{\partial S_{l' \lambda', l \lambda}(q_i)}{\partial q_i} \right|^2, \quad (2.60)$$

where  $g_i$  is the degeneracy of the mode  $i$ , the cross-section for inelastic vibrational excitation of one quanta  $v'_i = 1 \leftarrow v_i = 0$  for mode  $i$  writes

$$\sigma_{10}^i = \frac{\pi \hbar^2}{2m\varepsilon} \theta(\varepsilon - \hbar\omega_i) P_i. \quad (2.61)$$

$\theta$  is the Heaviside step function which opens the vibrational excitation channel when  $\varepsilon \geq \hbar\omega_i$ . The cross section for vibrational de-excitation of one quanta for the  $i^{\text{th}}$  normal modes is given by removing the Heaviside step function  $\theta$  from Equation (2.61). Equation (2.61) is an approximation of Equation (2.55) at the first order of  $q_i$ . It is clear that this expression significantly reduce the computational effort because only two values of  $q_i$  are need to calculate the derivative of the fixed-nuclei S-matrix used in cross section calculation. This simple formulation above can describe the (de-)excitation process changing only one quantum in each normal mode of the target molecule (for more details, see Appendix C). Excitation cross-sections for changing two or more quanta in a mode is neglected in Equation (2.61) due to the propensity rule.

According to the simple analytical form of the cross sections, the corresponding rate coefficients are easily evaluated from the general expression

$$\alpha_{v_i'v_i}(T) = \frac{8\pi}{(2\pi k_b T)^{\frac{3}{2}}} \int_0^{\infty} \sigma_{v_i'v_i}(\varepsilon) e^{-\frac{\varepsilon}{k_b T}} \varepsilon d\varepsilon, \quad (2.62)$$

giving

$$\alpha_{10}^i(T) = \sqrt{\frac{2\pi}{k_b T}} \frac{\hbar^2}{m^{3/2}} P_i \exp\left(-\frac{\hbar\omega_i}{k_b T}\right), \quad (2.63)$$

where  $k_b$  is the Boltzmann coefficient and  $T$  is the temperature.

To summarize, the theory of frame transformation extends the FN approximation by including the vibrational motion of the target adiabatically. This theory is valid as long as the fixed-nuclei scattering matrix is smooth with respect to the scattering energy. Generally, this theory is robust for ionic targets due to the smooth behavior of S-matrix (for ionic targets, the Coulomb force in the electron-ion collision accelerates the incident electron, which leads to an energy-independent eigenphase). For neutral target, its usefulness comes most often from the quality of the obtained re-

sults. We can directly apply this method when the S-matrix of electron-neutral collision is smooth. If the S-matrix is energy-dependent, we can remove the energy dependence by choosing a different normalization factor for the scattering wave function [76–78]. Then, the re-normalized  $\tilde{S}(q_i)$  is energy-independent and can be used for frame transformations in Equation (2.53). After the transformations, the re-normalization factor is multiplied back, and the energy dependence is recovered.

## CHAPTER 3: CROSS SECTIONS AND RATE COEFFICIENTS FOR VIBRATIONAL (DE-) EXCITATION OF NO<sub>2</sub> BY ELECTRON IMPACT

In this chapter, we use the theoretical tools introduced in Chapter 2 to compute cross sections for vibrational excitation of NO<sub>2</sub> ( $X^2A_1$ ) by electron impact. Calculations are based on a combination of the normal mode approximation for vibrational states of the target molecule (Section 2.1.3), fixed-nuclei electron-NO<sub>2</sub> scattering matrices (Section 2.2.2) and the vibrational frame transformation (Section 2.2.3) employed to evaluate the scattering matrix for vibrational transitions. Thermally-averaged rate coefficients are derived from the obtained cross sections for temperatures in the 10-10000 K interval for excitation of each normal mode of the target molecule. Analytical fits for the rate coefficients for singlets and triplets are provided to simplify their utilization in plasma depollution models as mentioned in Chapter 1. In addition, a comprehensive set of calculations are performed for assessing the uncertainty of the present calculations because of lack of experimental data. The uncertainty assessments indicate that the computed observables for vibrational (de-)excitation is reasonable for later use in NO<sub>2</sub>-containing plasma kinetics modeling. The following work has been published in *Plasma Sources Science and Technology* [79].

### 3.1 Introduction

The nitrogen dioxide (NO<sub>2</sub>) molecule has a number of applications in engineering and science. For instance, it is used in the sterilization of medical instruments [80]. In atmospheric science, the chemiluminescent emission from electronically excited NO<sub>2</sub> in the O + NO reaction, known as “air afterglow” [81], is important for understanding the complex physical processes in the middle and upper atmosphere. However, nitrogen dioxide is an undesirable pollutant in the troposphere. Exposure to the environment where the concentration of NO<sub>2</sub> exceeds 3ppm for longer than 8

hours (or  $> 5$  ppm for longer than 15 minutes) yields the negative effect on the human respiratory system [82]. The role of this trace constituent of atmosphere constantly increases along with an increase in its emission rate caused mainly by human activities such as automobile exhaust and industrial combustion. Non-equilibrium plasma technology has been introduced over the past several years as a promising technique for  $\text{NO}_2$  removal. The development of the technology requires knowledge of physical and chemical processes taking place in  $\text{NO}_2$  plasma. Especially important processes are collisions between electrons and  $\text{NO}_2$  molecules because the availability of accurate data for these processes is crucial for plasma modeling.

Electron collisions with the  $\text{NO}_2$  molecule have been extensively investigated in the past, with first studies focused on the  $\text{NO}_2$  ionization [83–85] due to a variety of applications in plasma technology. In more recent studies, other processes in the  $e^-$ - $\text{NO}_2$  collisions were studied. For example, Szymtkowski *et al.* [86] measured absolute total cross sections for electron- $\text{NO}_2$  collisions in a linear transmission experiment for the interval 0.6 to 220 eV of collision energies. A further investigation from intermediate to high energies was carried out by Zecca *et al.* [87]. Experiments by Fox [88] and Rangwala *et al.* [89] reported dissociative electron attachment (DEA) to  $\text{NO}_2$  as a mechanism on negative-ion formation. Munjal *et al.* [90] reported theoretical data on elastic integral, differential, momentum transfer cross sections, as well as electronic-excitation cross sections from the ground electronic state to the five lowest electronically excited states of  $\text{NO}_2$ .

Despite these efforts, still little information is available on the electron-impact vibrational excitation (VE) of  $\text{NO}_2$ . This process plays an important role in the chemistry and the physics of molecular plasma because vibrationally excited  $\text{NO}_2$  reacts differently, compared to the ground-state  $\text{NO}_2$ , with other species present in the plasma [91]. To the best of our knowledge, there exist only one measurement on VE cross sections for energies  $0.3 \sim 2.5$  eV by Benoit and Abouaf [92]. No theoretical study on VE of  $\text{NO}_2$  has been reported until now. As excitation of different modes have almost the same fundamental frequencies cannot be separated experimentally at least by the

conventional techniques, so the theoretical treatment for the VE of NO<sub>2</sub> is indeed necessary. To fill this gap, the objective of the present study is to provide VE cross sections and corresponding thermally-averaged rate coefficients obtained theoretically. Systematic calculations were performed for the excitation of the 3 lowest excited vibrational levels in the ground electronic state of NO<sub>2</sub>. For higher vibrational states, processes such as DEA become more predominant than vibrational excitation which will be discussed later in Chapter 5.

The chapter is organized as follows. In the next section, the theoretical approach used in the present calculation is briefly described according to Chapter 2. In Section 3.3, the obtained VE cross sections and corresponding rate coefficients are shown and discussed. Section 3.4 presents uncertainty estimations of the present approach. The concluding remarks are given in Section 3.5.

### 3.2 The Properties Of The NO<sub>2</sub> Molecule And Scattering Calculations

As mentioned in Section 2.1.2, NO<sub>2</sub> is an open-shell molecule belonging to the C<sub>2v</sub> point group at its equilibrium, with the ground state electronic configuration

$$X^2A_1 : 1a_1^2 2a_1^2 1b_2^2 3a_1^2 2b_2^2 4a_1^2 5a_1^2 3b_2^2 1b_1^2 4b_2^2 1a_2^2 6a_1^1.$$

It is characterized by three normal modes of vibration: bending ( $\nu_1$ ), symmetric stretching ( $\nu_2$ ), and asymmetric stretching ( $\nu_3$ ) (see Figure 3.1). Displacements along the bending and symmetric stretching modes do not break the C<sub>2v</sub> symmetry of the molecule, while the asymmetric stretching mode reduces the symmetry to the C<sub>s</sub> group according to the correlation Table 2.2.

Electronic structure and frequencies of normal modes can be determined using the *ab initio* quantum chemistry package MOLPRO as introduced in Section 2.1.4. As it is becoming increasingly recognized that uncertainty estimation is a necessary procedure for molecular structure calcula-

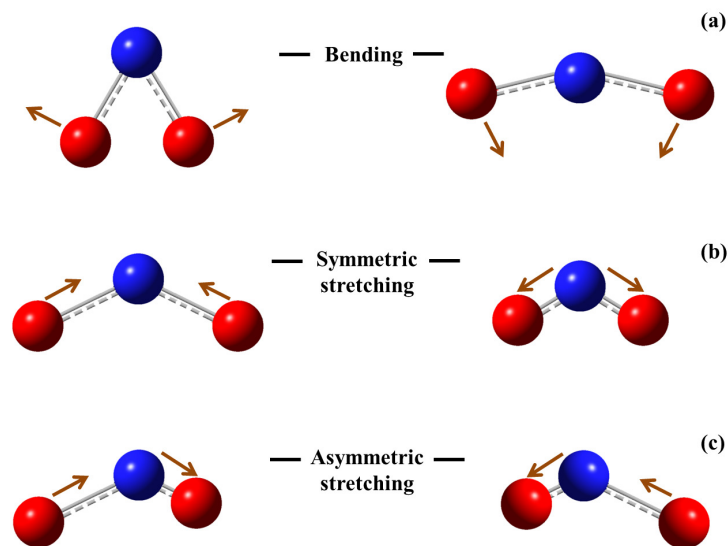


Figure 3.1: The sketch of three normal modes of  $\text{NO}_2$ : bending ( $\nu_1$ ), symmetric stretching ( $\nu_2$ ), and asymmetric stretching ( $\nu_3$ ). The red balls represent the O atoms and the blue balls represent the N atoms. The arrows indicate the force vectors.

tion [93], we performed calculations by the complete active space self-consistent field (CASSCF) (see Section 2.1.1) method with different CAS and basis sets shown in Table 2.1 to assess the present property calculation. Firstly, we use the same CAS which freezes 3 core orbitals and allowing the remaining 17 electrons freely distributed in 12 active orbitals ( $3-7a_1$ ,  $1-2b_1$ ,  $2-5b_2$  and  $1a_2$ ) and increase the size of basis set. We can find that the equilibrium geometry and normal mode frequency obtained by cc-pVTZ basis set agree with experimental data well. Thus we keep cc-pVTZ basis set and increase the size of CAS. Clearly, CASSCF (17,12) with cc-pVTZ can provide us a good agreement between our results and experiment.

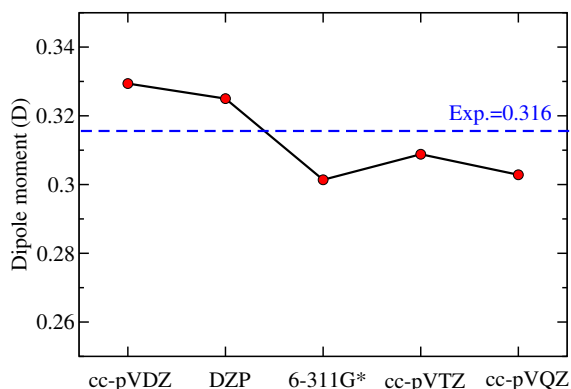
It is more intuitive to investigate the stability of other target properties such as the permanent dipole moment introduced in Equation (2.21) and ground state energy of  $\text{NO}_2$ . The results is shown in Figure 3.2. As we can see, when we set the "CAS" used in calculation as CAS5 (CASSCF(17,12) is set as CAS5 here) and increase the size of basis set, the dipole moment gradually approaches

Table 3.1: Structure and vibrational frequencies of NO<sub>2</sub> obtained in this study and compared with experimental data.  $\omega_1$ ,  $\omega_2$  and  $\omega_3$  are the frequencies of bending mode, symmetric stretching mode and asymmetric stretching mode, respectively. The numbers such as (17, 12) in the parentheses indicate 17 electron are kept free in 12 active orbitals.

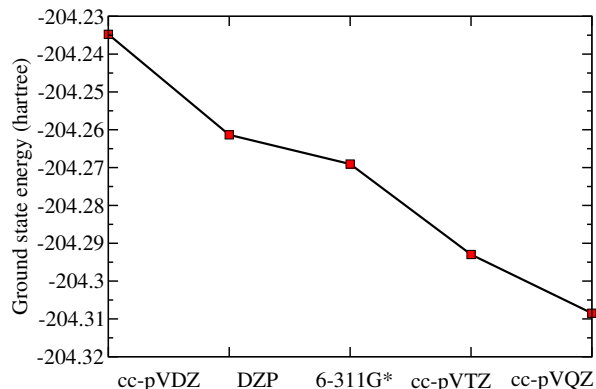
Method	Basis set	Bond (Å)	Angle(Degrees)	$\omega_1$ (cm <sup>-1</sup> )	$\omega_2$ (cm <sup>-1</sup> )	$\omega_3$ (cm <sup>-1</sup> )
CASSCF(17,12)	cc-pVDZ	1.208	133.8	750	1327	1640
CASSCF(17,12)	DZP	1.219	133.2	753	1316	1620
CASSCF(17,12)	6-311G*	1.206	133.7	756	1325	1634
CASSCF(17,12)	cc-pVTZ	1.204	133.9	756	1319	1625
CASSCF(17,12)	cc-pVQZ	1.203	133.9	759	1322	1623
CASSCF(9,8)	cc-pVTZ	1.186	136.3	764	996	1407
CASSCF(11,9)	cc-pVTZ	1.197	134.2	762	1315	1653
CASSCF(13,10)	cc-pVTZ	1.203	133.8	761	1325	1637
CASSCF(15,11)	cc-pVTZ	1.203	133.9	758	1322	1632
CASSCF(17,12)	cc-pVTZ	1.204	133.9	756	1319	1625
Exp.		1.193	134.1	750	1318	1618

the experimental value and the ground state energy decreases monotonically. The results with cc-pVTZ basis set is more closer to the experiment. Similarly, we keep the basis set as cc-pVTZ and increase the CAS, both of the dipole moment and ground state energy did not change significantly above CAS3, which means the property calculation with cc-pVTZ basis set and the CAS which is larger than CAS3 can provide us convergent results. Therefore, in the present electronic structure calculations, we use CASSCF method built from Hartree Fock (HF) orbitals with the CAS (17,12) and cc-pVTZ basis set since the properties calculated by this model match excellently with the experiment and are convergent result, namely accurate description of target molecule is obtained. Corresponding outputs, especially Hessian equilibrium geometry and frequencies will be used in the scattering part below.

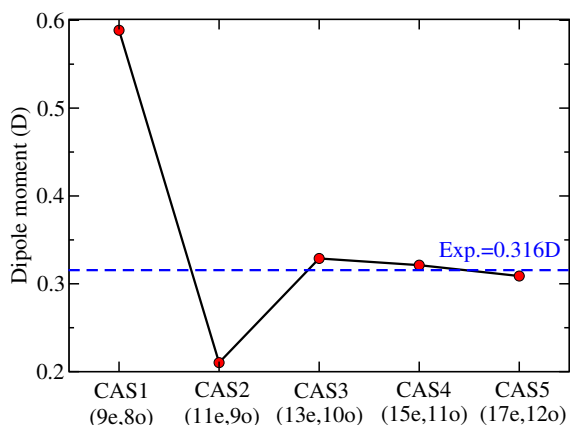
The electron-scattering calculations were carried out using the UK R-matrix code [30] with the Quantemol-N interface [71]. The first step is characterizing the potential energy curve of NO<sub>2</sub> along the normal coordinates. The cc-pVTZ basis set and the complete active space configura-



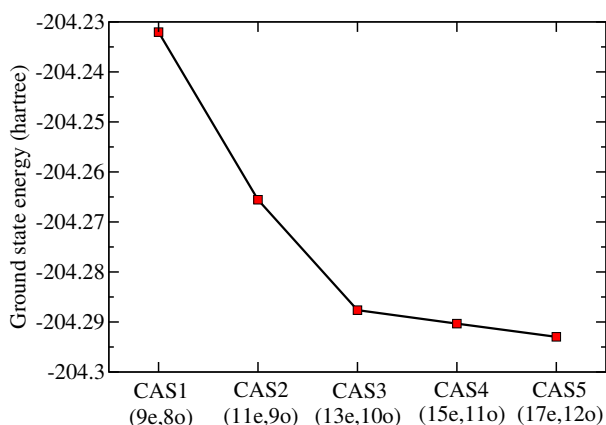
(a) The permanent dipole moment of NO<sub>2</sub> obtained by MOLPRO with different basis sets in CAS5



(b) The ground state energy of NO<sub>2</sub> obtained by MOLPRO with different basis sets in CAS5



(c) The permanent dipole moment of NO<sub>2</sub> obtained by MOLPRO with cc-pVTZ basis set and different CAS



(d) The ground state energy of NO<sub>2</sub> obtained by MOLPRO with cc-pVTZ basis set and different CAS

Figure 3.2: The uncertainty estimation of NO<sub>2</sub> property calculations using MOLPRO. For example, the numbers in brackets (17e, 12o) indicates the CAS that 17 electrons are kept free in 12 active orbitals

tion interaction (CAS-CI) method built on orbitals obtained from the same CASSCF calculation in MOLPRO were used in Quantemol-N calculation<sup>1</sup>. To make the dynamical R-matrix calculation tractable<sup>2</sup>, we freeze 10 electrons in the core  $1a_1, 2a_1, 3a_1, 1b_2, 2b_2$ , while the remaining 13 elec-

<sup>1</sup>we have to check that center of mass does not change and the equilibrium should be the same with Quantemol-N and MOLPRO.

<sup>2</sup>The CAS used in electronic structure calculation is too expensive to run in R-matrix calculation.

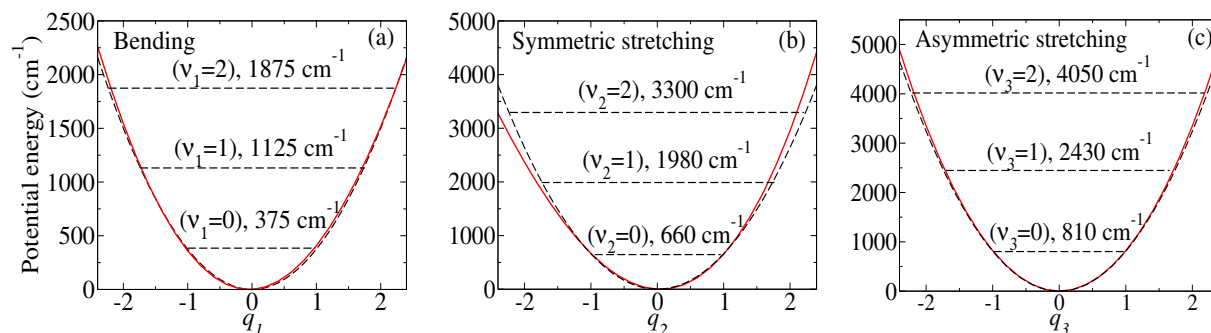


Figure 3.3: Potential energy curves for the ground electronic state of  $\text{NO}_2$  as a function of the (a) bending; (b) symmetric stretching; (c) asymmetric stretching modes. The abscissa axes in the figure represent dimensionless normal coordinates. In each panel, only one mode is varied, while the other modes are kept fixed at their equilibrium positions. Red solid curves are the actual potential energies obtained from the UKRmol suite, while black dashed curves represent energies calculated in the harmonic approximation. Horizontal dashed lines denote energies of vibrational states.

trons are kept free in the active space of the  $4a_1, 5a_1, 3b_2, 1b_1, 4b_2, 1a_2, 6a_1, 7a_1, 2b_1, 5b_2$  molecular orbitals. We used an R-matrix sphere of radius 14 Bohr, large enough to envelop the entire charge clouds of all the target electronic states included in the calculation. A partial waves expansion is used with continuum Gaussian-type orbitals up to  $l \leq 4$ . All the target states below cutoff energy 10 eV are retained in the final close-coupling calculation (Equation (2.40) of Chapter 2).

We plot the potential energy of the ground state of  $\text{NO}_2$  computed with the R-matrix code <sup>3</sup> in Figure 3.3. As discussed in Section 2.1.3, the potential energy surface of  $\text{NO}_2$  is split into the three potential energy curves along normal modes according Equation (2.16) and (2.17). Compared with the harmonic potential potential calculated by  $\frac{\hbar\omega_i}{2}q_i^2$ , we found that an accurate description of the target molecule for bending mode (panel (a) in the figure) and asymmetric stretching mode (panel (c)). Almost no anharmonic contribution is observed for these two modes. However, the potential

<sup>3</sup>Quantemol-N can also perform electronic structure calculation but can not give us normal frequency. Thus we calculated the normal modes using MOLPRO and performed scattering calculations along these normal coordinates.

Table 3.2: Vertical excitation energies (in eV) of NO<sub>2</sub> using CI model at equilibrium geometry

Symmetry No.	State	Present work (eV)
1	X <sup>2</sup> A <sub>1</sub>	0.00
2	<sup>2</sup> B <sub>2</sub>	3.78
3	<sup>2</sup> A <sub>2</sub>	3.82
4	<sup>2</sup> B <sub>1</sub>	4.28
5	<sup>4</sup> B <sub>2</sub>	5.93
6	<sup>4</sup> A <sub>2</sub>	5.95
7	<sup>2</sup> A <sub>2</sub>	6.97
8	<sup>2</sup> B <sub>2</sub>	7.17
9	<sup>2</sup> B <sub>1</sub>	8.23
10	<sup>2</sup> A <sub>2</sub>	8.54
11	<sup>2</sup> A <sub>1</sub>	8.65
12	<sup>4</sup> A <sub>1</sub>	9.83
13	<sup>2</sup> A <sub>1</sub>	10.61
14	<sup>2</sup> B <sub>2</sub>	10.62
15	<sup>4</sup> B <sub>1</sub>	10.90

energy of the symmetric stretching mode is slightly anharmonic as evident from panel (b) in the figure. The dipole moment of NO<sub>2</sub> obtained by Quantemol-N in this model is 0.317 D, which is also in remarkably good agreement with the experimental value of 0.316 D [94].

The vertical excitations energies of the doublet and quartet states calculated using our CI model are presented in Table 3.2. The energy of the first excited state <sup>2</sup>B<sub>2</sub> in our CI model is 3.78 eV<sup>4</sup> which is in good agreement with the CASSCF value 3.425 eV of other theoretical study [95] and 3.07 eV obtained by other R-matrix calculation with CAS-CI model [90]. Clearly, all the quantities presently obtained through Quantemol-N indicate a good description of target molecule .

In the R-matrix scattering calculations, we obtain the reactance matrix (K-matrix) for the e<sup>-</sup>-NO<sub>2</sub> collisions for all four irreducible representations (irrep) A<sub>1</sub>, B<sub>1</sub>, B<sub>2</sub> and A<sub>2</sub>. The fixed-nuclei

---

<sup>4</sup>In fact, our VE calculation will focus on the energy range below first excited state, i.e. the vibrational transitions within the ground electronic state of NO<sub>2</sub> is the main theme in the present calculation.

reactance matrices are then used to compute scattering matrices numerically according to Equation (2.50). The fixed-nuclei S-matrix elements  $S_{l'\lambda',l\lambda}$  with 25 partial waves are used to compute the scattering matrix  $S_{v_i'v_i}$  for VE,



relying on the vibrational frame transformation stated by Equation (2.53). The Gaussian-Legendre quadrature (see Appendix B) with 10 points is used to numerically compute the integral in Equation (2.53).

As explained in Section 2.2.3, the vibrational frame transformation (2.53) treatment becomes feasible, at least in principle, only if the elements of the fixed-nuclei S-matrix for the  $e^- - \text{NO}_2$  system are smooth with respect to the incident energy. Therefore, the treatment is not appropriate if there are low-energy resonances in the  $e^- - \text{NO}_2$  spectrum at low energies. In an attempt to analyse the behavior of S-matrix elements, we computed the absolute value squared  $|S_{l'\lambda',l\lambda}|^2$  of the matrix elements obtained from Quantemol-N calculations as a function of the electron scattering energy at the equilibrium geometry. Figure 3.4 gives an idea about couplings between different partial waves in the scattering process. Here, singlet states are chosen as an example. Clearly, only couplings between channels with  $\Delta l < 2$  are not negligible for inelastic scattering. The contribution from the  $\Delta l \geq 2$  couplings is very small. Notably, the  $|S_{l'\lambda',l\lambda}|^2$  coupling producing the dominant contribution to the inelastic process for each symmetry depends only weakly on the scattering energy, as shown in Figure 3.5. Therefore, it is reasonable to employ the vibrational frame transformation (2.53) to compute  $S_{v_i'v_i}$  for the VE calculations.

With  $S_{v_i'v_i}$  in hand, and taking an average over initial rotational states and a sum over final rotational states in the process, i.e. neglecting the rotational structure of the molecule, the cross sections of Equation (3.1) is then computed by Equation (2.55).

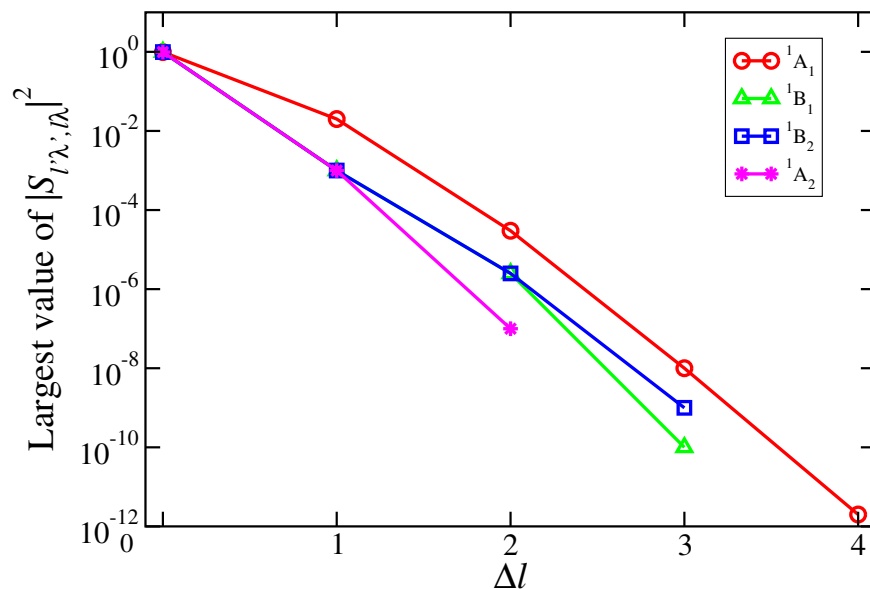


Figure 3.4: The largest value of  $|S_{l'\lambda', l\lambda}|^2$  with respect to all possible allowed combinations of  $l\lambda, l'\lambda'$  as a function of the difference  $\Delta l = l' - l$  for all four singlet irreducible representations (irreps) of the  $e^-$ -NO<sub>2</sub> complex. The lowest value of  $l$  is 0 for  ${}^1A_1$ , 1 for  ${}^1B_1$  and  ${}^1B_2$ , 2 for  ${}^1A_2$ . For  ${}^1A_1$  (solid red line with circles), the couplings between the  $s$  and  $f$ ,  $s$  and  $g$  partial waves are very small. For  ${}^1B_1$  (solid green line with triangles) and  ${}^1B_2$  (solid blue line with squares), since  $s$ -wave scattering is forbidden by symmetry, only couplings between  $p$ ,  $d$ ,  $f$  and  $g$  partial waves are shown. For  ${}^1A_2$  (solid pink line with stars),  $s$  and  $p$  partial wave scatterings are not allowed.

### 3.3 Cross Sections And Rate Coefficients

In this section, we present the calculated cross sections and rate coefficients for vibrational (de-)excitation of NO<sub>2</sub> for collision energies below the first resonance  $< 1.6$  eV of the  ${}^3B_1$  symmetry. The VE cross sections for changing up to two quanta are obtained for the three vibrational modes. For the symmetric stretching mode, the results for the double-quantum transition should be viewed as not very accurate, because the normal mode approximation is poor for the symmetric stretching mode as discussed above.

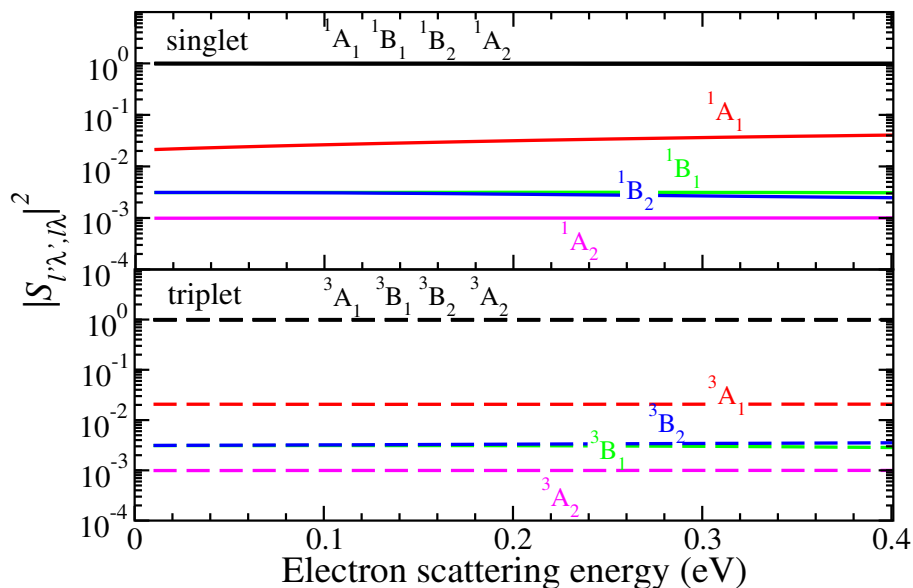


Figure 3.5: The figures show dominant (absolute value squared) elements  $|S_{l'\lambda',l\lambda}|^2$  of the scattering matrix as a function of the electron scattering energy at the  $\text{NO}_2$  equilibrium. Black lines: couplings between channels with  $\Delta l = 0$ . Color lines: couplings between channels with  $\Delta l = 1$

Figure 3.6 displays the VE cross sections for the singlet and triplet states of the  $e^- - \text{NO}_2$  complex with the target molecule being initially in the ground vibrational level. Not surprisingly, the  $1 \leftarrow 0$  cross sections of the  $e^- - \text{NO}_2$  singlet complex (solid red curves) are the largest compared to the triplet and  $2 \leftarrow 0$  transitions due to propensity rule. The  $1 \leftarrow 0$  VE cross section for triplet (dashed red curve) bending mode has the same shape as that of the singlet. Its magnitude is smaller than that for the singlet by more than a factor of 4. For the symmetric stretching mode (see Figure 3.6(b)), the  $1 \leftarrow 0$  VE cross sections for both singlet and triplet depend very weakly on the scattering energy up to 0.6 eV. Note that the  $1 \leftarrow 0$  VE cross sections for the asymmetric stretching mode are zero due to the symmetry of the scattering matrix with respect to positive and negative values of displacements along the mode. We plot the square of dominant fixed-nuclei S-matrix elements versus  $q_3$  as an example in Figure 3.7. As we can see, S-matrix is symmetric with respect to  $q_3$ . Thus the integral of Equation (2.53) vanishes for one quanta transition due to the symmetry forbidden of the wave

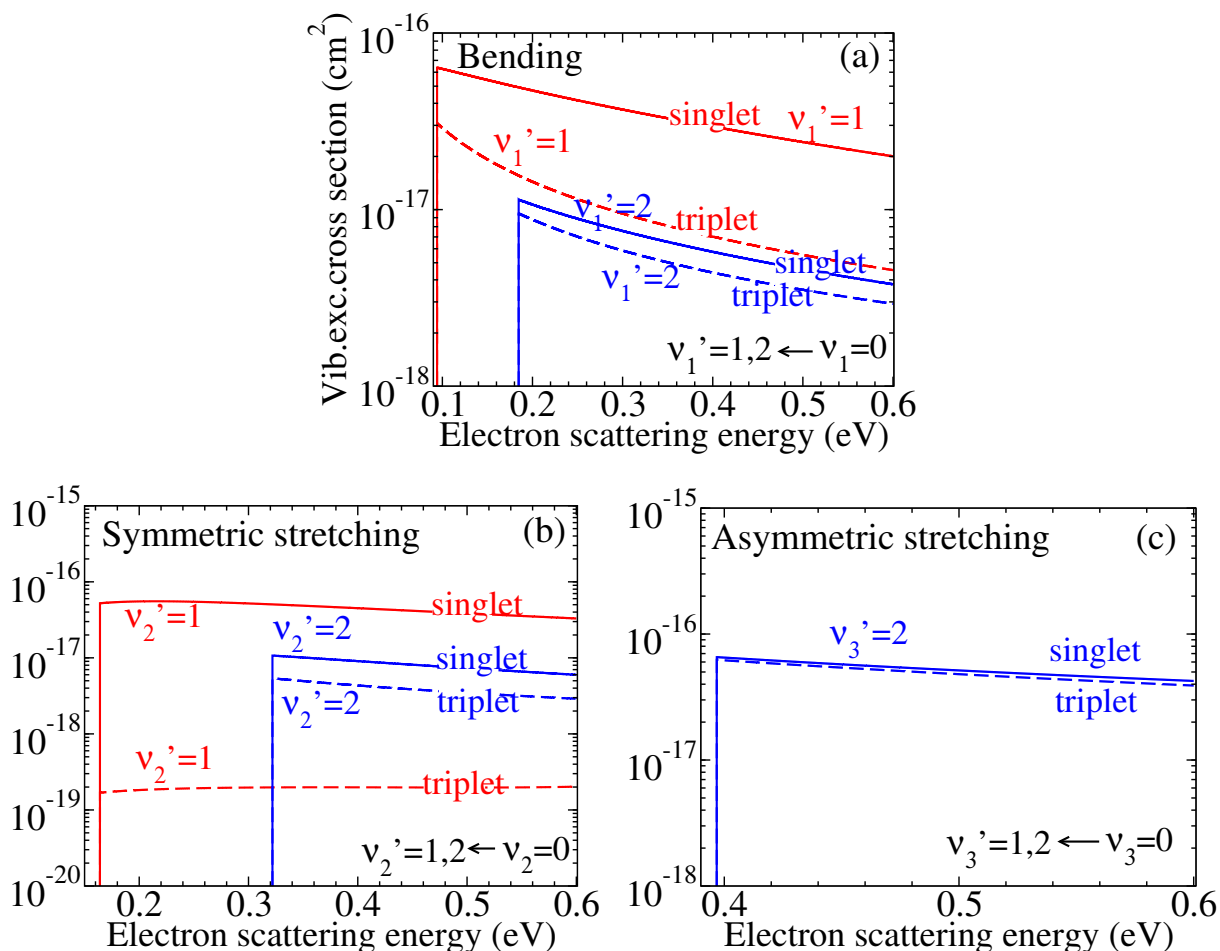


Figure 3.6: Calculated cross sections as functions of the electron scattering energy for the vibrational excitation of NO<sub>2</sub> being initially in the lowest vibrational state  $v_i = 0$  for the three normal modes (see the text for detailed discussion): (a) cross sections for  $v_i' = 1, 2 \leftarrow v_i = 0$  transitions for bending mode; (b) for symmetric stretching mode; (c) for asymmetric stretching mode.

functions <sup>5</sup>(see Equation (2.19)). Furthermore, there is no significant difference in the magnitude of the cross sections for the symmetric stretching and asymmetric stretching modes due to the close fundamental frequencies (see Table 3.1).

<sup>5</sup>The overlap between wave functions having opposite parity (for example  $v_3 = 0$  and  $v_3 = 1$ ) is suppressed, since the wave function of  $v_3 = 0$  and S-matrix are even-parity functions with respect to  $q_3$  and the wave function of  $v_3 = 1$  is an odd-parity function.

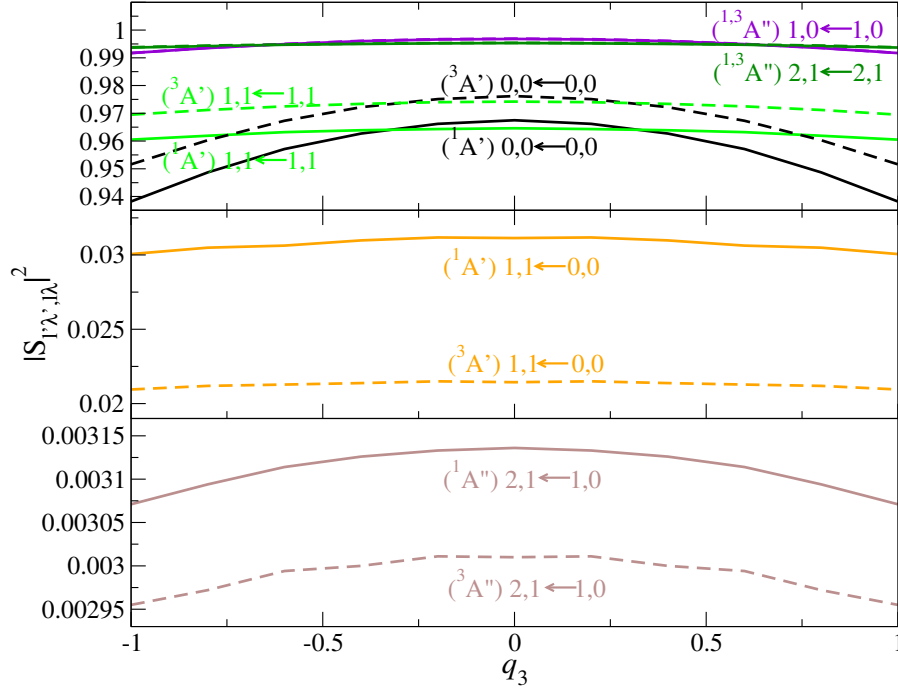


Figure 3.7: The figure shows dominant (absolute value squared) elements  $|S_{l'\lambda',l\lambda}|^2$  of the scattering matrix as a function of normal coordinate  $q_3$  (asymmetric stretching mode) at 0.3 eV scattering energy. Solid curve: singlet for  $\text{NO}_2 + e^-$  system. Dashed curve: triplet for  $\text{NO}_2 + e^-$  system. The corresponding symmetry is indicated in parentheses. The numbers indicate different partial waves  $l', \lambda' \leftarrow l, \lambda$ .

In addition, as mentioned in Section 2.2.3, the VE cross section for changing only one quanta can also be calculated by computing the square of the derivative of fixed nuclei S-matrix element,  $S_{l'\lambda',l\lambda}$ . Choosing the  $v_1 = 0 \rightarrow v_1' = 1$  cross sections for bending mode as an example, we display the comparison between the present result and that one calculated from Equation (2.61) in Figure 3.8. The derivative of fixed-nuclei S-matrix here is computed using the finite difference method with two points :  $q_1 = 0.2$  and  $q_1 = 1$ . As we can see in this figure, the cross section calculated by the analytical formula (2.61) (simple formulation) agree well with the cross section calculated numerically and discussed in Section 3.2 for triplet (the deviation is less than 10%). In the case of singlet, the VE cross section calculated by Equation (2.61) (green solid curve) is larger than

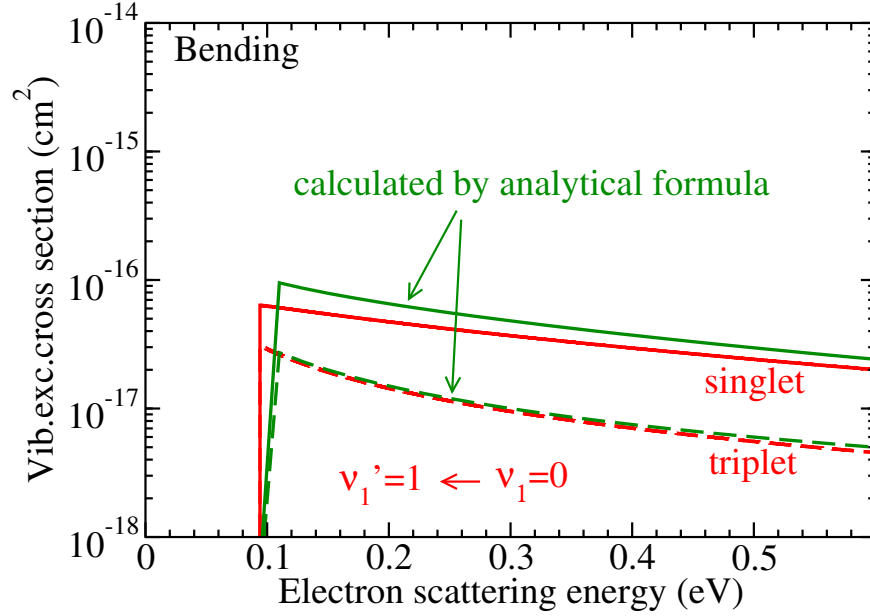


Figure 3.8: Comparison between the presently calculated  $v_1 = 0 \rightarrow v'_1 = 1$  cross sections (red curves) for bending mode and that one calculated from Equation (2.61) (green curves) with two normal coordinate values of  $q_1$  at 0.2 and 1 respectively.

the numerical one (red solid curve) by about 30%. We therefore plot the dominant fixed-nuclei S-matrix element  $S_{l'\lambda',l\lambda}$  versus  $q_1$  to give an idea about this deviation in Figure 3.8. Figure 3.9 displays the S-matrix for triplet (upper figure) and singlet (bottom figure) respectively. The left panels in Figure 3.9 are the real parts of S-matrix, and the right panels are the imaginary parts of S-matrix. In the upper Figure 3.9, we see oscillations for the S-matrix elements of triplet. However we found that the maximum deviation of the S-matrix elements along  $q_1$  is less than 2%, for the middle panels ( $S_{00,00}$  versus  $q_1$ ), which implies the S-matrix elements are in fact linear. Therefore, the derivative approximation for triplet is reasonable. For singlet, in the lower Figure 3.9, the S-matrix elements seems smooth with respect to  $q_1$ . However, if we compute the forward difference of all the  $S_{l'\lambda',l\lambda}$ , as shown in Figure 3.10, we can find that the derivative of S-matrix element for singlet is in fact depending on  $q_1$ . If we take  $q_1$  at  $q_1 = 0.2$  and  $q_1 = 1$  in singlet, it will give us a different slope from other set of  $q_1$  points. This can explain the overestimation of the S-matrix

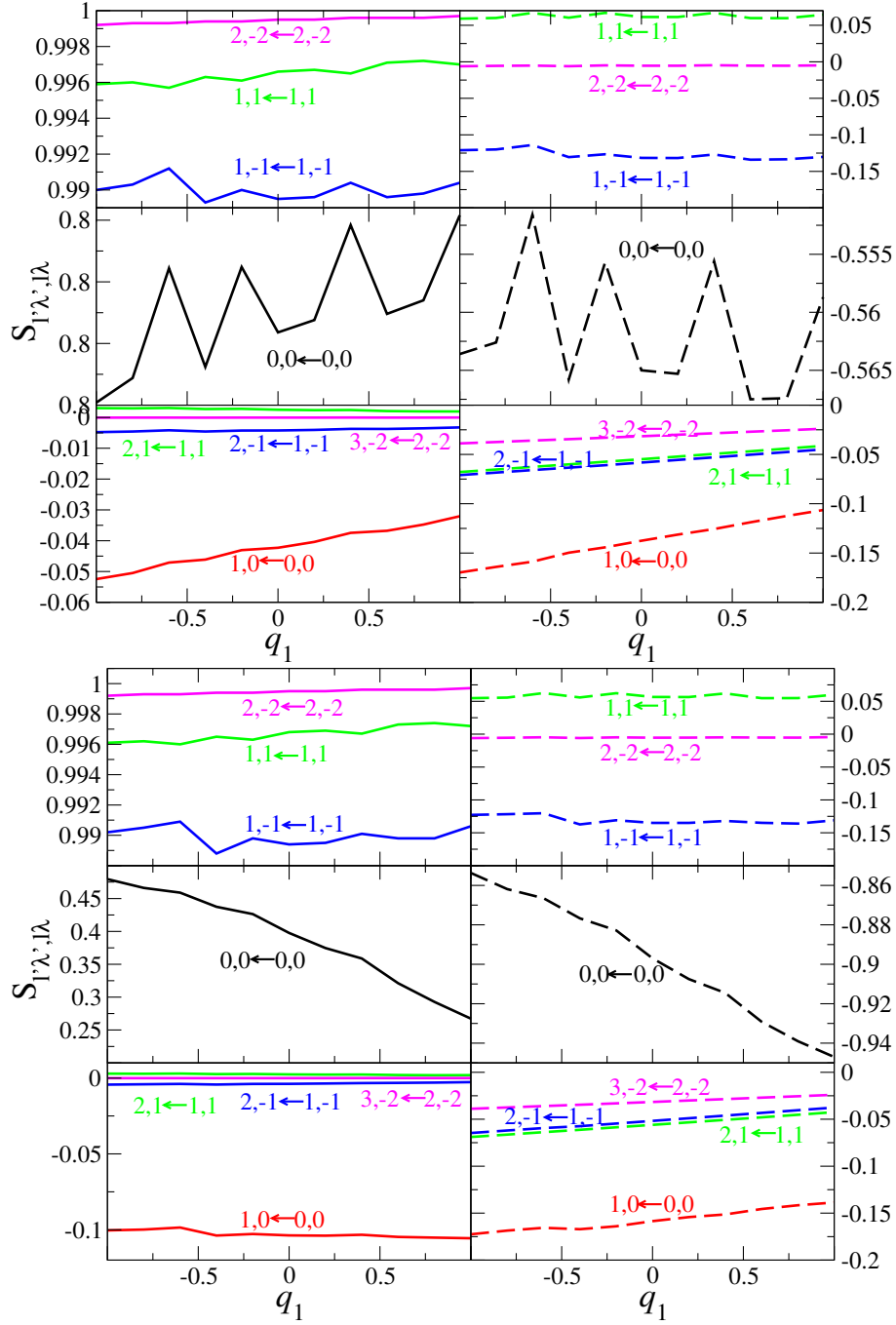


Figure 3.9: The figures show dominant elements  $S_{l'\lambda',l\lambda}$  of the scattering matrix as a function of normal coordinate  $q_1$  (bending mode) at 0.3 eV scattering energy. Upper figure: S-matrix elements for triplet . Lower figure: S-matrix elements for singlet. Solid curve: the real parts of S-matrix elements. Dashed curve: the imaginary parts of S-matrix elements. The numbers indicate different partial waves  $l', \lambda' \leftarrow l, \lambda$ .

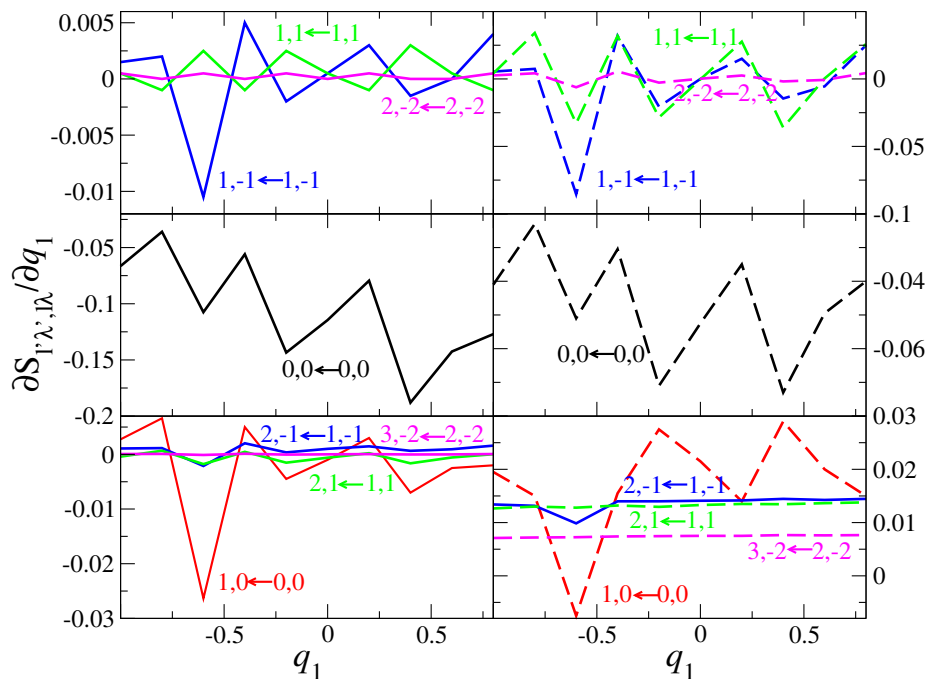


Figure 3.10: The figure shows the derivatives of dominant elements  $S_{l'\lambda',l\lambda}$  versus the normal coordinate  $q_1$  at 0.3 eV scattering energy. Solid curve: the real parts of S-matrix elements. Dashed curve: the imaginary parts of S-matrix elements. The numbers indicate different partial waves  $l', \lambda' \leftarrow l, \lambda$ .

derivative and, hence, in the cross section of Figure 3.8. To conclude, the VE cross section for singlet calculated by Equation (2.61) is somewhat larger than the present result. However, the analytical formula (2.61) apparently can provide one another efficient approach to compute the VE cross section with one quanta transition.

The thermally averaged rate coefficient  $\alpha_{v_i'v_i}(T)$  for VE of  $\text{NO}_2$  is obtained by Equation (2.62) from the energy-dependent cross sections of Equation (2.55). It should be noted that as  $\text{NO}_2$  is an open-shell molecule, the multiplicity of  $(\text{NO}_2 + e^-)$  system is 1 or 3 (more details can be found in Section 2.1.2). The rate coefficient is therefore first calculated separately for singlet and triplet transitions and then the final rate coefficient is obtained taking into account the corresponding

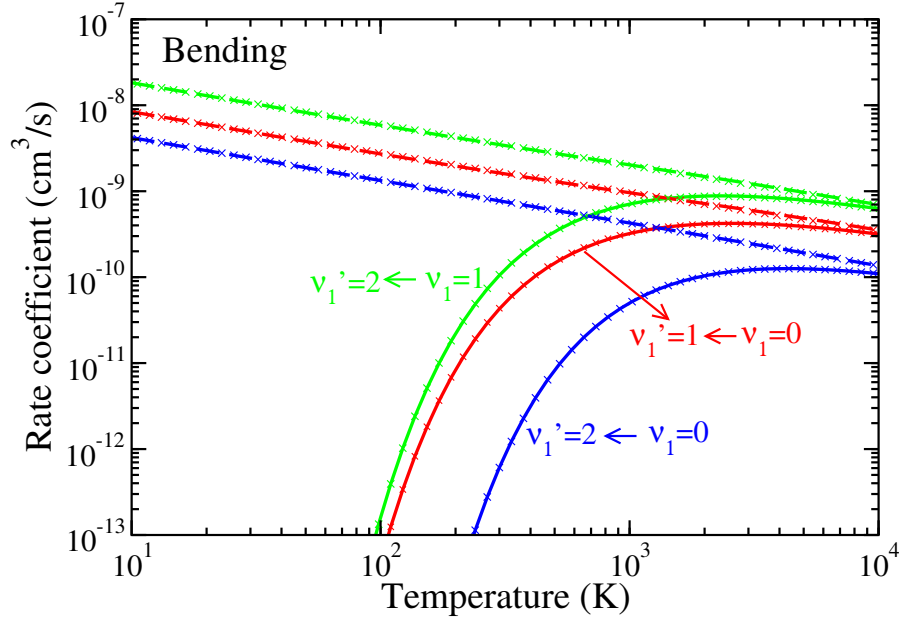


Figure 3.11: Spin- and thermally-averaged rate coefficients for (de-)excitation transitions between the three lowest vibrational states of the bending mode. Vibrational excitations are labeled by  $v_i' \leftarrow v_i$ . Corresponding de-excitations are shown by dashed lines of the same color. The figure also demonstrates the quality of the fit of Equation (3.3): Fitted curves are shown by stars with the same color for each transition.

statistical weights: 1/4 for singlet and 3/4 for triplet as

$$\alpha_{v_i', v_i}(T) = \frac{1}{4} \alpha_{v_i', v_i}^{singlet}(T) + \frac{3}{4} \alpha_{v_i', v_i}^{triplet}(T). \quad (3.2)$$

Figure 3.11 displays the spin- and thermally-averaged rate coefficients for (de-)excitation transitions between the three lowest vibrational states of the bending mode as an example. For  $T > 400$  K, the rate coefficient for one quanta transition increase rapidly from about  $10^{-10}$  to  $10^{-8}$   $\text{cm}^3/\text{s}$ .

Similarly to the previous studies [75, 96] for conveniently using the computed rate constants in plasma depollution models, we fitted the numerical spin- and thermally-averaged rate coefficients

to the following analytical formula

$$\alpha_{\nu_i'\nu_i}^{fit}(T) = \frac{1}{\sqrt{T}} e^{-\frac{\Delta_{\nu_i'\nu_i}}{T}} P_{\nu_i'\nu_i}^{fit}(x), \quad (3.3)$$

where

$$P_{\nu_i'\nu_i}^{fit}(x) = a_0 + a_1x + a_2x^2 \quad \text{and} \quad x = \ln(T). \quad (3.4)$$

The quantity  $P_{\nu_i'\nu_i}^{fit}(x)$  is the (de-)excitation probability. It depends weakly on the scattering energy. The temperature in the above equation should be in kelvin. In Equation (3.3),  $\Delta_{\nu_i'\nu_i}$  is the threshold energy defined as

$$\Delta_{\nu_i'\nu_i} = \begin{cases} E_{\nu_i'} - E_{\nu_i} > 0 & \text{for excitation,} \\ 0, & \text{for (de-)excitation.} \end{cases} \quad (3.5)$$

The numerically fitted values of coefficients  $a_i$  ( $i = 0, 1, 2$ ) for each individual transitions  $\nu_i' \leftarrow \nu_i$  are listed in Tables 3.3, 3.4, 3.5. Figure 3.11 also demonstrates the fitted curves by Equation (3.3). These curves are displayed in stars with same color for each transition obtained numerically. Evidently, the fitting curves exhibit a good agreement with that numerically obtained. The coefficient  $a_0$  of the  $1 \leftarrow 0$  transition for symmetric stretching mode is negative because the behavior of the cross section is not  $\varepsilon^{-1}$  as shown in Figure 3.6(b).

Table 3.3: Parameters  $a_0$ ,  $a_1$  and  $a_2$  of the polynomial  $P_{\nu_i'\nu_i}^{fit}(x)$  of Equation (3.3) and (3.4) between the three lowest vibrational states of bending mode. The pairs of the final and initial vibrational levels for each normal mode are at the second line in each header of the three tables. The third line in each header gives the threshold energies  $\Delta_{\nu_i'\nu_i}$  in Equation (3.5).

$\nu_i' \leftarrow \nu_i$	$1 \leftarrow 0$	$2 \leftarrow 0$	$0 \leftarrow 1$	$2 \leftarrow 1$	$0 \leftarrow 2$	$1 \leftarrow 2$
$\Delta_{\nu_i'\nu_i}(\text{K})$	1092	2142	0	1050	0	0
$a_0$	$1.98 \times 10^{-8}$	$1.25 \times 10^{-8}$	$2.66 \times 10^{-8}$	$4.33 \times 10^{-8}$	$1.33 \times 10^{-8}$	$5.75 \times 10^{-8}$
$a_1$	$1.47 \times 10^{-9}$	$2.17 \times 10^{-10}$	$-4.13 \times 10^{-10}$	$3.75 \times 10^{-9}$	$6.17 \times 10^{-12}$	$-2.96 \times 10^{-10}$
$a_2$	$1.65 \times 10^{-11}$	$-1.09 \times 10^{-11}$	$1.40 \times 10^{-10}$	$-1.03 \times 10^{-10}$	$3.10 \times 10^{-12}$	$1.67 \times 10^{-10}$

Table 3.4: Same as Table 3.3 for symmetric strctching mode

$v_i' \leftarrow v_i$	$1 \leftarrow 0$	$2 \leftarrow 0$	$0 \leftarrow 1$	$2 \leftarrow 1$	$0 \leftarrow 2$	$1 \leftarrow 2$
$\Delta_{v_i'/v_i}(\text{K})$	1904	3735	0	1831	0	0
$a_0$	$-3.32 \times 10^{-9}$	$1.48 \times 10^{-8}$	$1.58 \times 10^{-8}$	$2.92 \times 10^{-8}$	$1.56 \times 10^{-8}$	$5.79 \times 10^{-8}$
$a_1$	$4.24 \times 10^{-9}$	$2.46 \times 10^{-10}$	$-9.05 \times 10^{-10}$	$7.34 \times 10^{-9}$	$1.77 \times 10^{-11}$	$-5.71 \times 10^{-10}$
$a_2$	$-4.28 \times 10^{-11}$	$-1.35 \times 10^{-10}$	$2.81 \times 10^{-10}$	$-2.54 \times 10^{-10}$	$1.84 \times 10^{-12}$	$2.60 \times 10^{-10}$

Table 3.5: Same as Table 3.3 for asymmetric stretching mode. The  $\Delta v = 1$  transitions for asymmetric stretching mode are forbidden by symmetry.

$v_i' \leftarrow v_i$	$1 \leftarrow 0$	$2 \leftarrow 0$	$0 \leftarrow 1$	$2 \leftarrow 1$	$0 \leftarrow 2$	$1 \leftarrow 2$
$\Delta_{v_i'/v_i}(\text{K})$	2346	4604	0	2257	0	0
$a_0$	—	$2.03 \times 10^{-7}$	—	—	$1.81 \times 10^{-7}$	—
$a_1$	—	$-5.45 \times 10^{-9}$	—	—	$3.63 \times 10^{-10}$	—
$a_2$	—	$2.40 \times 10^{-10}$	—	—	$-1.22 \times 10^{-10}$	—

### 3.4 Uncertainty Estimation

To the best of our knowledge, there is no experimental or theoretical VE cross sections and rate coefficients data available for comparison with the present results. Hence, the uncertainty estimations for the theoretical model are very important to validate the present results. There are 2 kinds of uncertainty: one is the electronic structure as discussed in Section 3.2 and the other is scattering calculation by changing different parameters.

From a point of view of an electro-static model potential for the electron-NO<sub>2</sub> collisions, the major contribution to the scattering amplitude for vibration excitation is expected to be due to variations of the permanent dipole moment and the polarizabilities of NO<sub>2</sub> along the normal mode coordinates. We don't use the model potential method in this study: The accuracy of the final cross sections depends on the accuracy of wave functions of the target and the scattering electron. The

accuracy of computed wave functions cannot be compared with previous results directly. However, comparing the dipole moment, evaluated from wave functions of the target molecule, with the available accurate data can give an idea about the accuracy of computed wave functions used in the R-matrix calculations and, correspondingly, about the accuracy of the final cross sections. Here, we investigate the stability of the dipole moment of target molecule as an example by performing a complete R-matrix calculation with different active spaces and basis sets and compare the results with experimental data. We carried out two set of computations: (1) using the CAS (referred here as CAS4) mentioned in Section 3.2 and increasing the size of basis sets; (2) increasing the complete active space (CAS) with the *cc*-pVTZ basis set. The obtained results at the equilibrium geometry using the various parameters are illustrated in Figure 3.12. As one can see in Figure 3.12 (a), the dipole moment approaches the experimental value 0.316 D [94] when we increase the basis set. Evidently, the dipole moment obtained by *cc*-pVTZ basis set used in this study agrees with the experimental data very well. Augmented (aug-) basis sets are not used as they would significantly extend outside the R-matrix sphere. Figure 3.12 (b) displays the variation of dipole moment as a function of different CAS's for the *cc*-pVTZ basis set. Obviously, the CAS used currently, i.e. CAS4 corresponds to the dipole moment closest to the experimental data. Therefore, we concluded that the target properties obtained by Quantemol-N are well converged and accurately represented. It might also be desirable to provide uncertainties for other intermediate quantities computed in collisional studies, such as eigenphase sums. These are also shown in Figure 3.12, panel (c). As shown in the figure, the small shift observed in calculations with different CAS's indicates the convergence of the scattering data.

Another source of the uncertainty is the accuracy of the S-matrix derived from the UKRmol suite, when the dipole term (Equation (2.21)) is included in the interaction. As reported in Ref. [97], the presence of the dipole moment induces a strong anisotropy in the electronic potential, which reflects in an increase of the difference in S-matrix and stronger electronic couplings. It is respon-

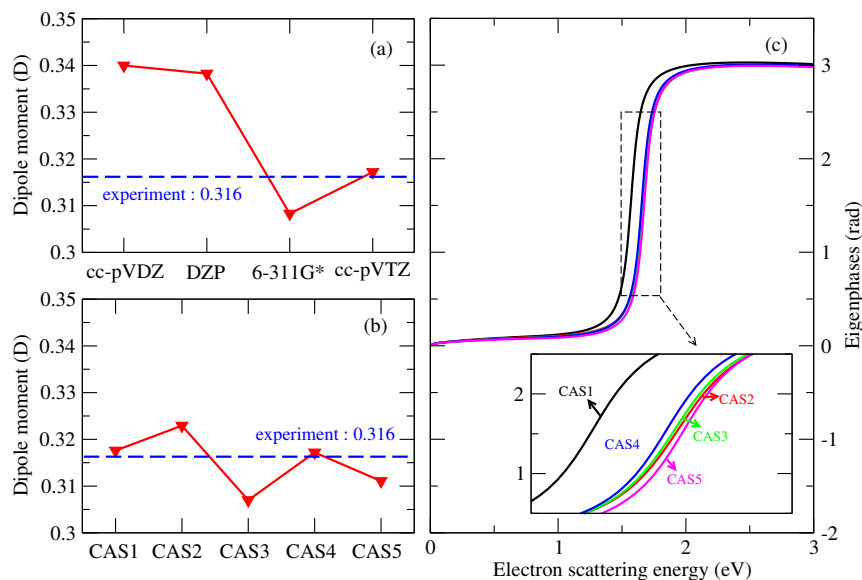


Figure 3.12: Variation of the computed permanent dipole moment of NO<sub>2</sub> versus different basis sets (panel (a)) and CAS (panel (b)). CAS1: 7 electrons are kept free in the active space including 7 orbitals; CAS2: 9 electrons are kept free in the active space including 8 orbitals; CAS3: 11 electrons are kept free in the active space including 9 orbitals; CAS4 (CAS used in this work): 13 electrons are kept free in the active space including 10 orbitals; CAS5: 15 electrons are kept free in the active space including 11 orbitals. The blue dashed line indicates the experimental value of the dipole moment. (c) The eigenphase sums of scattering of the <sup>3</sup>B<sub>1</sub> symmetry of the e<sup>-</sup>-NO<sub>2</sub> complex as a function of the electron scattering energy for different CAS's. The inset enlarges the region where a sharper energy-dependence is observed around 1.6 eV corresponding to a resonance.

sible for an increase of the HCO<sup>+</sup> DR cross section. Therefore, it is necessary to confirm that if the weak dipole-electron interaction in the present study makes a significant contribution to the final cross sections.

For the electron scattering by a non-polar molecule, the electronic angular momenta  $l$  are decoupled at large distances from the target, such that  $l$  is a good quantum number for large separations between the electron and the molecule. However, for a dipolar molecule the electronic angular momenta  $l$  are coupled at long, as at short distances. For this reason, we cannot use the specified basis of electronic states to represent the electronic Hamiltonian of the system. We stress that the dipolar

interaction exhibits the same long-range behavior as the centrifugal potential, thus, it is possible to combine the dipole and centrifugal terms, i.e. potentials with asymptotic behavior  $\frac{l(l+1)}{2r^2} - \frac{\hat{\mu}}{r^2}$ , where  $r$  is the radial electronic coordinates,  $\mu$  is the dipole moment of NO<sub>2</sub> and  $l$  is an integer. The Schrödinger equation for an electron in a dipole field is therefore given by (in atomic units<sup>6</sup>).

$$\left( -\frac{1}{2} \frac{d^2}{dr^2} + \left( \frac{\hat{L}^2}{2r^2} - \frac{\hat{\mu}}{r^2} \right) - E \right) \psi(\theta, \phi) = 0 \quad (3.6)$$

where  $\hat{L}$  is the angular momentum operator<sup>7</sup> and  $E$  is the total energy of the system. If we expand the dipole operator  $\hat{\mu}$  in spherical tensor and assume  $\mu$  is constant for any  $q$ , the problem can be reduced to the diagonalization of the angular part of electronic Hamiltonian with the form

$$\hat{H} = \begin{pmatrix} 0 & \frac{\langle Y_{0,0} | \mu \cos \theta | Y_{1,0} \rangle}{r^2} \\ \frac{\langle Y_{1,0} | \mu \cos \theta | Y_{0,0} \rangle}{r^2} & \frac{1}{r^2} \end{pmatrix} \quad (3.7)$$

where  $\theta$  is the azimuthal angle of the electron in the molecular coordinate system. Here we show the  $s\sigma - p\pi$  part of the electronic Hamiltonian as an example (in fact for <sup>1</sup>A<sub>1</sub> symmetry the  $\hat{H}$  should be a 9 × 9 matrix and for <sup>1</sup>A<sub>2</sub> symmetry it should be a 4 × 4 matrix etc.). We can obtain the effective angular momentum by compute the eigenvalues of Equation (3.7) and corresponding eigenvectors can be used to transform S-matrix in new channel states. According to the table of spherical harmonics [98], we know that  $Y_{1,0} = \sqrt{\frac{3}{4\pi}} \cos \theta$ , the  $\mu \cos \theta$  can thus be written in terms of  $Y_{1,0}$ . The numerator in the non-diagonal elements can be easily evaluated by (see Equation (107.14) in the page 444 of Ref. [99])

$$\langle Y_{l',\lambda'} | Y_{1,0} | Y_{l,\lambda} \rangle = (-1)^\lambda i^{-l+l'+1} \begin{pmatrix} l & 1 & l' \\ -\lambda & 0 & \lambda' \end{pmatrix} \begin{pmatrix} l & 1 & l' \\ 0 & 0 & 0 \end{pmatrix} \sqrt{\frac{(2+1)(2l+1)(2l'+1)}{4\pi}} \quad (3.8)$$

---

<sup>6</sup>The dipole moment  $\mu$  of NO<sub>2</sub> in atomic unit is 0.12431 ( $\mu = 0.316$  Debye/2.542)

<sup>7</sup> $\hat{L}^2 Y_{l\lambda} = l(l+1) \hbar^2 Y_{l\lambda}$

Table 3.6: Coefficients from the curves fitting  $|S_{l'\lambda',l\lambda}|^2 = \beta E^\alpha$  and  $|\tilde{S}_{l'\lambda',l\lambda}|^2 = \beta' E^{\alpha'}$  ( $E$  is in eV).

$l'\lambda' \leftarrow l\lambda$	$\beta$	$\alpha$	$\beta'$	$\alpha'$
00 $\leftarrow$ 00	$1.00 \times 10^0$	$1.82 \times 10^{-3}$	$1.00 \times 10^0$	$1.56 \times 10^{-3}$
10 $\leftarrow$ 00	$2.84 \times 10^{-2}$	$6.40 \times 10^{-2}$	$4.54 \times 10^{-2}$	$1.86 \times 10^{-1}$
20 $\leftarrow$ 00	$4.21 \times 10^{-5}$	$1.01 \times 10^{-1}$	$1.98 \times 10^{-5}$	$1.90 \times 10^{-1}$
22 $\leftarrow$ 00	$4.30 \times 10^{-3}$	$9.34 \times 10^{-1}$	$4.34 \times 10^{-3}$	$9.34 \times 10^{-1}$
20 $\leftarrow$ 10	$4.07 \times 10^{-3}$	$1.14 \times 10^{-3}$	$8.01 \times 10^{-3}$	$1.46 \times 10^{-3}$
30 $\leftarrow$ 20	$1.77 \times 10^{-3}$	$7.61 \times 10^{-4}$	$3.53 \times 10^{-3}$	$3.28 \times 10^{-4}$
40 $\leftarrow$ 30	$9.84 \times 10^{-4}$	$6.28 \times 10^{-4}$	$1.96 \times 10^{-3}$	$3.83 \times 10^{-4}$
32 $\leftarrow$ 00	$7.42 \times 10^{-6}$	$1.06 \times 10^0$	$1.05 \times 10^{-6}$	$1.10 \times 10^0$
42 $\leftarrow$ 00	$2.43 \times 10^{-9}$	$1.12 \times 10^0$	$7.23 \times 10^{-10}$	$7.50 \times 10^{-1}$
44 $\leftarrow$ 00	$1.25 \times 10^{-7}$	$1.92 \times 10^0$	$1.26 \times 10^{-7}$	$1.92 \times 10^0$

where the triangular inequalities:

$$|l - l'| \leq 1 \leq l + l' \quad (3.9)$$

should be obeyed and the sum  $l + 0 + l'$  must be even. The 3-j symbols in Equation (3.8) can be conveniently calculated by calculator on internet: [100]. We will find that most of the calculated<sup>8</sup> non-diagonal elements are zero. When we diagonalize the Hamiltonian for each symmetry, the values of the effective angular momentum  $l$  could be non-integer and even complex.

The eigenvectors of matrix (3.7) are used to build the unitary matrix to transform the scattering matrix into the effective angular momentum representation. On the next step, we fitted the obtained S-matrix elements (absolute values squared) before  $|S_{l'\lambda',l\lambda}|^2$  and after  $|\tilde{S}_{l'\lambda',l\lambda}|^2$  the unitary transformation with power law:  $|S_{l'\lambda',l\lambda}|^2 = \beta E^\alpha$  and  $|\tilde{S}_{l'\lambda',l\lambda}|^2 = \beta' E^{\alpha'}$ , respectively, where  $\alpha$ ,  $\beta$  and  $\alpha'$ ,  $\beta'$  are the fitted parameters. The obtained parameters are listed in Table 3.6. Figure 3.13 shows a few examples of scattering matrix elements of dominant channels ( $\Delta l \leq 2$  and  $\lambda$  is

<sup>8</sup>The results should finally be divided by the factor of  $Y_{1,0}$ , i.e.  $\sqrt{\frac{3}{4\pi}}$ .

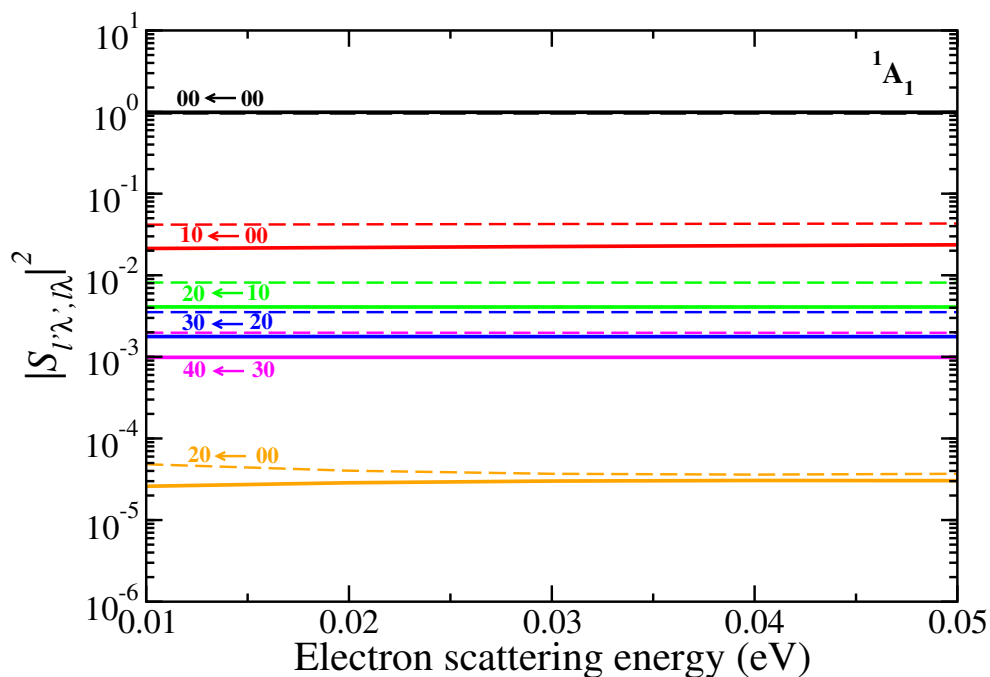


Figure 3.13: The figure compares selected values of the  ${}^1A_1$  scattering matrix elements (absolute value squared) before (solid color lines) and after (dashed lines of the same color) the unitary transformation that eliminates the long-range dipolar coupling between asymptotic channels in the  $e^-$ - $\text{NO}_2$  scattering matrix in the body frame. See the detailed discussion in the text. Each curve is labeled at the left of the figure with the pair of indexes ( $l'\lambda' \leftarrow l\lambda$ ), corresponding to the final channels and initial channel. The results for other irreps are not displayed but the situation is very similar to the  ${}^1A_1$  symmetry.

zero) of the  ${}^1A_1$  symmetry at equilibrium. The largest matrix element for the  $00 \leftarrow 00$  transition is unchanged after the unitary transformation. It is the variation of this matrix element with respect to the normal coordinates that gives the largest contribution to the cross sections. Therefore, the uncoupling the partial-wave channels at large distances would not produce a significant change in the final cross sections. This also means that the coupling between partial waves induced by the permanent dipole moment of the target has a minor effect on the final cross sections.

Assuming that the order of magnitude of the vibrational excitation cross sections is determined by the square of the derivatives of the permanent dipole moment and polarizabilities of the target

with respect to the normal coordinates, and also assuming that the relative uncertainties of the derivatives are of the same order as the relative uncertainties of the dipole moment, we can estimate the uncertainty of the obtained cross sections with respect to the accuracy of the wave functions of the target. From panels (a) and (b) in Figure. 3.12, we estimate that the uncertainty in the dipole moment of NO<sub>2</sub> is less than 2%, producing the uncertainty in cross sections less than 4%. Another source of uncertainty in the final cross sections is due to the variation of the geometry-fixed scattering matrix with energy. The choice of the energy at which the scattering matrix  $S_{l'l',l\lambda}(\mathbf{q})$  in Equation (2.53) is computed produces the corresponding uncertainty. Figure 3.5 gives an idea about the energy variation of  $S_{l'l',l\lambda}(\mathbf{q})$ . The largest components with  $\Delta l = 0$  vary for about 3% over the energy interval of 0.4 eV. It gives an uncertainty in the cross sections of the order of 6%. No other significant uncertainty sources were identified. Therefore, the overall uncertainty of the present calculations seems to be below 10%.

### 3.5 Conclusions

This chapter reported the first theoretical results on vibrational (de-)excitation of the NO<sub>2</sub> ( $X^2A_1$ ) molecule in collisions with a low-energy electron. The calculation is performed using an approach that combines the normal mode approximation for the vibrational states of the target, the R-matrix method, and the vibrational frame transformation. Cross sections and spin- and thermally-averaged rate coefficients are obtained for excitation of all three NO<sub>2</sub> modes by one and two quanta from the ground vibrational level.

In addition, extensive uncertainty estimations were performed by changing the basis sets and orbital spaces in the R-matrix calculations. Converged results for the target properties and eigenphase sums demonstrated the validity of the obtained results. We expect that the data reported in the present study could be valuable in kinetic studies of low-temperature NO<sub>2</sub>-containing plasma.

Moreover, we expect that our approach will also work for other triatomic molecules of atmospheric interest and have similar symmetry and electronic properties to  $\text{NO}_2$ , such as  $\text{SO}_2$ ,  $\text{O}_3$  and the  $\text{N}_2\text{O}$  molecule which will be investigated in Chapter 4.

## CHAPTER 4: CROSS SECTIONS AND RATE COEFFICIENTS FOR VIBRATIONAL (DE-) EXCITATION OF N<sub>2</sub>O BY ELECTRON IMPACT

Theoretical study of vibrational (de-)excitation of N<sub>2</sub>O by low-energy electron impact is carried out in this chapter. This study is in the continuity of the one done on NO<sub>2</sub>, on where we applied our theoretical model introduced in Chapter 2 to compute cross sections and rate coefficients for transitions between the lowest vibrational levels. The theoretical approach employs the normal mode approximation (Section 2.1.3) for the description of target vibrational states, the vibrational frame transformation (Section 2.2.3) to compute amplitudes of vibrational transitions, and the R-matrix method (Section 2.2.2) to compute *ab initio* electronic bound and continuum states. It was found that the non-adiabatic Renner-Teller effect, which couples partial waves of the incident electron with degenerate bending vibrations of N<sub>2</sub>O, is responsible for the excitation of the bending mode. Obtained theoretical results agree reasonably well with available experimental data at low energies. Thermally averaged rate coefficients are computed for temperatures in the 10-10000 K range. The following work has been published in *Physical Review A* [101].

### 4.1 Introduction

As introduced in Equation (1.3), vibrational (de-)excitation by electron impact is a process in which an electron scatters off a molecule and exchanges energy with it in a way that leaves the molecular target in a different vibrational state. For N<sub>2</sub>O, vibrational (de-)excitation can be depicted by



in which  $v_i$  and  $v_i'$  denoted the initial and final vibrational states of N<sub>2</sub>O, respectively.

Due to the importance of nitrous oxide ( $\text{N}_2\text{O}$ ) in a plethora of research fields ranging from astrochemistry [102–104] to low temperature plasma technology [105] and medicine [106], different electron- $\text{N}_2\text{O}$  collisional processes have been experimentally and theoretically explored over the years. Differential and integrated cross sections for elastic and certain inelastic processes have been measured by several groups [89, 107–126]. Although the experimental investigations generally agree on the position of an observed resonance near 2.3-2.5 eV, they disagree on the assignment for the symmetry of the resonant state. Furthermore, there is also disagreement with respect to a second resonance observed around or above 8.0 eV. On the theoretical side, the earlier studies of Morgan [60], Sarpal *et al.* [127], and Bettega *et al.* [128] aimed at clearly specifying the nature of the two resonances observed in the experiments. Morgan and Sarpal *et al.* employed the R-matrix method with different models to study electron scattering by  $\text{N}_2\text{O}$  in its equilibrium geometry. They obtained a resonance near 2.3 eV with  $^2\Pi$  symmetry. Later on, using a slight modification of the Schwinger multichannel (SMC) method of incorporating polarization effects, Bettega [128] was able to reproduce the experimental features between the two resonances.

To our knowledge, no theoretical vibrational cross sections has been reported so far, while there are several experimental cross sections: by Hayashi and Akashi [129], Kitajima [119] *et al.* , Allan and Skalicky [121], and Nakamura [122]. A compilation of their work can be found in a recent review [130]. Hayashi and Akashi presented cross sections for electron-induced vibrational excitations from electron swarm parameters in pure  $\text{N}_2\text{O}$ . Kitajima *et al.* as well as Allan and Skalicky measured absolute differential cross sections (DCS) for the vibrationally inelastic electron scattering with a range of the electron scattering energy from the threshold region up to 20 eV. Allan and Skalicky reported the measurements only for one scattering angle  $135^\circ$  and multiplied each of the measured DSC by factor  $4\pi$  to estimate the integral cross section. Nakamura [122] derived cross sections for vibrational excitation from swarm parameters.

The present chapter represents the first theoretical vibrational excitation (VE) study of  $\text{N}_2\text{O}$  by

electron impact. We present cross sections and rate coefficients for transitions between ground and first vibrational states of  $\text{N}_2\text{O}$ . The rotational structure is also neglected in the present study. The chapter is organized as follow. In Section 4.2, we describe the theoretical approach according to Chapter 2 and computational details in our calculations. In Section 4.3, the obtained VE cross sections and corresponding rate coefficients are shown and discussed. Section 4.4 presents uncertainty estimations of the present approach, and the last section, Section 4.5, is devoted to our conclusions.

## 4.2 Theoretical Approach And Computational Details

Our approach can be summarized as follows. We start by characterizing the molecular target according to its equilibrium geometry, vibrational frequencies, and dipole moment value at equilibrium; features that can be obtained performing *ab initio* electronic bound molecular states calculations. We proceed by performing *ab initio* electronic continuum molecular states calculations to obtain a scattering matrix at different molecular geometries along the vibrational normal mode coordinates. We then transform the scattering matrix into the basis of vibrational states of the target molecule. Finally, we compute the vibrational (de-)excitation cross sections from the transformed scattering matrix.

The approach used in this chapter has been described and applied to the  $\text{NO}_2$  molecule in Chapter 2 and Section 3.2, and a more detailed narrative of the simplified model on which our approach is based can be found in Section 2.2.3 and Section 3.3 and references therein [131, 132]. Therefore, we will limit the description presented in this section to the main ingredients of the theoretical formalism – the normal mode approximation and the vibrational frame transformation – and the computational details of our calculations.

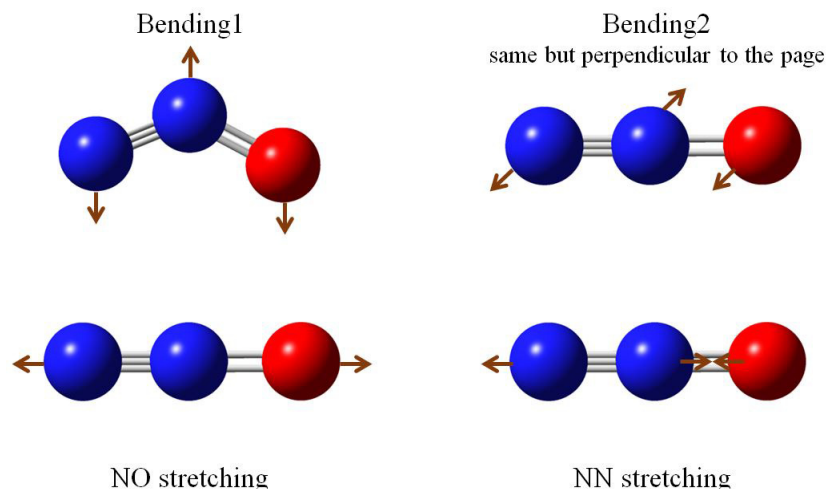


Figure 4.1: The three normal modes for  $\text{N}_2\text{O}$ . The red balls represent the O atoms and the blue balls represent the N atoms. The arrows indicate the force vectors.

At low energies around the equilibrium position, the potential energy curve of the most rigid molecules is fairly well described by the quadratic potential of a harmonic oscillator. In our approach, we describe vibrational wave functions of the molecular target using the normal mode approximation (see Section 2.1.3).  $\text{N}_2\text{O}$  has three normal modes of vibration, namely: the doubly degenerate bending mode, NO stretching, and NN stretching represented by  $\nu_1$ ,  $\nu_2$ , and  $\nu_3$ , respectively (see Figure 4.1). The approximation allows us to perform a significant part of calculations analytically. For molecules of astrophysical and low temperature plasma interest, like  $\text{N}_2\text{O}$ , only the lowest vibrational levels are significantly populated at low temperatures and the range of scattering energies needed to study vibrational excitation is within the validity of the normal mode model.

After computing the scattering matrix, we perform a vibrational frame transformation (see Section 2.2.3) to change the scattering matrix obtained for clamped nuclei for a number of molecular geometries to the vibrating-molecule picture, that the electron sees, when it is at large electronic

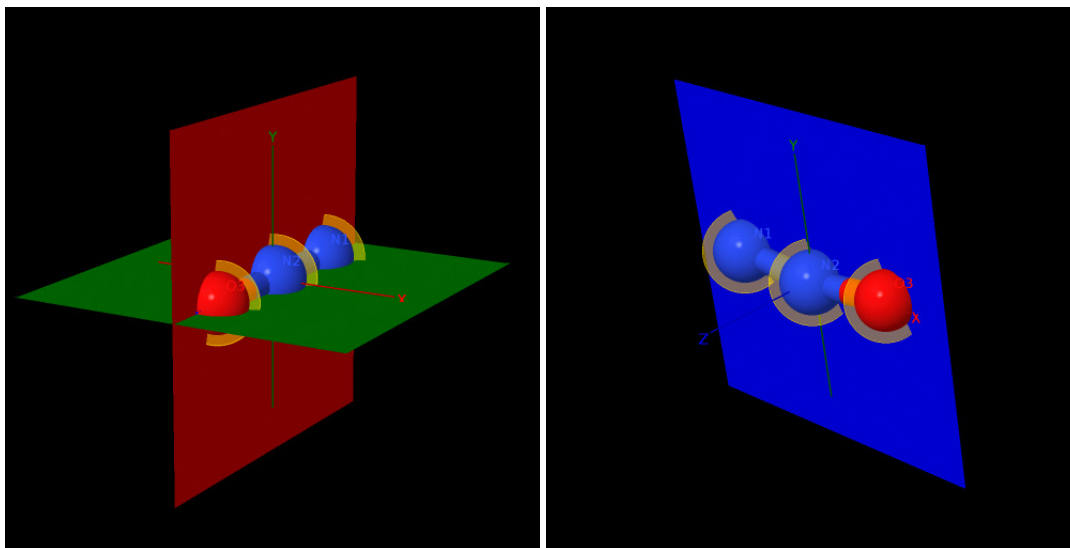


Figure 4.2: The three axes of the molecular coordinate system are chosen along the principal axes on the inertia of the molecule.

distances. The clamped nuclei basis of asymptotic channels is denoted by the channel quantum numbers  $\{l, \lambda\}$  that label the angular momentum of the incoming and outgoing electron and their respective projections on  $z$ -axis in the molecular frame coordinate system. The three axes of the molecular coordinate system are chosen along the principal axes on the inertia of the molecule, such that the quantization axis (the  $z$ -axis) is directed along the molecular axis in calculations for linear geometries as shown in the left panel in Figure (4.2). For bent geometries of the molecule, the  $z$ -axis is perpendicular to the plane of the molecule with the  $x$ -axis aligned along the axis of the smallest moment of inertia (see the right panel in Figure (4.2)). In Section 4 we introduce another set of quantum numbers  $\{l, \tilde{\lambda}\}$  and corresponding channel functions, which replace the spherical harmonic  $Y_l^\lambda$  with their real-valued combinations of  $Y_l^{\pm\lambda}$ . The vibrational frame transformation of the scattering matrix elements is then given by Equation (2.53). The physical meaning of an element of the transformed scattering matrix is the scattering amplitude from one vibrational state  $\eta_{v_i}(\mathbf{q})$  of the target molecule to another  $\eta_{v_i'}(\mathbf{q})$  as expressed by Equation (2.19). As discussed in Section 2.2.3, the vibrational frame transformation of Equation. (2.53) can only be performed if

the fixed-nuclei S-matrix element,  $S_{l'\lambda',l\lambda}$ , is a smooth function of the incident electronic energy. It means, in particular, that for this approach to be applicable, the fixed-nuclei S-matrix should not have low-energy electronic resonances. As discussed below, the lowest electronic resonance in e-NO<sub>2</sub> collisions occurs at collisions energies about 2.5 eV.

The cross section  $\sigma_{v_i'v_i}$  for vibrational (de-)excitation can be obtained from the corresponding matrix element  $S_{v_i'l'\lambda',v_i l\lambda}$  by Equation (2.55). Although the fixed-nuclei scattering matrix  $S_{l'\lambda',l\lambda}(\mathbf{q})$  is weakly-dependent on energy, the remaining energy-dependence introduces an ambiguity in the choice of the matrix in integrand of Equation (2.53). In the present calculation, we choose following procedure: Integrating over the normal mode  $\mathbf{q}$  in Equation (2.53) for a given energy  $\varepsilon$  of the electron in the incident channel (see the above equation), and at each integration point  $\mathbf{q}$ , the scattering matrix  $S_{l'\lambda',l\lambda}(\mathbf{q})$  is taken from the R-matrix calculations performed at this particular fixed-nuclei geometry  $\mathbf{q}$  and the electron-scattering energy  $E_{el}$ . Because the energy-dependence of the fixed-nuclei scattering matrix is weak below 2.5 eV, the corresponding uncertainty of the final cross section is much smaller than the uncertainty related to the choice of the *ab initio* model (discussed below). To demonstrate the energy dependence of the integrand of Equation (2.53), we also give three figures showing the integrands for the NO stretching mode for three among the largest matrix elements  $0,0 \leftarrow 0,0$ ,  $1,1 \leftarrow 1,1$ ,  $2,-2 \leftarrow 2,-2$ <sup>1</sup>. Each figure shows the integrand for one matrix element for three energies 0.3eV, 0.4eV (which are just above the vibrational excitation threshold), and 1.6eV (the energy is well above the threshold). As one can see, the energy dependence is very weak. For the  $1,1 \leftarrow 1,1$  and  $2,-2 \leftarrow 2,-2$  transitions as shown in the two lower panels in Figure (4.3), the curves for different energies are indistinguishable.

The cross section for vibrational excitation does not account for the rotational structure and can be compared with experiments or used in applications where the rotational structure of the initial and

---

<sup>1</sup>The numbers indicates  $l',\lambda' \leftarrow l,\lambda$

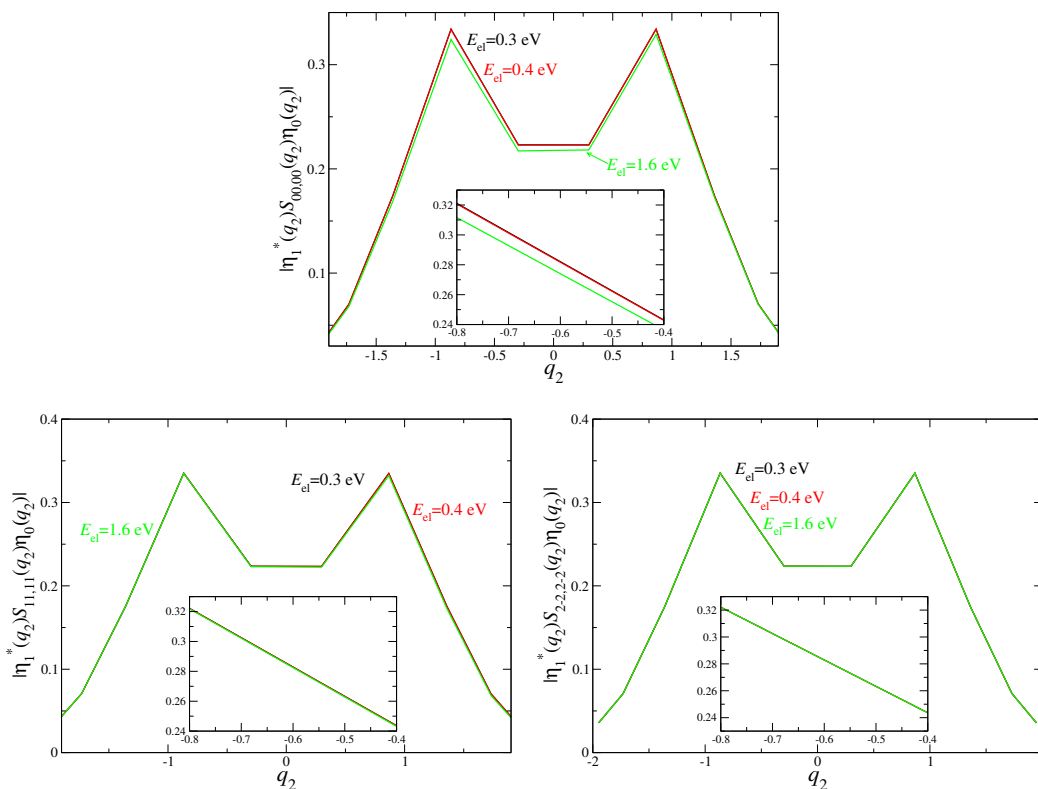


Figure 4.3: The integrands of Equation (2.53) for the NO stretching mode for three among the largest matrix elements  $0,0 \leftarrow 0,0$ ,  $1,1 \leftarrow 1,1$ ,  $2,-2 \leftarrow 2,-2$  as an example. Each figure shows the integrand for one matrix element for three energies 0.3 eV, 0.4 eV and 1.6 eV.

final vibrational levels is not important or not resolved. This is, generally, the case for the most of current experiments (including swarm measurements) and plasma applications at room or higher temperatures: With the rotational  $\text{N}_2\text{O}$  constant of  $0.41901 \text{ cm}^{-1} = 5.195 \times 10^{-5} \text{ eV}$  [133] at 300 K, at least, 25 rotational states are significantly populated.

To compute VE cross section, computational details should be introduced systematically. At its equilibrium geometry,  $\text{N}_2\text{O}$  has a linear asymmetric “N–N–O” molecular structure, described by the  $C_{\infty v}$  symmetry point group introduced in Section 2.1.2 with the ground electronic state of the  $^1\Sigma^+$  symmetry. The equilibrium geometry and the normal mode coordinates with corresponding frequencies were computed with the MOLPRO suite [42] using the Complete Active Space Self-

Table 4.1: Energies  $\hbar\omega_i$  (in eV) of N<sub>2</sub>O normal modes obtained in the present study and compared with experimental data from Ref. [94].

Mode ( $\nu_i$ )	Degeneracy	Symmetry	Experimental $\hbar\omega_i$	Calculated $\hbar\omega_i$
Bending ( $\nu_1$ )	2	$\Pi$	0.0739	0.0761
NO stretching ( $\nu_2$ )	1	$\Sigma^+$	0.1610	0.1622
NN stretching ( $\nu_3$ )	1	$\Sigma^+$	0.2830	0.2849

Consistent Field (CASSCF) method and the cc-pVTZ basis set [134] centered on each atom. N<sub>2</sub>O has 22 electrons in a closed-shell electronic ground state configuration given by

$${}^1\Sigma^+ : 1\sigma^2 2\sigma^2 3\sigma^2 4\sigma^2 5\sigma^2 6\sigma^2 1\pi^4 7\sigma^2 2\pi^4.$$

In the calculations preserving the  $C_{\infty v}$  symmetry group, the 10 electrons, which occupy the lowest five  $\sigma$  molecular orbitals, were kept frozen and the remaining 12 electrons were allowed to distribute themselves accordingly to symmetry and spin restrictions in the Complete Active Space (CAS) formed by the remaining  $6\sigma 1\pi 7\sigma 2\pi$  ground-configuration orbitals and the next 3 molecular orbitals  $8\sigma, 9\sigma, 3\pi$ , that are empty in the ground configuration. Because available quantum chemistry codes cannot handle continuous groups like  $C_{\infty v}$ , the calculations were performed in the  $C_{2v}$  group for the geometries describing NO and NN stretching displacements. For geometries, breaking the  $C_{\infty v}$  symmetry group – the bending-mode displacements – the same 10 electrons were kept frozen in the lowest five  $a'$  orbitals and the remaining 12 electrons were distributed in the  $6-12a'$  and  $1-3a''$  orbitals of the corresponding  $C_s$  symmetry group.

Upon optimization of the equilibrium geometry, the N-N and N-O bond lengths were found to be 1.131 Å and 1.186 Å, respectively, in good agreement with the experimental value 1.128 Å and 1.184 Å [94]. Table 4.1 shows a comparison between obtained normal mode frequencies and the available experimental data [94]. Our frequencies agree with a percentage difference of less than 3% with the experimental references.

After characterizing the equilibrium geometry and normal mode frequencies with MOLPRO [42], we carried out calculations of the potential energy of the ground electronic state of N<sub>2</sub>O and calculations of continuum states using the UK R-matrix code [30] with the Quantemol-N suite [71]. In order to achieve consistency with the MOLPRO calculations, we have used the same basis set and CAS. However, Quantemol-N does not have CASSCF built in it, and a series of convergence tests showed that the available Complete Active Space Configuration Interaction (CAS-CI) model with the Hartree-Fock (HF) orbitals built with MOLPRO gave the best results. Figure 4.4 displays ground state electronic potential energy curves of N<sub>2</sub>O for each normal mode obtained with Quantemol-N. For comparison, we also show potential energy curves of harmonic oscillators generated with the frequencies obtained from MOLPRO. The Quantemol-N potential energy curves agree reasonably well with the potential energies calculated in the harmonic approximation. Small discrepancies are attributed to the anharmonicity of the actual N<sub>2</sub>O potential. The permanent electric dipole moment of the target molecule obtained from the R-matrix calculation is 0.1 D, which is considered to be in satisfactory agreement with experimental value 0.16 D [94].

Using the molecular orbitals obtained from the structure calculations and the continuum Gaussian type orbitals with partial waves up to  $l \leq 4$ , we performed the electronic continuum molecular states calculations with Quantemol-N. The radius of the R-matrix sphere was set to be 11 bohrs<sup>2</sup>. All the electronic states of the target below the cutoff energy 16 eV have been included in the close-coupling (CC) expansion. From the scattering calculations we can obtain the eigenphase sums and the reactance matrix, K-matrix, at clamped nuclei.

The indicator for the efficacy of the scattering calculation is the eigenphase sums. Figure 4.5 displays the eigenphase sum of different irreducible representations at equilibrium and at displacements away from the equilibrium along each normal-mode coordinate. We can extract the position

---

<sup>2</sup>N<sub>2</sub>O is a closed shell molecule. We have verified that 11 bohrs is sufficient to obtain a convergent R-matrix calculation result.

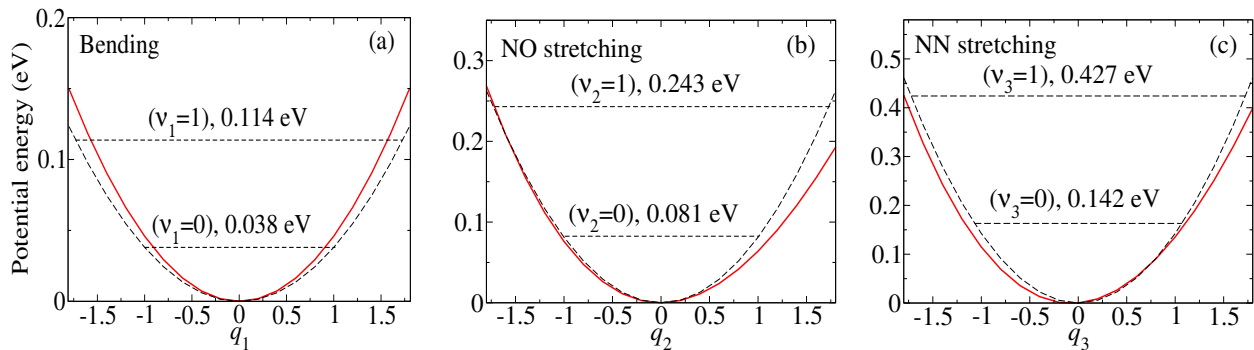


Figure 4.4: Potential energy curves for the ground electronic state of  $\text{N}_2\text{O}$  as a function of the (a) bending, (b) NO stretching and (c) NN stretching normal-mode coordinates. The abscissa axes in the figures represent dimensionless normal mode coordinates. In each panel, only one mode is varied, while the other modes are kept fixed at their equilibrium positions. Red solid curves are the actual potential energies obtained from the R-matrix code, while black dashed curves represent energies calculated in the harmonic approximation, i.e. simply  $\sim \frac{\hbar\omega_i}{2} q_i^2$ . Horizontal dashed lines denote the energies of vibrational states.

and width of calculated resonances by fitting the eigenphase sum to a Breit-Wigner form (see Equation (5.3)). At equilibrium, the lowest resonance is found at 3.0 eV and has the  $^2\Pi$  symmetry. To compare with available experimental data (the resonance around 2.3-2.5 eV [121, 135]), the zero-point energy  $\hbar(\omega_1 + 2\omega_2 + \omega_3)/2 = 0.3$  eV of the ground vibrational level should be accounted for. Therefore, in the present calculation, the energy of the resonance is 2.7 eV above the ground vibrational level. The difference with the experimental position of the resonance is attributed to the large uncertainty associated with the Born-Oppenheimer approximation used to identify the energy of the resonance in the theoretical calculation: The position of the resonance depends strongly on the choice of the fixed geometry near the  $\text{N}_2\text{O}$  equilibrium, at which the scattering calculations were performed. In addition, the width (about 1 eV) of this shape resonance is larger than the difference between the experimental and theoretical results.

The K-matrix obtained from the scattering calculations was used to compute the clamped-nuclei scattering matrix, S-matrix. Figure 4.6 displays selected dominant elements (the absolute value

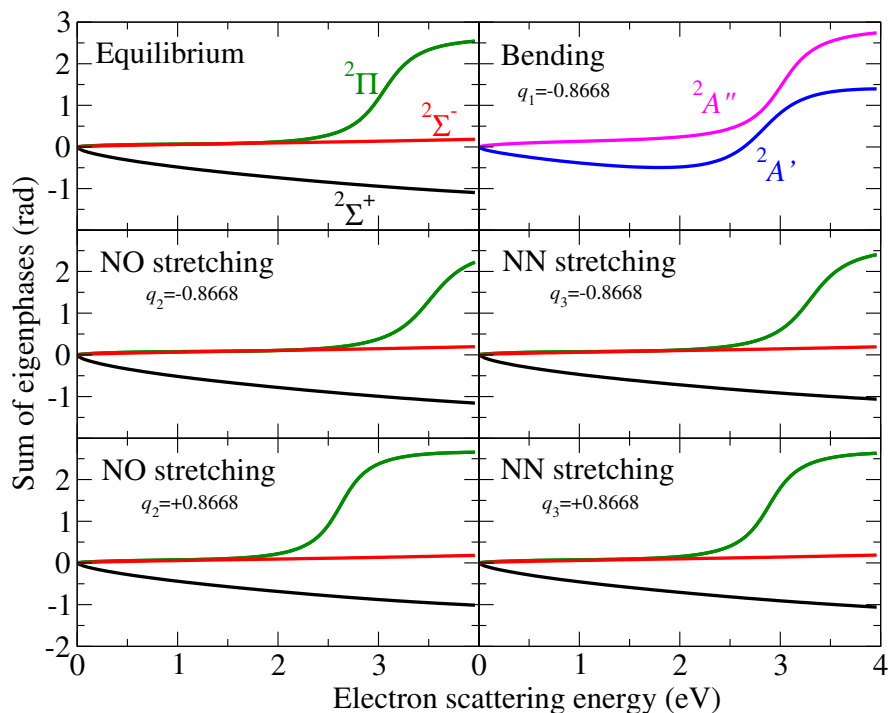


Figure 4.5: Sum of eigenphases as a function of the electron scattering energy for equilibrium geometry and displacements  $q_i = \pm 0.8668$  (dimensionless) along each normal mode. Due to the symmetry of bending mode, the eigenphase sum of  $q_1 = +0.8668$  and  $q_1 = -0.8668$  are the same. The curves are color coded according the different symmetries of the  $e^- + \text{N}_2\text{O}$  system.

squared) of the S-matrix at equilibrium geometry. In the figure (as well as in Figure 4.7 below), indices  $\tilde{\lambda}$  refer to real-valued combinations of spherical harmonics  $Y_l^{\pm\lambda}$  with positive and negative projections  $\lambda$ . The real-valued harmonics  $Y_{l\tilde{\lambda}}$  with positive  $\tilde{\lambda}$  transform as cosine-type functions with respect to the rotational angle  $\phi$  about the axis  $z$  perpendicular to the plane of the molecule, while the harmonics with negative  $\tilde{\lambda}$  transform as sine-type functions. Except for the  $S_{10,00}$  element, all other elements behave smoothly with the electronic energy below the first resonance. The minimum is observed near 0.4 eV for the  $10 \leftarrow 00$  transition. Although the  $S_{10,00}$  element has a strong energy dependence, which breaks the condition of the applicability of the vibrational frame transformation (the energy dependence should be smooth), its contribution to the VE cross section in Equation (2.55) is negligible when compared to dominant terms (diagonal over  $l\lambda$ ) and,

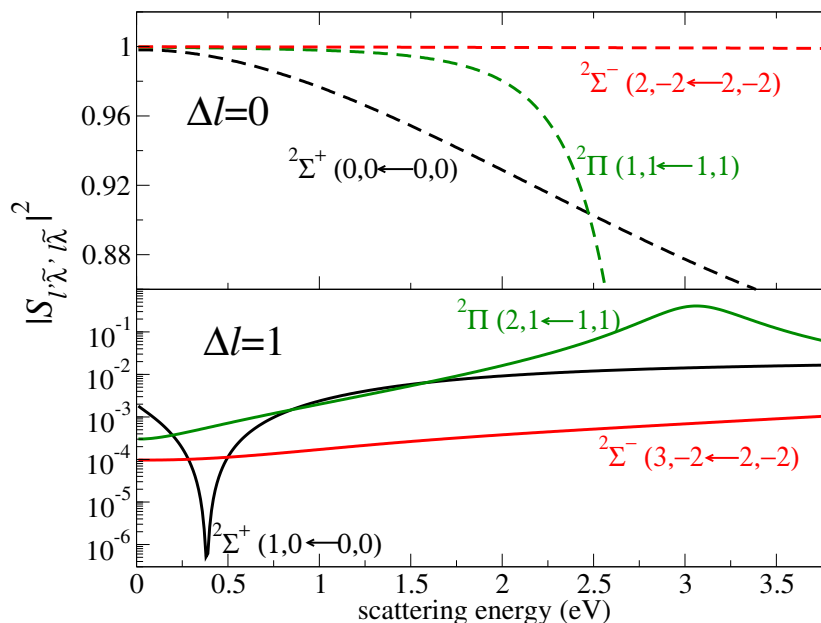


Figure 4.6: Largest S-matrix elements (absolute value squared,  $|S_{l\tilde{\lambda}, l\tilde{\lambda}}|^2$ ) computed at the  $\text{N}_2\text{O}$  equilibrium geometry as a function of the scattering energy. Upper panel shows the couplings between channels with  $\Delta l = 0$  in dashed curves. Bottom panel shows the coupling between channels with  $\Delta l = 1$  in solid curves.

therefore, it does not compromise the present theoretical approach. The vibrationally transformed S-matrix is calculated according to Equation (2.53), where the integration over vibrational coordinates is performed numerically using a Gaussian-Legendre quadrature (more details can be found in Appendix B) with 10 points.

### 4.3 Renner-Teller Coupling In $\text{N}_2\text{O}$ Vibrational Excitation By Electron

It is instructive to analyze the dependence of major coupling elements of the scattering matrix as a function of normal coordinates, especially for the bending mode. We start by introducing few general aspects of the Renner-Teller effect for linear molecules. The Renner-Teller coupling is,

of course, a particular type of the non-Born-Oppenheimer (non-adiabatic) coupling<sup>3</sup>. It induces a coupling between the vibrational and the electronic motions. Its effect on electron-molecule collisions was discussed in several previous studies [131, 136–140].

For N<sub>2</sub>O molecule, at its linear equilibrium configuration, the Renner-Teller coupling is zero. The main contribution to the VE cross section of the NO and NN stretching modes is thus due to variation of the diagonal elements of the scattering matrix with low  $l$ .

In contrast, for the bending mode, the major contribution is due to the  $q_1$ -dependence of non-diagonal elements between the  $^2\Sigma^+$  and  $^2\Pi$  states of the  $e^- + \text{N}_2\text{O}$  system near the linear geometry which is the Renner-Teller coupling. For a linear triatomic (and larger) molecule with a ground electronic state of  $^1\Sigma$  symmetry, the Renner-Teller effect couples  $\sigma$  and  $\pi$  partial waves<sup>4</sup> of the incident electron with vibrational bending motion of the target molecule.

Due to the symmetry of the bending mode, all matrix elements  $S_{l'\tilde{\lambda}', l\tilde{\lambda}}$  are symmetric or antisymmetric with respect to the change of the sign  $q_1 \rightarrow -q_1$  of the displacement along the bending mode. The elements, which are symmetric, such as diagonal elements and some non-diagonal, do not contribute to the vibrational excitation by one quantum of the bending mode. For an element  $S_{l'\tilde{\lambda}', l\tilde{\lambda}}$  to be antisymmetric with respect to the  $q_1 \rightarrow -q_1$  operation, one of  $\tilde{\lambda}'$  and  $\tilde{\lambda}$  should be negative with the other one to be positive or zero. In addition, there is a selection rule on the elements that do not vanish: For displacements along  $q_1$ , both spherical harmonics in  $S_{l'\tilde{\lambda}', l\tilde{\lambda}}$  should be of  $a'$  or  $a''$  irreducible representations<sup>5</sup> of the  $C_s$  symmetry group (of the bent molecule). Fig-

---

<sup>3</sup>The coupling between adiabatic electronic states computed in the Born-Oppenheimer approximation is often called non-Born-Oppenheimer coupling as well as non-adiabatic coupling. The two terms are almost equivalent but the term “non-adiabatic” is somewhat more general and may refer to the coupling between states different than electronic states obtained in the Born-Oppenheimer approximation.

<sup>4</sup>We denote both the  $\pi - \pi$  and  $\sigma - \pi$  couplings as Renner-Teller couplings, whereas in some other studies, only the former is denote by this term.

<sup>5</sup>The symmetric and antisymmetric with respect to reflection in a plane containing the molecular axis is denoted by single and double primes.

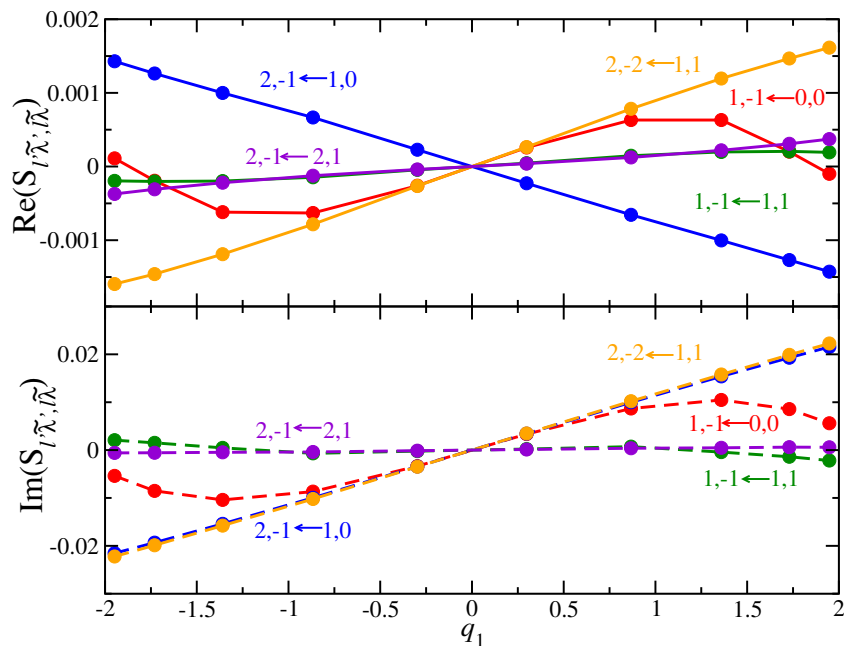


Figure 4.7: Largest fixed-nuclei S-matrix elements as a function of the bending coordinate  $q_1$ , computed for scattering energy 0.26 eV. The upper (lower) panel shows the real (imaginary) part of the S-matrix elements. Couplings  $l'\tilde{\lambda}' \leftarrow l\tilde{\lambda}$  between different partial waves, represented by real harmonics  $Y_{l,\tilde{\lambda}}$ , are labeled by curves of different colors.

Figure 4.7 shows largest (in magnitude) antisymmetric S-matrix elements as a function of the bending coordinate.

In Fig. 4.7, we see that the most of the elements are linear with the  $q_1$  coordinate with a notable exception of  $S_{1,-1,00}$ , which has a strong cubic dependence  $q_1^3$ . We attribute the significant cubic contribution to the coupling to the fact that the  $s\sigma$  partial wave penetrates closer to the  $N_2O$  core electrons such that the linear approximation for the coupling between the  $Y_{0,0}$  and  $Y_{1,-1}$  harmonics is not valid any more and higher terms, if a Taylor expansion is used to represent the coupling, are needed.

The linear dependence of the coupling between partial wave components in a linear molecule

for small displacements along the bending coordinate <sup>6</sup> is one of the main characteristics of the Renner-Teller effect (more details can be found in Equation (1) of Ref. [136]). The effect can not be easily observed in  $e^-$ -N<sub>2</sub>O scattering experiments, but it manifests itself in the bound states of  $e^-$ -N<sub>2</sub>O system: Due to the degeneracy of the <sup>2</sup>Π electronic state of the  $e^-$ -N<sub>2</sub>O complex and the degenerate bending mode of N<sub>2</sub>O, the relatively strong Renner-Teller coupling results in a bending configuration of the equilibrium geometry of the N<sub>2</sub>O<sup>-</sup> anion [141, 142].

#### 4.4 Cross Sections And Rate Coefficients

We calculated vibrational (de-)excitation cross sections for transitions between the ground and first excited vibrational states for each of the normal modes. Figure 4.8 displays the comparison of the theoretical  $1 \leftarrow 0$  VE cross sections with the available experimental data [121, 122, 129], mentioned in the introduction. All three experimental data do not resolve the  $\nu_2 = 1/\nu_1 = 2$  and  $\nu_3 = 1/\nu_2 = 2$  thresholds, i.e. the experimental cross section for the excitation of the NO mode ( $\nu_2 = 0 \rightarrow 1$ ) includes also a contribution for the transition  $\nu_1 = 0 \rightarrow 2$ , and the cross section for the excitation of the NN mode includes a contribution for the  $\nu_2 = 0 \rightarrow 2$  transition. But these additional contributions are expected to be significantly smaller due to the vibrational propensity rule: The transitions with a change of only one vibrational quantum are the largest. There is a significant disagreement between the experimental data, up to a factor of 20-50 for certain energies. On the other hand, the theoretical results also don't agree better with one or another experiments: For the NO stretching mode (panel b), the theory agrees better with the experiment by Hayashi [129]. For the bending mode (panel a), the theory agrees better with the two other experiments, although the agreement is quite poor. Finally, for the NN stretching mode (panel c), the theory

---

<sup>6</sup>With this choice of the quantization axis  $z$  (see Figure (4.2)), under the transformation  $q_1 \rightarrow -q_1$  the angle  $\phi$  changes sign and, correspondingly,  $\sin \phi \rightarrow -\sin \phi$  and  $\cos \phi \rightarrow \cos \phi$ . As a result, only the scattering matrix elements  $S_{l'\lambda', l\lambda}$ , in which the product of real spherical harmonics  $Y_{l'\lambda'} Y_{l\lambda}$  changes sign under  $q_1 \rightarrow -q_1$ , are linear with  $q_1$  in the lowest order.

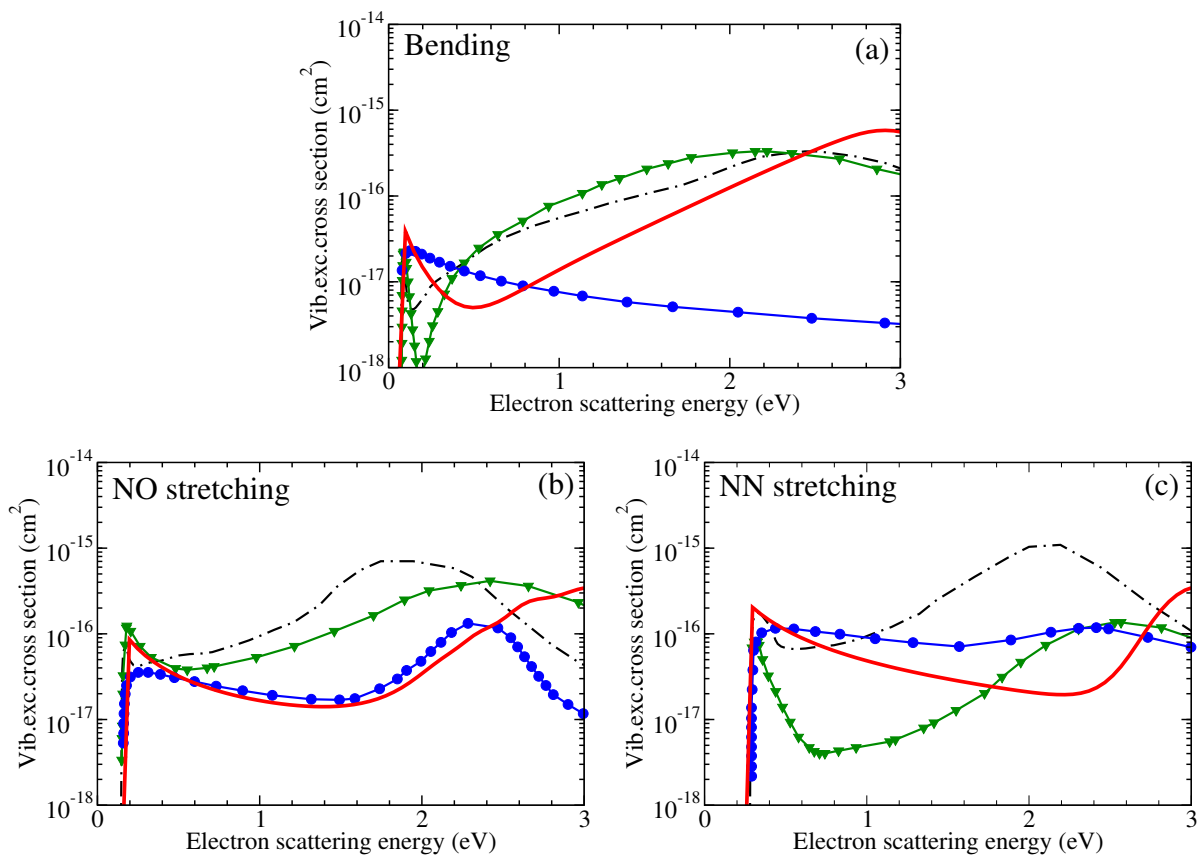


Figure 4.8: Comparison of the present theoretical results with available experimental cross sections for the vibrational  $v_i = 0 \rightarrow v_i' = 1$  excitation of the (a) bending, (b) NO stretching, and (c) NN stretching modes. The experimental results are taken from Hayashi [129, 130] (solid line with circles), Allan and Skalicky [121] (solid line with triangles), and Nakamura [122] (dashed-dotted line).

agrees better again with the data by Hayashi [129].

In a recent review article [130], the swarm data by Nakamura [122], shown by the dashed-dotted lines in the figure, were recommended as the most accurate one among the available experimental cross sections. However, it should be stressed that the recommended swarm data may not be very accurate because of an ambiguity in the interpretation of the swarm data [122] (see the discussion in Sections 3.3 and 3.5 of Ref. [130]). Therefore, the recommended experimental data should have

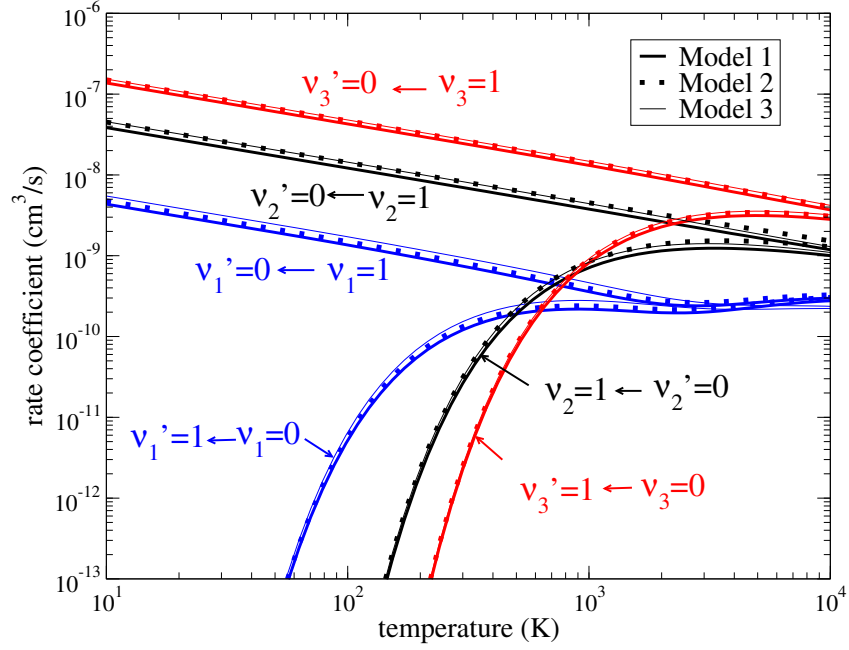


Figure 4.9: Thermally-averaged rate coefficients for (de-)excitation transitions between the ground and first excited vibrational states of the bending mode (blue curves), NO stretching mode (black curves) and NN stretching mode (red curves). Vibrational (de-)excitations are labeled by  $v_i' \leftarrow v_i$ . To give an idea of the uncertainty of the present results, we also plotted the results of calculations with Model 2 (dotted lines) and Model 3 (thin lines). The three calculations produce curves which are almost indistinguishable in the figure.

a relatively large uncertainty and could be improved in a future in a more accurate experiment.

The present theoretical cross sections are expected to be valid only for energies below the energy of the  $^2\Pi$  resonance mentioned above, i.e. below 2.3 eV.

Thermally averaged rate coefficients  $\alpha_{v_i'/v_i}(T)$  for vibrational excitation are obtained from the cross sections of Equation (2.55) using the standard formula (2.62). The computed rate coefficients are shown in Figure. 4.9 with different color. For a convenient use in plasma models, the computed coefficients were also fitted using the analytical formula (3.3), (3.4) and (3.5) employed in Chapter 3. The numerically fitted parameters for vibrational (de-)excitation are given in Table 4.2. When

Table 4.2: Parameters  $a_0$ ,  $a_1$  and  $a_2$  of the polynomial  $P_{v_i'v_i}^{fit}(x)$  in Equation (3.3) and (3.4) for transitions between the ground and first vibrational states in each normal mode. We specify the excitation threshold energies  $\Delta_{v_i'v_i}$  of Equation (3.5) in the second column. The threshold  $\Delta_{v_i'v_i} = 0$  for de-excitation process.

$1 \leftrightarrow 0$	$\Delta_{v_i'v_i}(\text{K})$	$a_0$	$a_1$	$a_2$
Bending	885	$1.37 \times 10^{-8}$	$-2.50 \times 10^{-11}$	$4.40 \times 10^{-12}$
NO stretching	1888	$1.22 \times 10^{-7}$	$6.60 \times 10^{-11}$	$-3.14 \times 10^{-11}$
NN stretching	3316	$4.34 \times 10^{-7}$	$7.42 \times 10^{-10}$	$-5.20 \times 10^{-10}$

the parameters given in the table are used in the fitting formulas of Equation (3.3) and (3.4) with temperature in kelvin, the obtained numerical values of rate coefficients will be in units of  $\text{cm}^3/\text{s}$ .

#### 4.5 Uncertainty Estimation

Similar to Section 3.4, we have performed a number of calculations to assess the uncertainty of the obtained theoretical results for  $\text{N}_2\text{O}$  molecule. There are two main sources of uncertainty in the present theoretical approach. The first one is the accuracy of the fixed-nuclei S-matrix elements computed for the polar molecule (with a small dipole moment) in the limited basis of spherical harmonics. It has been previously discussed in Section 3.4. The uncertainty associated with this approximation was estimated to be of the order of 6 % for  $\text{NO}_2$  in Chapter 3. It should not be larger for  $\text{N}_2\text{O}$  because it has a smaller dipole moment so that the couplings between partial waves induced by the permanent dipole moment of this molecule has a weaker effect on the final cross sections. Therefore, it is reasonable to assume that the corresponding uncertainty in the present case is below 6 %.

The second source of uncertainty is from the particular scattering model used in the calculation. The uncertainty can be assessed by performing a complete calculation with different parameters of

the model. With parameters discussed in Section 4.2, referred as Model 1, we obtained the results shown above. In the second calculation with Model 2, the CAS in the configuration calculation is the same as in Model 1 but a larger basis set cc-pVQZ was used. Finally, in Model 3 calculation the electronic basis set is kept cc-pVTZ, but the CAS is reduced compared to Model 1: 12 electrons were placed in frozen orbitals and remaining 10 electrons in the lowest orbitals were allowed to be freely distributed in the active space (see Table 4.3).

Table 4.3: The explicit characteristics of different Models used in uncertainty estimation for N<sub>2</sub>O. The second row is the basis sets. The numbers on the left side hand in parentheses indicate the number of active electrons. The numbers on the right side hand in parentheses indicate the number of active orbitals. For example, Model 1 means that the calculation is carried out using cc-pVTZ basis set and the CAS is 12 electrons are kept free in 10 active orbitals.

Model 1	Model 2	Model3
cc-pVTZ	cc-pvQZ	cc-pvTZ
CAS(12e,10o)	CAS(12e,10o)	CAS(10e, 8o)

The rate coefficients obtained in the three models are shown in Fig. 4.9. The difference in the rate coefficients produced in the three models is about 6 %. Consequently, the overall uncertainty of the present theoretical result is estimated to be below 12 %.

## 4.6 Conclusions

In this chapter, we computed cross sections for vibrational (de-)excitations of N<sub>2</sub>O by a low-energy electron using our developed model in Chapter 2: (1) the normal mode approximation describing the vibrational states of the target molecule, (2) the R-matrix method evaluating the fixed-nuclei electron-N<sub>2</sub>O scattering matrices, and (3) the vibrational frame transformation to evaluate amplitudes for vibrational transitions. In this approach, we neglected the rotational structure of each vibrational level, which corresponds to the situation where rotational structure is not resolved in

the initial and final states of the target molecule.

The computed results show a reasonable agreement with experimental data for NO and NN stretching modes. For the bending mode the agreement is rather poor at energies above 0.4 eV. It was found that the Renner-Teller coupling is responsible for the excitation of the bending mode, as it was expected from general theoretical considerations. We are quite confident about the present theoretical cross sections for the bending mode because the numerical calculations of fixed-nuclei scattering matrix fit well to the theory of Renner-Teller coupling.

It should be stressed here that the most reliable experimental cross section for the bending mode by Nakamura [122, 130] is obtained from swarm data and a direct measurement of differential cross section at a single scattering angle by Allan and Skalicky [121] and, therefore, may have a large uncertainty. This suggests that a better direct measurement of vibrational excitation in N<sub>2</sub>O, at least, for a few energies is needed.

## CHAPTER 5: DISSOCIATIVE ELECTRON ATTACHMENT OF NO<sub>2</sub>.

In low-energy electron–molecule collisions, dissociative electron attachment (DEA) is another dominant inelastic process which is in competition with rotational excitation and vibrational excitation that we studied in Chapter 3 and 4. As discussed in Chapter 1, DEA of NO<sub>2</sub> is important in depollution of combustion since it is an efficient process to remove the unwanted pollutant molecule by fragmenting it (the neutral toxic molecule) into neutral and charged fragments. However, the theoretical description of this process is still an extremely challenging task. In this chapter, we use a theoretical approach based on the Bardsley-O'Malley theory combined to the normal mode approximation of the target in order to estimate the DEA cross section for NO<sub>2</sub> with modest computational efforts. The obtained cross section agree with the available experimental results qualitatively. The quantitative discrepancy at the lowest resonance will be reserved for future study.

### 5.1 Introduction

Dissociative electron attachment of polyatomic molecule is represented symbolically by Equation (1.4) in Chapter 1. Generally, DEA can be described as a two-step process. Step one entails the resonant capture of a free electron by the molecule AB leading to the formation of a complex negative ion AB<sup>-\*</sup>. Step two concerns the decay of this negative ion via either electron ejection or dissociation into neutral and negative ion fragments. The latter channel is termed DEA. The products from DEA could take part very efficiently in various chemical processes leading to a wide variety of applications.

Due to the fact that the anionic product from DEA can be detected with standard mass spectrometer, DEA has been studied extensively in experiments. Experimental studies of DEA to molecules

from the size of diatomic molecules up to the size of bio-molecules were reviewed in Hotop *et al.* [143] and Fabrikant *et al.* [144]. Common experimental techniques for DEA are briefly mentioned here. Details can be found in Hotop *et al.* [143], Fabrikant *et al.* [144] and references therein. The electron beam used in DEA experiments is commonly produced from hot filament or photoionization. The beam is then crossed with molecular beam or stagnant gas target. The anionic products from DEA are then collected and analyzed in a time-of-flight mass spectrometer. Absolute DEA cross section can be obtained if the spectrometer is coupled with a trochoidal electron monochromator [145]. In addition, if the molecular beam has a well-defined profile, the absolute cross section can be obtained using the relative flow technique [146].

Apart from measuring the absolute cross section, it is of physical interest to study the velocity map of anionic products from DEA. From the velocity map, one can obtain the kinetic energy and angular distribution of the products, thereby understanding the dynamics of DEA. The velocity map imaging is achieved by the combination of time-of-flight spectrometer and position-sensitive detector [144], and its implementation to DEA experiments was first done by Krishnakumar and co-workers [147].

As mentioned in Chapter 1,  $\text{NO}_2$  is known as an industrial pollutants and controlling its emission is crucial for protection of the environment. Since DEA of  $\text{NO}_2$  is identified as one of the underlying mechanism for  $\text{NO}_2$  removing using non-equilibrium plasma, it has been studied experimentally by many groups. It was found that the DEA leads to the production of  $\text{O}^-$ ,  $\text{NO}^-$  and  $\text{O}_2^-$  and that the production peak of  $\text{NO}^-$  and  $\text{O}_2^-$  in comparison to  $\text{O}^-$  is more than two orders of magnitude smaller. Fox [88] reported  $\text{O}^-$  ion peaks at 1.9 eV, 3.0 eV and 8.75 eV. He assigned the 8.75 eV peak as due to impurities like NO or  $\text{H}_2\text{O}$ . Rallis and Goodings [148] reported  $\text{O}^-$  ion peaks at 3.0 eV and 8.1 eV. Abouaf and Fiquet-Fayard [149] reported that  $\text{O}^-$  produced with NO ( $X^2\Pi$ ) in the first peak is due to dissociation of  $\text{NO}^-$  in the  $^1\text{B}_1$  resonant state. Rangwala *et al.* [89] measured absolute cross section of  $\text{O}^-$  from DEA of  $\text{NO}_2$  and compared it with that of  $\text{O}_3$ . They observed

three main peaks at 1.4 eV, 3.1 eV and 8.3 eV in the  $O^-$  channel. The cross section at 1.4 eV peak is  $1.02 \times 10^{-17} \text{cm}^2$ . They noted that the peak positions in DEA cross sections of  $\text{NO}_2$  and  $\text{O}_3$  are similar. From these similarities they concluded that shape resonance mechanism is dominant at the first peak, however at higher energies core excited shape resonance and Feshbach resonance may contribute.

Even though a notable advancement in DEA experiments of  $\text{NO}_2$  has been obtained over the last decades, theoretical development for DEA of this molecule is sparse. In fact, even for diatomic molecules such as  $\text{Cl}_2$  and  $\text{O}_2$ , obtaining an accurate ab-initio DEA cross section is a very challenging task [150], not to mention the case of polyatomic molecules. The full-scale treatment of polyatomic molecules is unlikely in the near future due to the multi-dimensional nature of the problem. To the best of our knowledge, theoretical values are not available for  $\text{NO}_2$ . Thus, more effort is needed for searching a simplified approach to provide estimations on DEA cross sections for  $\text{NO}_2$  molecule.

Following the introduction, the theoretical approach used in the present DEA calculation will be presented in the next section. In Section 5.3, the obtained results are discussed. The concluding remarks are given in Section 5.4.

## 5.2 Resonance Calculation And Theory of Resonant Capture

Following the discussions of introduction, it was found that the DEA to  $\text{NO}_2$  gives  $O^-$  as the dominant ion with peaks at about 1.6 eV [89, 151]. The process will be studied here is therefore the following one, [90]



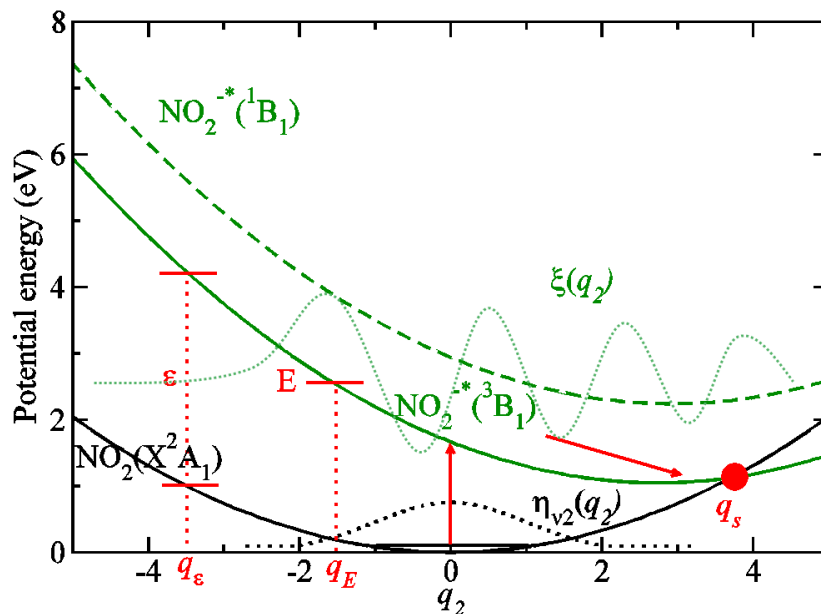


Figure 5.1: Schematics of DEA of  $\text{NO}_2(X^2A_1)$  depicting the break up channel  $\text{O}^-(^2P) + \text{NO}(X^2\Pi)$ . The graph shows the molecular potential energy curves as a function of the normal coordinate introduced in Section 2.1.3 (the reason why the abscissa is  $q_2$  will be discussed below). The neutral molecule captures an incoming electron with a certain kinetic energy (red arrow) and the system forms a temporary negative molecular ion  $\text{NO}_2^{-(^1,3B_1)}$  that eventually dissociates. It should be noted that the  $\text{NO}_2^{-(^3B_1)}$  and  $\text{NO}_2^{-(^1B_1)}$  states have the same dissociation limits.  $q_\epsilon$  denotes the Frank-Condon point.  $q_E$  denotes the classical turning point and  $q_s$  denotes the stabilization point.  $E$  is total energy and  $\epsilon$  is incident energy. The nuclei wave function  $\xi(q_2)$  and  $\eta_2(q_2)$  of  $\text{NO}_2^{-(^3B_1)}$  and  $\text{NO}_2(X^2A_1)$  are illustrated by the green and black dotted curves respectively.

This process can be illustrated schematically by the potential energy curves in Figure 5.1. The black solid curve and green solid (dashed) curve represent the potential energy curves of  $\text{NO}_2(X^2A_1)$  and  $\text{NO}_2^{-(^3B_1)}$  ( $\text{NO}_2^{-(^1B_1)}$ ) respectively. The black horizontal line indicates the ground vibrational state of  $\text{NO}_2(X^2A_1)$  where the process might start (the zero-point energy of  $\text{NO}_2(X^2A_1)$ ). The vertical red arrow indicates the electronic capture process, i.e., the electron attaching to  $\text{NO}_2(X^2A_1)$  at a specific incoming electron energy to form a temporary negative ion  $\text{NO}_2^{-(^3B_1)}$  (the nature of this intermediate state will be discussed below). The following red arrows indicate the dissociation path, when the temporary negative ion finds itself in a dissociative state leading

to the breakdown of the molecule. When the molecule has a normal coordinate larger than the position of the crossing point  $q_s$  between the potential of  $\text{NO}_2$  and  $\text{NO}_2^{-*}$ , autoionization (that is, re-emit the incoming electron) is no longer energetically possible. The dissociative state become bound and stable and will then continue to dissociate into the fragments  $\text{O}^{-}(^2P) + \text{NO}(X^2\Pi)$ . For this reason the crossover point  $q_s$  is often called the stabilization point.

The metastable intermediate state  $\text{NO}_2^{-*}(^1,^3B_1)$  mentioned above are called resonance states. The energy of the resonant anionic state relative to the neutral state of the molecule (the length of the vertical red arrow) therefore corresponds to the resonance energy. Generally, the DEA cross section  $\sigma_{DEA}$  can be written as the product of the cross section  $\sigma_c$  for the formation of this resonance state and the “survival probability,”  $S_f$ , i.e., the probability that the resonance  $\text{NO}_2^{-*}$  state will decay by dissociation rather than by autoionization, viz.,

$$\sigma_{DEA} = \sigma_c S_f. \quad (5.2)$$

The separation of the cross section into two independent factors describing the formation and dissociation of the intermediate resonance state as Equation (5.2) is extremely useful for a qualitative analysis of the DEA process [152–154].

In order to determine the capture cross section  $\sigma_c$  and survival probability  $S_f$  of Equation (5.2), the location (energy) and width of resonances are essential parameters. We employed the UK R-matrix code in Quantemol-N suite to compute these parameters. We first calculate the reaction matrix  $K$  mentioned in Section 2.2.2, then diagonalize it. Next, the eigenphase is extracted and summed over all different partial waves according to Equation (2.49). The derivative of the eigenphase sums is then fitted to the Breit-Wigner form

$$\frac{d\delta}{d\varepsilon} = \sum_i \frac{\Gamma_i/2}{(E - \Delta_i)^2 + (\Gamma_i/2)^2} \quad (5.3)$$

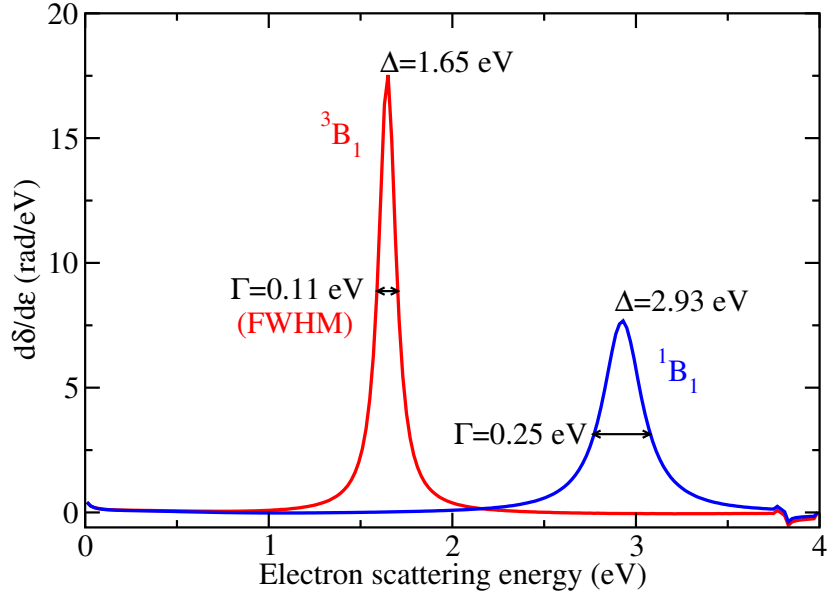
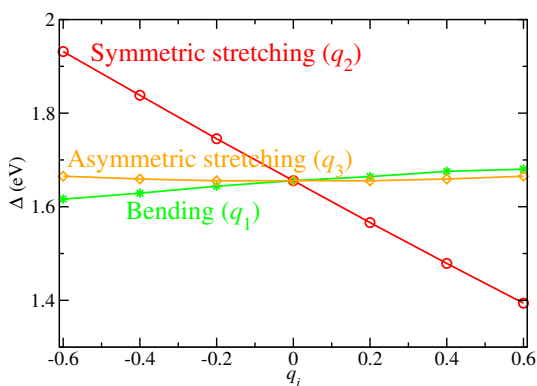


Figure 5.2: The derivative of the eigenphase sums (for  $\text{NO}_2 + e^-$  system) with respect to electron scattering energy for  ${}^3\text{B}_1$  (red curve) and  ${}^1\text{B}_1$  (blue curve) symmetries at equilibrium. The maximum of the derivative is used to obtain the width of the resonance according to Equation (5.4).

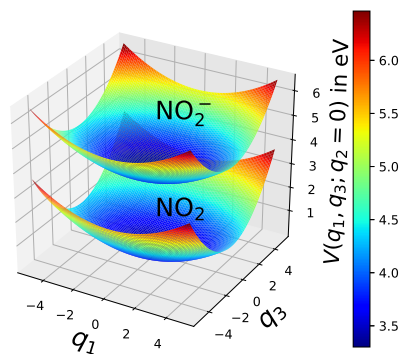
where  $\Delta_i$  and  $\Gamma_i$  are the  $i^{\text{th}}$  resonance energy and width. For isolated resonances, one can locate the resonance energies  $\Delta_i$  from the peaks of the derivative (see Figure 5.2) and calculate the widths by

$$\Gamma_i = 2 \left( \left. \frac{d\delta}{d\varepsilon} \right|_{\Delta_i} \right)^{-1}. \quad (5.4)$$

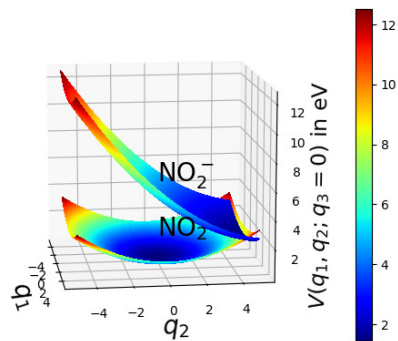
From Figure 5.2, it is clear to find that the resonance width is the full width at half maximum (FWHM) of the peak. At electron energy below 4 eV, and at equilibrium geometry, we found two shape resonances ( $\text{NO}_2 + e^-$  system) which usually appear as broad peaks in the eigenphase sum as a function of energy;  ${}^3\text{B}_1$  ( $\Delta = 1.65$  eV,  $\Gamma = 0.11$  eV) and  ${}^1\text{B}_1$  ( $\Delta = 2.93$  eV,  $\Gamma = 0.25$  eV). As mentioned in Equation (5.1), these two resonances can lead to dissociation to  $\text{O}^-({}^2P) + \text{NO}(\text{X}^2\Pi)$ .



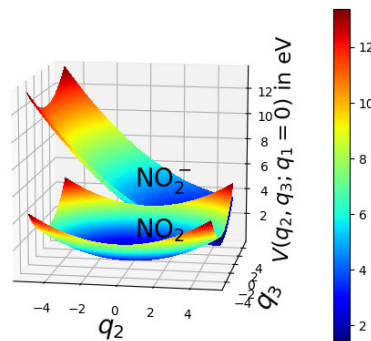
(a) The variation of resonance energies  $\Delta$  in (in eV) over  $q_1$  (green star),  $q_2$  (circles) and  $q_3$  (diamond) for  $\text{NO}_2^{-*}({}^3B_1)$ .



(b) The potential energy surface of  $\text{NO}_2(X^2A_1)$  and  $\text{NO}_2^{-*}({}^3B_1)$  over  $q_1$  and  $q_3$ .



(c) The potential energy surface of  $\text{NO}_2(X^2A_1)$  and  $\text{NO}_2^{-*}({}^3B_1)$  over  $q_1$  and  $q_2$ .



(d) The potential energy surface of  $\text{NO}_2(X^2A_1)$  and  $\text{NO}_2^{-*}({}^3B_1)$  over  $q_2$  and  $q_3$ .

Figure 5.3: The capture coordinate determination. Only  $q_2$  normal coordinate is relevant for electron capture process.

We then computed the resonance energy  $\Delta$  over different normal displacements to determine the capture coordinate, as shown in Figure 5.3 (a). We can find that for  $q_1$  (bending mode) and  $q_3$  (asymmetric stretching mode), resonance energy  $\Delta$  at negative and positive displacement are equal. It implies that the resonance energies depend at least quadratically on the normal displacement near the equilibrium, thus they are almost flat. The variation of  $\Delta$  over  $q_2$  is in a linear behavior, which

strongly suggest that only  $q_2$  coordinate is responsible for electron capture. For a more visually picture, we roughly plot the potential energy surface of  $\text{NO}_2(X^2A_1)$  and  $\text{NO}_2^{-*}(^3B_1)$  over each normal mode in Figure 5.3 (b), (c) and (d). According to Figure 5.1, we found that to obtain the potential energy of the resonant state, the neutral state has to be added to resonance energy. Since the resonance energies for  $q_1$  and  $q_3$  are almost constant, the potential energy surface of  $\text{NO}_2^{-*}(^3B_1)$  over  $q_1$  and  $q_3$  obtained by adding the constant energies to PES of  $\text{NO}_2(X^2A_1)$  is almost parallel to  $\text{NO}_2$  PES (see Figure 5.3 (b)). Clearly, the potential energy surfaces can only cross in the  $q_2$  dimension (see Figure 5.3 (b) and (d)) which gives the capture behavior as shown in Figure 5.1.

Since only one coordinate is responsible, no transformation is needed as in paper [29]<sup>1</sup>. The equation for the metastable nuclear wave function  $\xi(q_2)$  is then

$$\left[ \frac{-\hbar\omega_2}{2} \frac{d^2}{dq_2^2} + U_d(q_2) - \frac{i\Gamma(q_2)}{2} - E \right] \xi(q_2) = \sqrt{\frac{\Gamma(q_2)}{2\pi}} \eta_{v_2}(q_2), \quad (5.5)$$

$$U_d(q_2) = \frac{1}{2} \hbar\omega_2 q_2^2 + \Delta(q_2), \quad (5.6)$$

where  $U_d$  is defined as the potential energy curve of  $\text{NO}_2^{-*}$  (green solid curve in Figure 5.1) obtained by adding the resonance energy to the potential energy of  $\text{NO}_2$  in Equation (2.16) with dimensionless normal coordinate. The nuclear wave function of  $\text{NO}_2^{-*}(^3B_1)$  state,  $\xi(q_2)$ , as illustrated in Figure 5.1 with green dashed curve is an Airy function. It is largest near  $q_E$ , oscillates rapidly for  $q_2 > q_E$ , and decreases exponentially as  $q_2$  is decreased from  $q_E$ .  $q_E$  is the classical turning point, at which the potential energy of  $\text{NO}_2^{-*}(^3B_1)$  state,  $U_d$ , is equal to the total energy  $E$  ( $E$  is the sum of zero-point energy for frequency  $\omega_2$  and energy of the scattering electron  $\varepsilon$ , namely

---

<sup>1</sup>There are 6 different normal modes for the molecule investigated in Ref. [29], two normal coordinates are related to capture process. Thus a transformation is needed to obtain the capture coordinate.

$E = \frac{\hbar\omega_2}{2} + \varepsilon$ ).  $\eta_{v_2}$  is the initial wave function of  $\text{NO}_2$  nuclei. Since the width of the resonance  $\Gamma$  is in the order of 0.1 eV, autodetachment is non-negligible. Thus, the survival probability, against autodetachment has to be included in DEA calculation. Using the WKB approximation, the survival probabilities  $S_f$  can be explicitly written as [155–157]

$$S_f = \exp\left(-\frac{1}{\hbar} \int_{t_E}^{t_s} \Gamma(q) dt\right) = \exp\left(-\int_{q_E}^{q_s} \frac{\tilde{\Gamma}(q)}{\tilde{v}(q)} dq\right), \quad (5.7)$$

where  $\tilde{\Gamma} = \Gamma/(\hbar\omega_2)$ .  $\tilde{v}$  is the relative velocity of separation of the dissociating fragments  $\text{O}^-(^2P)$  and  $\text{NO}(X^2\Pi)$ ,  $\tilde{v}(q) = \sqrt{2[(E - U_d(q))/(\hbar\omega_2)]}$ . The integration is extended over the region between the Frank-Condon point  $q_E$  (the point at which the difference between the potential curve for  $\text{NO}_2^{-*}(^3B_1)$  and  $\text{NO}_2(X^2A_1)$  is equal to the incident energy  $\varepsilon$ ) and the stabilization point  $q_s$  (see Figure 5.1). The cross section for dissociative attachment, Equation (5.1), is then given by

$$\sigma_{DEA}(\varepsilon) = g \frac{2\pi^2}{k^2} \frac{\Gamma(q_E)}{|U'_d(q_E)|} |\eta_{v_2}(q_E)|^2 S_f, \quad (5.8)$$

where  $k$  is the wave number of incident electron and  $g$  is the spin statistical ratio ( $g = \frac{3}{4}$  for  $\text{NO}_2^{-*}(^3B_1)$ ,  $g = \frac{1}{4}$  for  $\text{NO}_2^{-*}(^1B_1)$ ). In order to evaluate this expression, one needs to know four things: the capture width  $\Gamma(q_E)$ , the exact positions of the classical turning point  $q_E$ , the slope of the repulsive potential energy curve  $U'_d$  and the initial nuclei wave function of target  $\eta_{v_2}(q_E)$ .

### 5.3 Results and Discussion

In order to obtain those parameters in Equation (5.8), we display the resonance energy  $\Delta$  of  $\text{NO}_2^{-*}(^1,^3B_1)$  and the potential energy curve  $U_n$  of  $\text{NO}_2(X^2A_1)$  along  $q_2$  obtained from Quantemol-

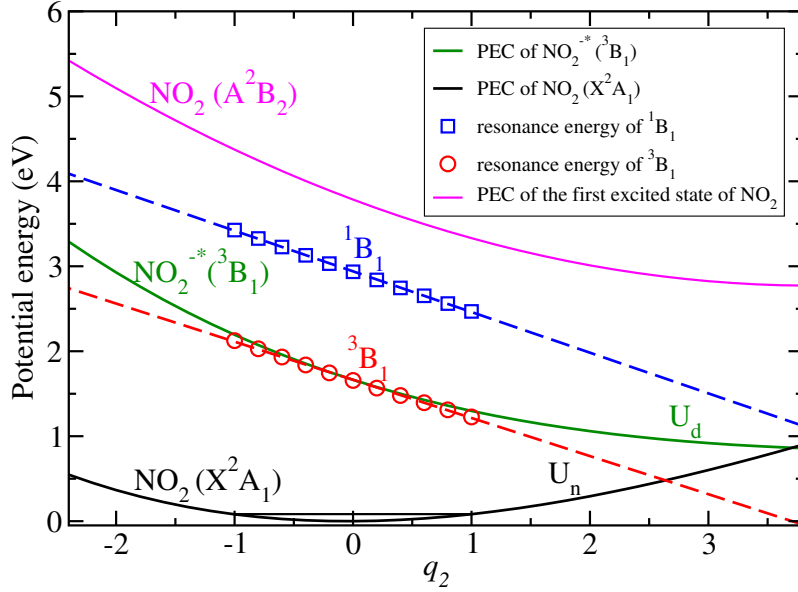


Figure 5.4: The anionic potential energy  $U_d$  (green curve), neutral potential energy  $U_n$  (black curve) and  ${}^3B_1$  resonance energy  $\Delta$  (circles) ( ${}^1B_1$  in squares) and its linear approximation (red straight line) along  $q_2$  for  $\text{NO}_2$  at  $q_1 = q_3 = 0$ . The first excited electronic state of  $\text{NO}_2$  (pink solid curve) obtained from Quantemol-N is also displayed in this figure. It indicates the DEA process is carried out below the first excited state of the target molecule.

N in Figure 5.4. The red line shows the first order approximation of  $\Delta(q_2)$ ,

$$\Delta(q_2) \approx \Delta(0) + \frac{d\Delta}{dq_2}(0)q_2. \quad (5.9)$$

The potential energy  $U_d$  of  $\text{NO}_2^{-*}({}^3B_1)$  is obtained by

$$U_d(q_2) = U_n(q_2) + \Delta(q_2). \quad (5.10)$$

The slope term in Equation (5.9) is therefore the derivative of  $U_d'$  at equilibrium. The  $\eta_{v_2}$  is the ground vibrational wave function of  $\text{NO}_2$  as expressed in Equation (2.20). The classical turning point  $q_E$  is obtained by solving the  $U_d(q_E) = E$ . The potential energy curve of  $\text{NO}_2$  and  $\text{NO}_2^{-}$  cross to each other around  $q_s = 3.7$ . The stabilization point is far from the Frank-Condon region.

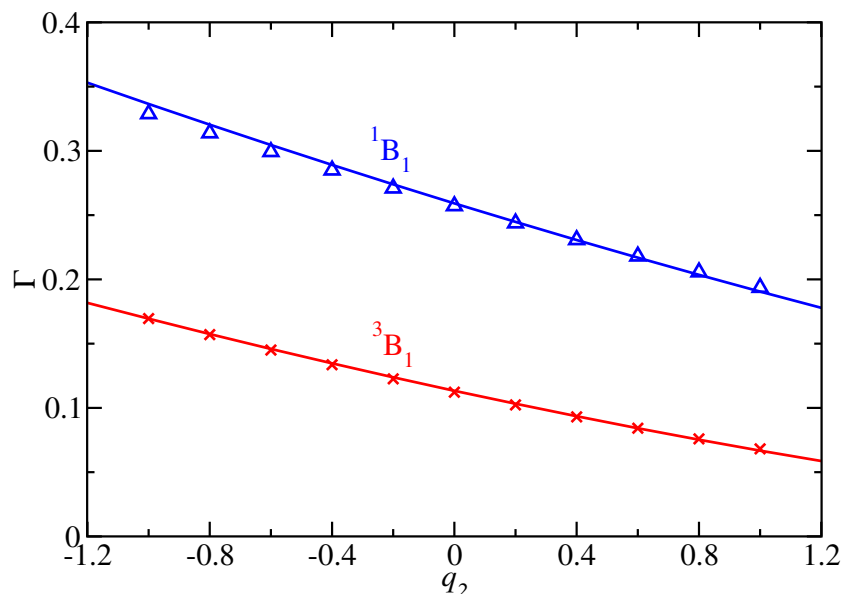


Figure 5.5: The width of the  $^3B_1$  (red crosses) and  $^1B_1$  (blue triangles) resonances against its position with different values of  $q_2$  for  $\text{NO}_2$  at  $q_1 = q_3 = 0$ . Straight lines are the corresponding fitting part using Equation (5.9)

However, the classical turning point  $q_E$  starting at -1.5 is within the range of the nuclear vibrations in the initial neutral state. The capture process can clearly occur in this molecule in a well-defined region of normal coordinates, thereby our approach is justified. The formation of  $\text{NO}_2^{-*}$  is most likely to occur when the normal coordinate is close to the Frank-Condon point obtained by solving  $\Delta(q_\epsilon) = \epsilon$ . At this point electron capture can occur without any simultaneous transfer of energy into nuclear motion. We therefore show the effective width against its position with different values of  $q_2$  in Figure 5.5. As discussed in paper [29], the effective width is related to the resonance energy  $\Delta(q_\epsilon)$  which can be fitted by electron energy  $\epsilon$  to enforce the threshold behavior. In the present case, the effective width can be fitted as

$$\Gamma(q_\epsilon) = \alpha \left[ \Delta(0) + \frac{d\Delta}{dq_\epsilon}(0)q_\epsilon \right]^\beta, \quad (5.11)$$

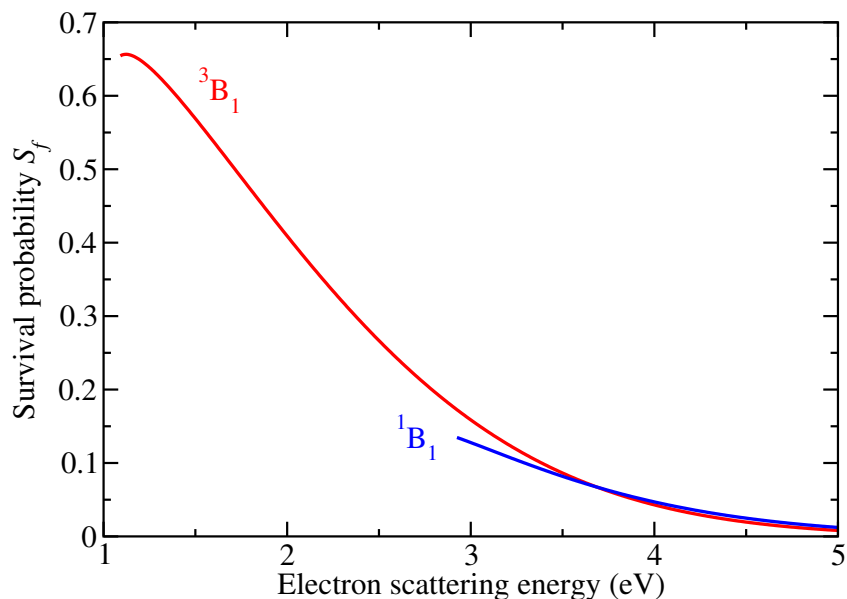


Figure 5.6: The calculated survival probability of the  ${}^3B_1$  (red curve) and  ${}^1B_1$  (solid curve) resonances with respect to electron scattering energy.

since the electron energy is set to equal the resonance energy in our approach.  $\alpha$  and  $\beta$  are fitting coefficient. As we offset the resonance energy, the effective width will be zero at the crossing point between the anionic and neutral potential.

With all the necessary quantities in hand, we can obtain the survival probabilities  $S_f$  as plotted in Figure 5.6 and the DEA cross section of Equation (5.8) is shown in Figure 5.7. The first peak value of the cross section in the present study is  $2.655 \times 10^{-16} \text{ cm}^2$  at 1.49 eV. It is about 26 times of magnitude larger than the cross section measured by Rangwala *et al.* [89]. The deviation could be explained by the fact that the existence of potential barrier in the dissociation pathway  $O^- + NO$ , such that there is reflection of the outgoing flux from the barrier causing significant increase of the cross section. If we can compute the potential energy curve of  $NO_2^-$  and then estimate the tunneling probability, the DEA cross section results may be improved. However, the peak location is only about 3.5% different from the experiment by Rangwala *et al.* [89], which

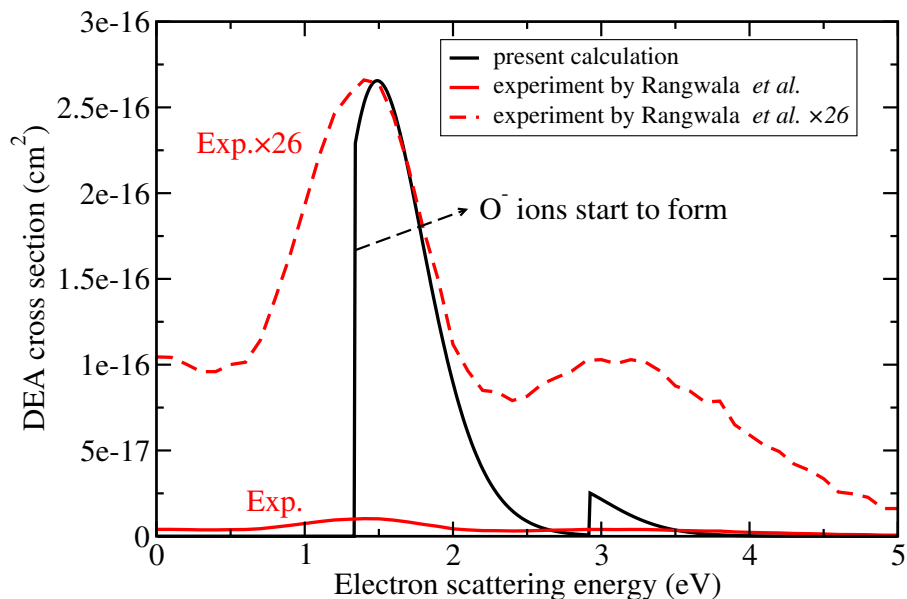


Figure 5.7: Comparison between the experimental DEA cross section for  $\text{NO}_2$  by Rangwala *et al.* (red solid curve) and the present theoretical results (black solid curve).

is within their uncertainty. In addition, an onset of the calculated cross section can be seen from Figure 5.7 which represents the threshold energy at which  $\text{O}^-$  ions start to form. The  $\text{O}^-$  cannot be formed at 0 eV as DEA of  $\text{NO}_2$  is an endothermic process, such that there is an activation energy. The threshold energy in experiment is 1.65 eV. It is determined by the ON-O bond dissociation energy ( $D_{\text{ON-O}} = 3.11$  eV) and O electron affinity ( $\text{EA}_{\text{O}} = 1.46$  eV). The electron affinity of an atom or molecules is the energy released when the extra electron is detached from a singly charged negative ion. The calculated threshold energy is 1.42 eV ( $E_{th} = 1.65 - \frac{\hbar\omega_z}{2}$ ) which agree with the experimental data well. The threshold energy of cross section by Rangwala *et al.* [89] is much lower than 1.65 eV due to the finite energy resolution of the electron beam and limitation in calculating the average initial kinetic energy from FWHM of the peak with fairly Gaussian shape [147]. The position of the second peak at 2.9 eV observed by Rangwala *et al.* [89] and Nandi *et al.* [147] at 3.0 eV was also well reproduced in the present study. But the magnitude of the cross section is still 6 times larger than the experiments by Rangwala *et al.* [89].

#### 5.4 Conclusion And Further Works

To summarize, we calculated the DEA cross section of  $\text{NO}_2$  using an *ab-initio* method based on the Bardsley-O'Malley theory [152, 154, 155] proposed for diatomic molecules and generalized to polyatomic molecules by Chi Hong Yuen *et al.* [29]. Survival probability can be implemented to compute DEA cross section in the present model. The peak location and threshold energy have a good agreement with experiments which implying the simplified approach capture partial physics of DEA. It thus encourages study of other similar systems such as  $\text{SO}_2$  and  $\text{N}_2\text{O}$  using the same approach. But more information is needed for the potential energy surface of  $\text{NO}_2^-$  to enhance the DEA cross section. Potential energy surface calculation is computationally expensive and will be reserved for future study. Despite many works will be required to improve the present model, our approach can still provide an idea of the DEA cross section when other more accurate approach are computationally expensive or not available.

## CHAPTER 6: CONCLUSION AND PERSPECTIVES

In this thesis, we present theoretical studies of electron-induced vibrational excitation of  $\text{NO}_2$  (Chapter 3) and  $\text{N}_2\text{O}$  (Chapter 4). It is the most important process for nitrogen oxides containing plasma kinetic modeling. The dissociative electron attachment which is the competitive process of vibrational excitation is also investigated in this thesis for  $\text{NO}_2$  molecule (Chapter 5). The purpose of this work is to develop a theoretical formulation for this process for an arbitrary polyatomic molecule, and to understand the mechanism of depollution procedure using non-equilibrium plasma technology, because DEA is considered to be a major route to  $\text{NO}_2$  pollutant molecular break-up in cool plasma. A brief summary of the results chapter by chapter is given below followed by conclusions for the individual quantities calculated. Finally a discussion of future work is given to conclude.

Cross sections for the vibrational excitation of  $\text{NO}_2$  between the lowest vibrational states were calculated for all the normal modes (Section 3.2 and 3.3). The theoretical approach applied for cross section calculation can be summarized as following. We start by characterizing the molecular target (Section 2.1) according to its important physical properties such as equilibrium geometry, permanent dipole moment and vibrational frequencies using the MOLPRO procedure. The corresponding outputs will be used in the scattering part. We performed an R-matrix theory calculation (Section 2.2.2) to obtain the scattering matrices for different molecular geometries along the vibrational normal mode coordinates. We then transform the fixed-nuclei S-matrix into the basis of vibrational states of the target molecule (Section 2.2.3). Finally, we compute the vibrational (de-) excitation cross sections from the transformed scattering matrix. The VE cross sections for  $\text{NO}_2$  was reported for the first time. Therefore, the uncertainty estimation was performed to validate the present theoretical approach. The uncertainty may arise from varying parameters of the computational model such as a chosen Gaussian basis set, the size of the R-matrix box, and other parameters

of the model. Uncertainties for some intermediate quantities were shown and discussed to give an idea about the convergence of our results (Section 3.4). Thermally averaged rate coefficients are computed for temperatures in the 10-10000 K range.

Cross sections for the vibrational excitation of  $\text{N}_2\text{O}$  between the lowest vibrational states were calculated for all the normal modes (Section 4.2 and 4.3). The calculation was carried out using the similar approach applied to  $\text{NO}_2$ . It was found that the non-adiabatic Renner-Teller effect, which couples partial waves of the incident electron with degenerate bending vibrations of  $\text{N}_2\text{O}$ , is responsible for the excitation of the bending mode. The obtained theoretical results for NO stretching and NN stretching mode agree reasonably well with available experimental data at low energies. Thermally averaged rate coefficients were also computed for temperatures in the 10-10000 K range.

For  $\text{NO}_2$  and  $\text{N}_2\text{O}$ , the obtained cross section and rate coefficient of vibrational excitation should be viewed as averaged over initial rotational states and summed over final rotational states of the corresponding initial and final vibrational levels. The obtained thermally-averaged rate coefficients are relevant for the kinetic modeling of molecule based cold non-equilibrium plasma, in the context of a complete lack of other theoretical or experimental data on these processes for these molecules, and are ready to be used in the modeling of plasma for depollution processes. The thermally-averaged rate coefficients were all thus fitted by analytical form for convenient use in plasma modeling.

Besides the vibrational excitation, there is a probability for DEA process (Chapter 5) occurring at collision energies of the incident electron below the first excited state of the target molecule. This process was therefore a necessary part in the present thesis to understand more of the dynamic within the  $\text{NO}_2$  containing plasma. We started from the method based on the Bardsley-O'Malley theory developed for diatomic molecules and generalized to complex polyatomic molecules by Chi

Hong Yuen *et al.* The resonance parameters obtained in R-matrix calculation for VE of  $\text{NO}_2$  was directly set as the input for DEA cross section calculation. Our cross sections were compared with experimentally measured of this reaction. However, the magnitude of cross section calculated in this thesis is 26 times larger than the experimental result. The reason may attributed to the existence of the potential barrier on the potential energy surface of the  $\text{NO}_2^{-*}$  after the crossing point. If we can determine the location and height of the potential barrier, and compute the tunneling probability according it, there is a chance to improve the present DEA result.

Therefore, computing the potential energy surface of  $\text{NO}_2$  and  $\text{NO}_2^-$  will be the future work to try to improve our DEA results. In addition, extending the approach applied in vibrational excitation to vibronic excitation <sup>1</sup> for  $\text{N}_2\text{O}$  is also a meaningful proposal for the future work since the corresponding experiment results are available and this process is also necessary in N- and O-containing plasma modeling. Electronic structure calculation for the excited state should be the first step. Scattering calculation of the excited state along normal coordinates will be a challenging work in vibronic project. A theoretical approach combined with vibronic frame transformation used in Ref. [158] can be applied to the vibronic excitation of  $\text{N}_2\text{O}$ .

---

<sup>1</sup>The excitations between vibrational levels of different electronic states.

## APPENDIX A: Quantemol-N

Quantemol-N is menu driven by a series of panels:

### **Panel 1: Molecule Definition**

In this panel, we can write the target molecular formula in accordance with the standard way or select the corresponding elements from the periodic table.

### **Panel 2: Set Isotope**

### **Panel 3: Coordinate Entry**

This panel deals with the target geometry. The Cartesian position vectors of the constituent atoms are entered into the table in Angstroms. Rotation operation on the right of the panel can be used to adjust the molecular point group. Note that the center-of-mass frame are adopted in the R-matrix calculation. Namely, the origin of the input coordinate of the target molecular ion should locate at the center of mass of the target. To make sure that the origin is put at the center of mass, we just need to click the button "move to the center of mass" in this panel. While for MOLPRO, it doesn't matter since the origin will be automatically moved to the center of mass. The obtained potential energies are the same and only behavior as a function of normal coordinates.

### **Panel 4: Symmetry Definition**

By clicking on the point group menu in panel 3, the point group symmetry operations are imposed on the molecule. The symmetrically equivalent atoms must be selected also in order to proceed.

### **Panel 5: Electronic structure**

We can supply the ground state configuration of the target molecule in this panel.

### **Panel 6: Target Model**

This panel deals with the assumptions of the quantum chemistry method and basis set used to represent the target wavefunctions. The basis set is selected usually from the library supplied with the software. Another option is available to import other basis sets in supermolecule format from

EMSL [159]. The number of atomic symmetries in the bottom of this panel means that how many kinds of GTO functions are used in the calculation. Please note that the Quantemol-N module only interprets up to g functions.

### **Panel 7: Scattering Parameters**

This panel deals with the outer region calculation. The number of target states to be included in the calculation can be altered here. Choosing the total number states as zero here means that all the electronic states below the cut-off energy will be taken into account. The ‘CAS Virtuals’ option requires us to select additional orbitals to construct the complete active space (not the number of all the active orbitals). The R-matrix interaction radius, default  $10 a_0$ , and the energy grid, default setting 0.1 eV to 10 eV in steps of 0.02 eV, all of which may be set here.

### **Panel 8: Additional Functionality**

This panel allows us to decide whether to run additional modules to give extra data such as DEA cross sections and high-energy cross sections.

### **Panel 9: Advanced Settings**

Virtual orbitals and frozen orbitals (occupied-open) can be set at this panel. In addition, the HFSCF and MCSCF orbitals generated by MOLPRO can also be imported in the R-matrix calculation by clicking the related options on the right of this panel. Options ‘Open Orbs’ and ‘Valence Orbitals’ respectively refer to the open orbitals and CAS virtuals defined before. ‘States’ means the state average.

### **Panel 10: Review Calculation**

The last panel gives a summary of the previously set parameters which must be saved in order to proceed with the R-matrix calculation

Quantemol-N generates vertical excitation energies, graphs of eigenphase sums, inelastic cross sections, BEB ionization cross sections and rate coefficients. Resonances are automatically fitted to yield their parameters. The data are saved to simple text files to facilitate further analysis.

### **Common error exits in Quantemol-N**

*Error 38* means that there is not enough space in the hard disk. It can be resolved by deleting the 'qntmp' folder.

*Error 64* means that some problems occurred while rearranging the data to be displayed on the computation end panel. It doesn't matter if this error occurs because all the data will be used for further analyzing has already been saved in the 'results' and 'matrices' folders.

*Error174* means that the chosen CAS is too big.

*Error 62* is coming when there are excited states near to the energy of the scattering electron. In ions in particular, there are low lying excited states, and when you get near to a threshold of an excited state there can be an infinite number of resonances which leads to instabilities in the R-matrix codes. This problem can be solved by using the small electron scattering grid such as 0.001 eV and decreasing the finishing energy to avoid the resonances that are currently causing the instabilities. Another suggestion is to increase the propagation distance such as  $500 a_0$  - something that has to be done manually in the input files.

## APPENDIX B: Gauss–Legendre quadrature

Gauss-Legendre quadrature technique is a numerical integration technique in which the definite integral of a function can be stated as a weighted sum of function values at specified points within the domain of integration:

$$\int_{-1}^1 f(q) dq = \sum_{i=1}^n w_i f(q_i). \quad (\text{B.1})$$

Here,  $q_i$  is the Gauss node (the  $i^{\text{th}}$  root of Legendre polynomials  $P_n$ <sup>1</sup>) and its weight  $w_i$  is given by

$$w_i = \frac{2(1 - q_i^2)}{[nP_{n-1}(q_i)]^2}, \quad (\text{B.2})$$

where the Legendre polynomials can be defined via the recursive relation

$$P_{n+1}(q) = \frac{2n+1}{n+1}qP_n(q) - \frac{n}{n+1}P_{n-1}(q). \quad (\text{B.3})$$

Fortunately, the roots of the Legendre polynomials and their corresponding weights have been extensively tabulated, so we can simply use these tables (such as Table B.1) without redoing the calculations. The only issue to be careful about is that the tabulated values were computed by taking  $[-1, 1]$  as the integration interval, whereas in any given problem the integration interval may not be  $[-1, 1]$ . Therefore we need to transform the tabulated values to analogous values on a general interval  $[a, b]$ . This is done through the following change of variable:

$$-1 \leq \tilde{q} < 1 \leftrightarrow a < q \leq b, \quad (\text{B.4})$$

---

<sup>1</sup>The first few are  $P_0(q) = 1$ ,  $P_1(q) = q$ ,  $P_2(q) = \frac{3}{2}(q^2 - \frac{1}{3})$ ,  $P_3(q) = \frac{5}{2}(q^3 - \frac{3}{5}q)$  and  $P_4(q) = \frac{1}{8}(35q^4 - 30q^2 + 3)$ .

if

$$\frac{\tilde{q} - (-1)}{1 - (-1)} = \frac{q - a}{b - a}, \quad (\text{B.5})$$

so that

$$q = \frac{b-a}{2}\tilde{q} + \frac{a+b}{2}, \quad (\text{B.6})$$

$$\begin{aligned} \int_a^b f(q) dq &= \int_{-1}^1 f\left(\frac{b-a}{2}\tilde{q} + \frac{a+b}{2}\right) \frac{dq}{d\tilde{q}} d\tilde{q} \\ &= \int_{-1}^1 f\left(\frac{b-a}{2}\tilde{q} + \frac{a+b}{2}\right) \frac{b-a}{2} d\tilde{q} \\ &= \frac{b-a}{2} \int_{-1}^1 f\left(\frac{b-a}{2}\tilde{q} + \frac{a+b}{2}\right) d\tilde{q} \\ &\approx \frac{b-a}{2} \sum_{i=1}^n w_i f\left(\frac{b-a}{2}\tilde{q}_i + \frac{a+b}{2}\right) \end{aligned} \quad (\text{B.7})$$

If we define  $h = \frac{b-a}{2}$  (the length of the interval) and  $c = \frac{a+b}{2}$  (the midpoint of the interval), then the roots  $\tilde{q}_i$  in  $[-1, 1]$  are transformed to the nodes  $q_i$  in  $[a, b]$  via  $q_i = \frac{h}{\tilde{q}_i} + c$ , and the quadrature formula for approximating  $\int_a^b f(q) dq$  will be  $\frac{h}{2}$  times the formula for approximating the equivalent integral over  $[-1, 1]$ . The quadrature rules defined above, using the roots of Legendre polynomials as their nodes, are called Gauss–Legendre rules which is used in the  $S_{\nu_i l' \lambda', \nu_i l \lambda}$  of Equation (2.53) calculation.

Table B.1: Gauss–Legendre nodes and weights

number of points, $i$	nodes, $q_i$	weights, $w_i$
1	0	2
2	$-\frac{1}{\sqrt{3}}$	1
	$+\frac{1}{\sqrt{3}}$	1
3	$-\sqrt{\frac{3}{5}}$	$\frac{5}{9}$
	0	$\frac{8}{9}$
	$+\sqrt{\frac{3}{5}}$	$\frac{5}{9}$
4	$-\sqrt{\frac{15+2\sqrt{30}}{35}}$	$\frac{18-\sqrt{30}}{36}$
	$-\sqrt{\frac{15-2\sqrt{30}}{35}}$	$\frac{18+\sqrt{30}}{36}$
	$+\sqrt{\frac{15-2\sqrt{30}}{35}}$	$\frac{18+\sqrt{30}}{36}$
	$+\sqrt{\frac{15+2\sqrt{30}}{35}}$	$\frac{18-\sqrt{30}}{36}$
$\vdots$	$\vdots$	$\vdots$

## APPENDIX C: The simple VE formulation

Starting from the harmonic potential

$$V(x) = \frac{1}{2}m\omega^2x^2, \quad (\text{C.1})$$

and introducing the dimensionless normal coordinate  $q = x\sqrt{\frac{m\omega}{\hbar}}$ , Eq.(C.1) becomes

$$V(q) = \frac{\hbar\omega}{2}q^2, \quad (\text{C.2})$$

where  $m$  and  $\omega$  stand for the mass and angular frequency of the particle, respectively. Expanding the S-matrix of 2sd-order in the normal mode coordinate  $q_i$  (of mode  $i$ )

$$S_{l'\lambda',l\lambda}(\mathbf{q}) = S_{l'\lambda',l\lambda}(\mathbf{q}_{eq}) + \sum_i \left. \frac{\partial S_{l'\lambda',l\lambda}}{\partial q_i} \right|_{q_{eq}} q_i + \frac{1}{2} \sum_i \left. \frac{\partial^2 S_{l'\lambda',l\lambda}}{\partial q_i^2} \right|_{q_{eq}} q_i^2 + \mathcal{O}(q_i^3) \quad (\text{C.3})$$

The vibrational frame transformation consists on evaluating the matrix elements

$$\langle v | S_{l'\lambda',l\lambda}(\mathbf{q}) | v \rangle \quad (\text{C.4})$$

where  $q_i = \frac{1}{\sqrt{2}}(\hat{a}_i + \hat{a}_i^\dagger)$  upon introducing the operator of annihilation  $a_i$  and its adjoint, the creation operator,  $a_i^\dagger$  that act on any ket  $|v_i\rangle$  as

$$\hat{a}_i |v_i\rangle = \sqrt{v_i} |v_i - 1\rangle \quad \text{and} \quad \hat{a}_i^\dagger |v_i\rangle = \sqrt{v_i + 1} |v_i + 1\rangle. \quad (\text{C.5})$$

Plugging Eq.(C.3) into Eq.(C.4) yields

$$\langle v | S_{l'\lambda',l\lambda}(\mathbf{q}) | v' \rangle = \langle v | S_{l'\lambda',l\lambda}(\mathbf{q}_{eq}) | v' \rangle + \sum_i \left. \frac{\partial S_{l'\lambda',l\lambda}}{\partial q_i} \right|_{q_{eq}} \langle v_i | q_i | v'_i \rangle + \frac{1}{2} \sum_i \left. \frac{\partial^2 S_{l'\lambda',l\lambda}}{\partial q_i^2} \right|_{q_{eq}} \langle v_i | q_i^2 | v'_i \rangle$$

Lets evaluate each term above using Eqs.(C.5) :

$$\langle v | S_{l'\lambda',l\lambda}(\mathbf{q}_{eq}) | v' \rangle = S_{l'\lambda',l\lambda}(\mathbf{q}_{eq}) \langle v | v' \rangle = S_{l'\lambda',l\lambda}(\mathbf{q}_{eq}) \delta_{vv'} \quad (\text{C.6})$$

$$\begin{aligned} \sum_i \left. \frac{\partial S_{l'\lambda',l\lambda}}{\partial q_i} \right|_{q_{eq}} \langle v_i | q_i | v'_i \rangle &= \frac{1}{\sqrt{2}} \sum_i \left. \frac{\partial S_{l'\lambda',l\lambda}}{\partial q_i} \right|_{q_{eq}} \langle v_i | \hat{a}_i + \hat{a}_i^\dagger | v'_i \rangle \\ &= \frac{1}{\sqrt{2}} \sum_i \left. \frac{\partial S_{l'\lambda',l\lambda}}{\partial q_i} \right|_{q_{eq}} \langle v_i | \hat{a}_i | v'_i \rangle + \frac{1}{\sqrt{2}} \sum_i \left. \frac{\partial S_{l'\lambda',l\lambda}}{\partial q_i} \right|_{q_{eq}} \langle v_i | \hat{a}_i^\dagger | v'_i \rangle \\ &= \frac{1}{\sqrt{2}} \sum_i \left. \frac{\partial S_{l'\lambda',l\lambda}}{\partial q_i} \right|_{q_{eq}} \sqrt{v'_i} \langle v_i | v'_i - 1 \rangle + \frac{1}{\sqrt{2}} \sum_i \left. \frac{\partial S_{l'\lambda',l\lambda}}{\partial q_i} \right|_{q_{eq}} \sqrt{v'_i + 1} \langle v_i | v'_i + 1 \rangle \\ &= \frac{1}{\sqrt{2}} \sum_i \left. \frac{\partial S_{l'\lambda',l\lambda}}{\partial q_i} \right|_{q_{eq}} \left( \sqrt{v'_i} \delta_{v_i v'_i - 1} + \sqrt{v'_i + 1} \delta_{v_i v'_i + 1} \right) \end{aligned} \quad (\text{C.7})$$

and

$$\begin{aligned} \frac{1}{2} \sum_i \left. \frac{\partial^2 S_{l'\lambda',l\lambda}}{\partial q_i^2} \right|_{q_{eq}} \langle v_i | q_i^2 | v'_i \rangle &= \frac{1}{2(\sqrt{2})^2} \sum_i \left. \frac{\partial^2 S_{l'\lambda',l\lambda}}{\partial q_i^2} \right|_{q_{eq}} \langle v_i | (\hat{a}_i + \hat{a}_i^\dagger)^2 | v'_i \rangle \\ &= \frac{1}{4} \sum_i \left. \frac{\partial^2 S_{l'\lambda',l\lambda}}{\partial q_i^2} \right|_{q_{eq}} \left( \langle v_i | \hat{a}_i^2 | v'_i \rangle + \langle v_i | \hat{a}_i^{\dagger 2} | v'_i \rangle + \langle v_i | 2\hat{N}_i + \hat{1} | v'_i \rangle \right) \\ &= \frac{1}{4} \sum_i \left. \frac{\partial^2 S_{l'\lambda',l\lambda}}{\partial q_i^2} \right|_{q_{eq}} \left( \sqrt{v'_i(v'_i - 1)} \langle v_i | v'_i - 2 \rangle + \sqrt{(v'_i + 1)(v'_i + 2)} \langle v_i | v'_i + 2 \rangle + (2v'_i + 1) \langle v_i | v'_i \rangle \right) \\ &= \frac{1}{4} \sum_i \left. \frac{\partial^2 S_{l'\lambda',l\lambda}}{\partial q_i^2} \right|_{q_{eq}} \left( \sqrt{v'_i(v'_i - 1)} \delta_{v_i v'_i - 2} + \sqrt{(v'_i + 1)(v'_i + 2)} \delta_{v_i v'_i + 2} + (2v'_i + 1) \delta_{v_i v'_i} \right) \end{aligned} \quad (\text{C.8})$$

Assuming that the molecule is in its vibrational ground state ( $\forall i, v'_i = 0$ ), in the first order, the electron can be captured only in the first excited vibrational state of each mode. Hence, Eqs.(C.6)

and (C.8) cancel out and Eq.(C.7) gives

$$\sum_i \frac{\partial S_{l'\lambda',l\lambda}}{\partial q_i} \Big|_{q_{eq}} \langle v_i | q_i | v_i' \rangle = \frac{1}{\sqrt{2}} \sum_i \frac{\partial S_{l'\lambda',l\lambda}}{\partial q_i} \Big|_{q_{eq}} \times 1 \quad (\text{C.9})$$

Thus, the VE cross section for mode  $i$  can be expressed as

$$\begin{aligned} \sigma_{v_i' v_i} &= \frac{\pi \hbar^2}{2mE} \sum_{l'\lambda',l\lambda} \left| \frac{\partial S_{l'\lambda',l\lambda}}{\partial q_i} \Big|_{q_{eq}} \langle v_i | q_i | v_i' \rangle \right|^2 \\ &= \frac{\pi \hbar^2}{2mE} \sum_{l'\lambda',l\lambda} \left| \frac{1}{\sqrt{2}} \frac{\partial S_{l'\lambda',l\lambda}}{\partial q_i} \Big|_{q_{eq}} \right|^2 \\ &= \frac{\pi \hbar^2}{4mE} \sum_{l'\lambda',l\lambda} \left| \frac{\partial S_{l'\lambda',l\lambda}}{\partial q_i} \Big|_{q_{eq}} \right|^2. \end{aligned} \quad (\text{C.10})$$

## APPENDIX D: La synthèse

Le  $\text{NO}_2$  et le  $\text{N}_2\text{O}$  sont connus comme des polluants atmosphériques générés comme sous-produits de la combustion de combustibles fossiles, qui ont un effet délétère sur la santé humaine et l'environnement atmosphérique. De nouvelles technologies telles que le plasma hors équilibre sont prometteuses pour contrôler et détruire ces deux molécules. Les collisions de molécules électron-neutre sont les processus dominants qui se déroulent dans l'environnement du plasma hors équilibre, et qui ont donc un effet critique sur le comportement du plasma. Il est évident que les données de diffusion, y compris les sections efficaces et les constantes de vitesse, entre les molécules d'électrons et d'oxydes d'azote sont nécessaires pour développer et optimiser la technologie de dépollution du plasma.

Cette thèse présente des études théoriques sur la diffusion des électrons avec des molécules de  $\text{NO}_2$  et de  $\text{N}_2\text{O}$ . En ce qui concerne la molécule  $\text{NO}_2$ , nous étudions l'excitation vibratoire entre les niveaux les plus bas au sein des états électroniques de cette molécule. Ce processus de diffusion est important dans la modélisation cinétique du plasma. Le calcul est effectué par une approche qui combine l'approximation des modes normaux pour les états vibratoires du  $\text{NO}_2$ , le code de la UK R-matrice pour obtenir la électron-molécule S-matrice pour les géométries fixes de la cible et la « vibrational frame transformation » pour évaluer les matrices de diffusion pour les transitions vibratoires. En ce qui nous concerne, il n'existe aucune donnée théorique ou expérimentale sur l'excitation vibratoire du  $\text{NO}_2$ . Par conséquent, la section efficace d'excitation vibratoire calculée dans cette thèse est rapportée pour la première fois pour cette molécule. Les coefficients de vitesse correspondants de l'excitation vibratoire sont obtenus à partir des sections efficaces pour la plage de températures de 10K à 10000 K. Comme aucun résultat expérimental ne peut être utilisé pour la comparaison, l'estimation de l'incertitude des résultats est effectuée pour valider l'approche théorique actuelle, où l'on peut voir que les résultats calculés de l'excitation

(dé) vibratoire sont convergents. Par conséquent, les coefficients de taux peuvent être ajustés par polynôme et sont raisonnables pour une utilisation ultérieure dans la modélisation de la cinétique des plasmas contenant du  $\text{NO}_2$ .

Les sections efficaces d'excitation vibratoire de la molécule de  $\text{N}_2\text{O}$  sont déterminées dans un cadre similaire. Nous utilisons la même méthode appliquée à la molécule de  $\text{NO}_2$  pour calculer la section efficace de transition entre le sol et les premiers états vibrationnels du  $\text{N}_2\text{O}$ . Les résultats obtenus sont en accord raisonnable avec les données expérimentales. Il est donc utile d'expliquer les résultats expérimentaux. Les coefficients de vitesse d'excitation vibratoire sont également obtenus à partir des sections efficaces pour la plage de températures de 10K à 10000 K. Les coefficients de taux moyennés thermiquement sont ajustés par forme analytique pour une utilisation pratique dans la modélisation du plasma. La structure rotationnelle des molécules neutres cibles est négligée dans la présente approche, ce qui implique que les sections efficaces et les coefficients de vitesse obtenus doivent être considérés comme moyennés sur les états rotationnels initiaux et additionnés sur les états rotationnels finaux des niveaux vibrationnels initiaux et finaux correspondants. Il a été constaté que l'effet Renner-Teller non adiabatique, qui couple des ondes partielles de l'électron incident avec des vibrations de flexion dégénérées de  $\text{N}_2\text{O}$ , est responsable de l'excitation du mode de flexion. Les résultats convergents pour les propriétés cibles et les coefficients de taux démontrent la validité des résultats théoriques obtenus. L'incertitude des présents calculs est un peu plus élevée que pour le  $\text{NO}_2$ .

Enfin, l'attachement dissociatif des électrons (DEA) du  $\text{NO}_2$  est étudié dans cette thèse. Ce processus est important pour la compréhension du mécanisme de dépollution du plasma car le processus DEA est la principale voie de destruction du  $\text{NO}_2$ . Le processus DEA est en compétition avec l'excitation vibratoire dans la gamme d'énergie de diffusion en dessous du premier état d'excitation électronique de la cible. Dans ce processus, l'électron diffusant peut être capturé par la molécule cible en formant un état temporaire. Cet état est en fait un état de résonance qui se dissocie de

la molécule neutre et des fragments d'ions négatifs. La méthode utilisée pour calculer la section efficaces de la DEA du  $\text{NO}_2$  est basée sur la théorie de Bardsley-O'Malley développée pour les molécules diatomiques et généralisée aux molécules polyatomiques complexes par Chi Hong Yuen *et al.* Elle a été vérifiée en la comparant avec les mesures expérimentales disponibles. La probabilité exacte de survie est impliquée dans le présent modèle. Les sections efficaces obtenues montrent un accord qualitatif avec les résultats expérimentaux disponibles. Mais l'écart quantitatif sera réservé aux travaux futurs.

## LIST OF REFERENCES

- [1] L. Campbell and M. Brunger, “Electron collisions in atmospheres,” *International Reviews in Physical Chemistry*, vol. 35, no. 2, pp. 297–351, 2016.
- [2] R. Meier, “Ultraviolet spectroscopy and remote sensing of the upper atmosphere,” *Space Science Reviews*, vol. 58, no. 1, pp. 1–185, 1991.
- [3] A. Broadfoot, M. Belton, P. Takacs, B. Sandel, D. Shemansky, J. Holberg, J. Ajello, S. Atreya, T. Donahue, H. Moos, *et al.*, “Extreme ultraviolet observations from voyager 1 encounter with jupiter,” *Science*, vol. 204, no. 4396, pp. 979–982, 1979.
- [4] A. Broadfoot, B. Sandel, D. Shemansky, J. Holberg, G. Smith, D. Strobel, J. McConnell, S. Kumar, D. Hunten, S. Atreya, *et al.*, “Extreme ultraviolet observations from voyager 1 encounter with saturn,” *Science*, vol. 212, no. 4491, pp. 206–211, 1981.
- [5] D. L. Huestis, S. W. Bougher, J. L. Fox, M. Galand, R. E. Johnson, J. I. Moses, and J. C. Pickering, “Cross sections and reaction rates for comparative planetary aeronomy,” *Space science reviews*, vol. 139, no. 1-4, p. 63, 2008.
- [6] A. Luque, U. Ebert, and W. Hundsdorfer, “Interaction of streamer discharges in air and other oxygen-nitrogen mixtures,” *Physical review letters*, vol. 101, no. 7, p. 075005, 2008.
- [7] B. Boudaiffa, P. Cloutier, D. Hunting, M. A. Huels, and Sanche, “Resonant formation of DNA strand breaks by low-energy (3 to 20 eV) electrons,” *Science*, vol. 287, no. 5458, pp. 1658–1660, 2000.
- [8] K. Houfek *Czech. J. Phys*, vol. 52, pp. 29–40.
- [9] D. George, “Magnetohydrodynamic electrical power generation,” *At. Energy Australia*, vol. 8, no. 3, 1965.

- [10] A. J. DeMaria, "Review of CW high-power CO<sub>2</sub> lasers," *Proceedings of the IEEE*, vol. 61, no. 6, pp. 731–748, 1973.
- [11] J. Thomas, M. Kelly, J.-P. Monchalin, N. Kurnit, and A. Javan, "Stable CO<sub>2</sub> and N<sub>2</sub>O laser design," *Review of Scientific Instruments*, vol. 51, no. 2, pp. 240–243, 1980.
- [12] G. Correale, A. Rakitin, A. Nikipelov, S. Pancheshnyi, I. Popov, A. Starikovskiy, T. Shirashi, T. Urushihara, and M. Boot, "Non-equilibrium plasma ignition for internal combustion engines," tech. rep., SAE Technical Paper, 2011.
- [13] M. Kimura, "Theoretical consideration of plasma-processing processes," in *Advances In Atomic, Molecular, and Optical Physics*, vol. 44, pp. 33–57, Elsevier, 2001.
- [14] R. Springer, B. Cameron, and G. Reeves, "New methods—experimental and theoretical—to control thin film properties for target fabrication," *Fusion Technology*, vol. 31, no. 4, pp. 449–455, 1997.
- [15] G. Bird, M. Gallis, J. Torczynski, and D. Rader, "Accuracy and efficiency of the sophisticated direct simulation monte carlo algorithm for simulating noncontinuum gas flows," *Physics of Fluids*, vol. 21, no. 1, p. 017103, 2009.
- [16] V. Laporta and D. Bruno, "Electron-vibration energy exchange models in nitrogen-containing plasma flows," *The Journal of chemical physics*, vol. 138, no. 10, p. 104319, 2013.
- [17] Z. Wang, B. Li, A. Ehn, Z. Sun, Z. Li, J. Bood, M. Aldén, and K. Cen, "Investigation of flue-gas treatment with O<sub>3</sub> injection using NO and NO<sub>2</sub> planar laser-induced fluorescence," *Fuel*, vol. 89, no. 9, pp. 2346–2352, 2010.
- [18] Z. Adnan, S. Mir, and M. Habib, "Exhaust gases depletion using non-thermal plasma (NTP)," *Atmospheric Pollution Research*, vol. 8, no. 2, pp. 338–343, 2017.

- [19] P. Talebizadeh, M. Babaie, R. Brown, H. Rahimzadeh, Z. Ristovski, and M. Arai, "The role of non-thermal plasma technique in NO<sub>2</sub> treatment: A review," *Renewable and Sustainable Energy Reviews*, vol. 40, pp. 886–901, 2014.
- [20] Y.-h. Bai, J.-r. Chen, X.-y. Li, and C.-h. Zhang, "Non-thermal plasmas chemistry as a tool for environmental pollutants abatement," in *Reviews of Environmental Contamination and Toxicology Vol 201*, pp. 117–136, Springer, 2009.
- [21] N. Manivannan, W. Balachandran, R. Beleca, and M. Abbod, "Non-thermal plasma technology for the abatement of NO<sub>2</sub> and SO<sub>2</sub> from the exhaust of marine diesel engine," 2014.
- [22] R. McAdams, "Prospects for non-thermal atmospheric plasmas for pollution abatement," *Journal of Physics D: Applied Physics*, vol. 34, no. 18, p. 2810, 2001.
- [23] R. K. Srivastava, R. E. Hall, S. Khan, K. Culligan, and B. W. Lani, "Nitrogen oxides emission control options for coal-fired electric utility boilers," *Journal of the Air & Waste Management Association*, vol. 55, no. 9, pp. 1367–1388, 2005.
- [24] B. Bederson, H. Walther, and M. Inokuti, *Advances in Atomic, Molecular, and Optical Physics: Cross-Section Data*. Elsevier, 1994.
- [25] J. Nickel, P. Zetner, G. Shen, and S. Trajmar, "Principles and procedures for determining absolute differential electron-molecule (atom) scattering cross sections," *Journal of Physics E: Scientific Instruments*, vol. 22, no. 9, p. 730, 1989.
- [26] S. Buckman and B. Lohmann, "Low-energy total cross section measurements for electron scattering from helium and argon," *Journal of Physics B: Atomic and Molecular Physics*, vol. 19, no. 16, p. 2547, 1986.
- [27] L. C. Pitchford, B. V. McKoy, A. Chutjian, and S. Trajmar, *Swarm Studies and Inelastic Electron-Molecule Collisions: Proceedings of the Meeting of the Fourth International*

*Swarm Seminar and the Inelastic Electron-Molecule Collisions Symposium, July 19–23, 1985, Tahoe City, California, USA.* Springer Science & Business Media, 2012.

- [28] M. J. Brunger and S. J. Buckman, “Electron-molecule scattering cross-sections. i. experimental techniques and data for diatomic molecules,” *Physics reports*, vol. 357, no. 3-5, pp. 215–458, 2002.
- [29] C. Yuen, N. Douguet, S. F. Dos Santos, A. Orel, and V. Kokoouline, “Simplified model to treat the electron attachment of complex molecules: Application to H<sub>2</sub>CN and the quest for the CN<sup>-</sup> formation mechanism,” *Physical Review A*, vol. 99, no. 3, p. 032701, 2019.
- [30] J. Tennyson, “Electron–molecule collision calculations using the R-matrix method,” *Physics Reports*, vol. 491, no. 2-3, pp. 29–76, 2010.
- [31] J. Carr, P. Galiatsatos, J. D. Gorfinkiel, A. G. Harvey, M. Lysaght, D. Madden, Z. Mašín, M. Plummer, J. Tennyson, and H. Varambhia, “UKRmol: a low-energy electron-and positron-molecule scattering suite,” *The European Physical Journal D*, vol. 66, no. 3, p. 58, 2012.
- [32] H. B. Schlegel, “Exploring potential energy surfaces for chemical reactions: an overview of some practical methods,” *Journal of computational chemistry*, vol. 24, no. 12, pp. 1514–1527, 2003.
- [33] R. Krishnan, J. S. Binkley, R. Seeger, and J. A. Pople, “Self-consistent molecular orbital methods. XX. a basis set for correlated wave functions,” *The Journal of chemical physics*, vol. 72, no. 1, pp. 650–654, 1980.
- [34] T. H. Dunning Jr, “Gaussian basis sets for use in correlated molecular calculations. i. the atoms boron through neon and hydrogen,” *The Journal of chemical physics*, vol. 90, no. 2, pp. 1007–1023, 1989.

- [35] I. N. Levine, *Physical Chemistry*. McGraw-Hill Education, 2009.
- [36] C. C. J. Roothaan, “New developments in molecular orbital theory,” *Reviews of modern physics*, vol. 23, no. 2, p. 69, 1951.
- [37] E. Lewars, “Introduction to the theory and applications of molecular and quantum mechanics,” *Computational chemistry*, p. 318, 2003.
- [38] B. O. Roos, P. R. Taylor, and P. E. Sigbahn, “A complete active space scf method (CASSCF) using a density matrix formulated super-CI approach,” *Chemical Physics*, vol. 48, no. 2, pp. 157–173, 1980.
- [39] F. A. Cotton, *Chemical applications of group theory*. John Wiley & Sons, 2003.
- [40] D. Janežič, R. M. Venable, and B. R. Brooks, “Harmonic analysis of large systems. iii. comparison with molecular dynamics,” *Journal of Computational Chemistry*, vol. 16, no. 12, pp. 1554–1566, 1995.
- [41] E. B. Wilson, “JC Decius, and PC Cross, Molecular Vibrations,” *The Theory of Infrared and Raman Vibrational Spectra*. McGraw-Hill, New York, 1955.
- [42] H.-J. Werner, P. J. Knowles, G. Knizia, F. R. Manby, and M. Schütz, “Molpro: a general-purpose quantum chemistry program package,” *Wiley Interdisciplinary Reviews: Computational Molecular Science*, vol. 2, no. 2, pp. 242–253, 2012.
- [43] <http://www.molpro.net>.
- [44] H. Werner and P. Knowles, “Users Manual Version 2019.2,” *Chem. Phys*, vol. 135, p. 054101, 2011.
- [45] E. Lifshitz, LD, and S. L. (JB), *Quantum Mechanics; Non-relativistic Theory*. Pergamon Press, 1965.

- [46] D. J. Griffiths and D. F. Schroeter, *Introduction to quantum mechanics*. Cambridge University Press, 2018.
- [47] B. Schneider and T. Rescigno, “Complex Kohn variational method: Application to low-energy electron-molecule collisions,” *Physical Review A*, vol. 37, no. 10, p. 3749, 1988.
- [48] D. Watson, R. Lucchese, V. McKoy, and T. Rescigno, “Schwinger variational principle for electron-molecule scattering: Application to electron-hydrogen scattering,” *Physical Review A*, vol. 21, no. 3, p. 738, 1980.
- [49] L. Leal, “Brief review of the r-matrix theory,” 2010.
- [50] P. G. Burke, *R-matrix theory of atomic collisions: Application to atomic, molecular and optical processes*, vol. 61. Springer Science & Business Media, 2011.
- [51] E. P. Wigner, “Resonance reactions,” *Physical Review*, vol. 70, no. 9-10, p. 606, 1946.
- [52] E. P. Wigner and L. Eisenbud, “Higher angular momenta and long range interaction in resonance reactions,” *Physical Review*, vol. 72, no. 1, p. 29, 1947.
- [53] P. Burke, A. Hibbert, and W. Robb, “Electron scattering by complex atoms,” *Journal of Physics B: Atomic and Molecular Physics*, vol. 4, no. 2, p. 153, 1971.
- [54] W. Robb, “The use of the R-matrix method in atomic calculations,” *Computer Physics Communications*, vol. 4, no. 1, pp. 16–19, 1972.
- [55] P. Burke, “The R-matrix method in atomic physics,” *Computer Physics Communications*, vol. 6, no. 6, pp. 288–302, 1973.
- [56] B. Schneider, “R-matrix theory for electron-atom and electron-molecule collisions using analytic basis set expansions,” *Chemical Physics Letters*, vol. 31, no. 2, pp. 237–241, 1975.

- [57] “Elastic scattering of electrons from F<sub>2</sub>: An R-matrix calculation, author=Schneider, BI and Hay, PJ, journal=Physical Review A, volume=13, number=6, pages=2049, year=1976, publisher=APS,”
- [58] P. Burke, I. Mackey, and I. Shimamura, “R-matrix theory of electron-molecule scattering,” *Journal of Physics B: Atomic and Molecular Physics*, vol. 10, no. 12, p. 2497, 1977.
- [59] B. M. Nestmann, K. Pfingst, and S. D. Peyerimhoff, “R-matrix calculation for electron-methane scattering cross sections,” *Journal of Physics B: Atomic, Molecular and Optical Physics*, vol. 27, no. 11, p. 2297, 1994.
- [60] L. Morgan, C. Gillan, J. Tennyson, and X. Chen, “R-matrix calculations for polyatomic molecules: electron scattering by N<sub>2</sub>O,” *Journal of Physics B: Atomic, Molecular and Optical Physics*, vol. 30, no. 18, p. 4087, 1997.
- [61] L. A. Morgan, J. Tennyson, and C. J. Gillan, “The UK molecular R-matrix codes,” *Computer physics communications*, vol. 114, no. 1-3, pp. 120–128, 1998.
- [62] P. Burke\* and J. Tennyson, “R-matrix theory of electron molecule scattering,” *Molecular Physics*, vol. 103, no. 18, pp. 2537–2548, 2005.
- [63] C. Bloch, “Une formulation unifiée de la théorie des réactions nucléaires,” *Nuclear Physics*, vol. 4, pp. 503–528, 1957.
- [64] A. Arthurs and A. Dalgarno, “The theory of scattering by a rigid rotator,” *Proceedings of the Royal Society of London. Series A. Mathematical and Physical Sciences*, vol. 256, no. 1287, pp. 540–551, 1960.
- [65] A. Faure, J. D. Gorfinkiel, L. A. Morgan, and J. Tennyson, “GTOBAS: fitting continuum functions with Gaussian-type orbitals,” *Computer physics communications*, vol. 144, no. 2, pp. 224–241, 2002.

- [66] C. Gillan, J. Tennyson, and P. Burke, "Computational methods for electron-molecule collisions ed FA gianturco and WM huo," 1995.
- [67] M. Gailitis, "New forms of asymptotic expansions for wavefunctions of charged-particle scattering," *Journal of Physics B: Atomic and Molecular Physics*, vol. 9, no. 5, p. 843, 1976.
- [68] C. Noble and R. Nesbet, "CFASYM, a program for the calculation of the asymptotic solutions of the coupled equations of electron collision theory," 1984.
- [69] K. Baluja, P. Burke, and L. Morgan, "R-matrix propagation program for solving coupled second-order differential equations," *Computer Physics Communications*, vol. 27, no. 3, pp. 299–307, 1982.
- [70] L. A. Morgan, "A generalized R-matrix propagation program for solving coupled second-order differential equations," 1984.
- [71] J. Tennyson, D. B. Brown, J. J. Munro, I. Rozum, H. N. Varambhia, and N. Vinci, "Quantemol-N: an expert system for performing electron molecule collision calculations using the R-matrix method," in *Journal of Physics: Conference Series*, vol. 86, p. 012001, IOP Publishing, 2007.
- [72] O. Atabek, D. Dill, and C. Jungen, "Quantum-defect theory of excited  $\pi$  u 1- levels of h 2," *Physical Review Letters*, vol. 33, no. 3, p. 123, 1974.
- [73] U. Fano, "Unified treatment of perturbed series, continuous spectra and collisions," *JOSA*, vol. 65, no. 9, pp. 979–987, 1975.
- [74] C. Jungen and O. Atabek, "Rovibronic interactions in the photoabsorption spectrum of molecular hydrogen and deuterium: An application of multichannel quantum defect methods," *The Journal of Chemical Physics*, vol. 66, no. 12, pp. 5584–5609, 1977.

- [75] M. Ayouz and V. Kokoouline, “Cross sections and rate coefficients for vibrational excitation of  $\text{HeH}^+$  molecule by electron impact,” *Atoms*, vol. 4, no. 4, p. 30, 2016.
- [76] C. Greene, U. Fano, and G. Strinati, “General form of the quantum-defect theory,” *Physical Review A*, vol. 19, no. 4, p. 1485, 1979.
- [77] C. H. Greene, A. Rau, and U. Fano, “General form of the quantum-defect theory. ii,” *Physical Review A*, vol. 26, no. 5, p. 2441, 1982.
- [78] C. H. Greene and C. Jungen, “Molecular applications of quantum defect theory,” in *Advances in atomic and molecular physics*, vol. 21, pp. 51–121, Elsevier, 1985.
- [79] H. Liu, S. F. dos Santos, C. H. Yuen, P. Cortona, V. Kokoouline, and M. Ayouz, “Theoretical study of electron-induced vibrational excitation of  $\text{NO}_2$ ,” *Plasma Sources Science and Technology*, vol. 28, no. 10, p. 105017, 2019.
- [80] M. Shomali, D. Opie, T. Avasthi, and A. Trilling, “Nitrogen dioxide sterilization in low-resource environments: A feasibility study,” *PLoS One*, vol. 10, no. 6, p. e0130043, 2015.
- [81] P. Clough and B. A. Thrush, “Mechanism of chemiluminescent reaction between nitric oxide and ozone,” *Transactions of the Faraday Society*, vol. 63, pp. 915–925, 1967.
- [82] J. A. Bernstein, N. Alexis, C. Barnes, I. L. Bernstein, A. Nel, D. Peden, D. Diaz-Sanchez, S. M. Tarlo, and P. B. Williams, “Health effects of air pollution,” *Journal of allergy and clinical immunology*, vol. 114, no. 5, pp. 1116–1123, 2004.
- [83] J. Collin, “Ionization and dissociation of molecules by monoenergetic electrons. iii. on the existence of a bent excited state of  $\text{NO}_2^+$ ,” *The Journal of Chemical Physics*, vol. 30, no. 6, pp. 1621–1621, 1959.
- [84] R. W. Kiser and I. Hisatsune, “Electron impact spectroscopy of nitrogen dioxide1,” *The Journal of Physical Chemistry*, vol. 65, no. 8, pp. 1444–1446, 1961.

- [85] K. Stephan, H. Helm, Y. Kim, G. Seykora, J. Ramler, M. Grössl, E. Märk, and T. Märk, “Single and double ionization of nitrogen dioxide by electron impact from threshold up to 180 eV,” *The Journal of Chemical Physics*, vol. 73, no. 1, pp. 303–308, 1980.
- [86] C. Szmytkowski, K. Maciag, and A. Krzysztofowicz, “NO<sub>2</sub> total absolute electron-scattering cross sections,” *Chemical physics letters*, vol. 190, no. 1-2, pp. 141–144, 1992.
- [87] A. Zecca, R. Melissa, R. S. Brusa, and G. P. Karwasz, “Additivity rule for electron-molecule cross section calculation: A geometrical approach,” *Physics Letters A*, vol. 257, no. 1-2, pp. 75–82, 1999.
- [88] R. Fox, “Negative ion formation in NO<sub>2</sub> by electron attachment,” *The Journal of Chemical Physics*, vol. 32, no. 1, pp. 285–287, 1960.
- [89] S. A. Rangwala, E. Krishnakumar, and S. Kumar, “Dissociative-electron-attachment cross sections: A comparative study of NO<sub>2</sub> and O<sub>3</sub>,” *Physical Review A*, vol. 68, no. 5, p. 052710, 2003.
- [90] H. Munjal, K. Baluja, and J. Tennyson, “Electron collisions with the NO<sub>2</sub> radical using the R-matrix method,” *Physical Review A*, vol. 79, no. 3, p. 032712, 2009.
- [91] N. Mason, W. Johnstone, and P. Akther in *Electron Collisions with Molecules, Clusters, and Surfaces*, pp. 47–62, Springer, 1994.
- [92] C. Benoit and R. Abouaf, “Vibrational excitation in  $e^-$ -NO<sub>2</sub> collision at low energy (0.3-2.5 eV),” *Chemical physics letters*, vol. 177, no. 6, pp. 573–578, 1991.
- [93] H. Chung, B. Braams, K. Bartschat, A. Császár, G. Drake, T. Kirchner, V. Kokoouline, and J. Tennyson, “Uncertainty estimates for theoretical atomic and molecular data,” *Journal of Physics D: Applied Physics*, vol. 49, no. 36, p. 363002, 2016.

- [94] R. D. Johnson III, “NIST computational chemistry comparison and benchmark database, NIST standard reference database number 101,” *NIST, Gaithersburg, MD*, 2010.
- [95] J. Liévin, A. Delon, and R. Jost, “Absorption cross section of NO<sub>2</sub> by the reflection method from ab initio calculations involving the three low lying electronic states,” *The Journal of chemical physics*, vol. 108, no. 21, pp. 8931–8943, 1998.
- [96] V. Kokoouline, A. Faure, J. Tennyson, and C. H. Greene, “Calculation of rate constants for vibrational and rotational excitation of the H<sub>3</sub><sup>+</sup> ion by electron impact,” *Mon. Not. R. Astron. Soc.*, vol. 405, no. 2, pp. 1195–1202, 2010.
- [97] N. Douguet, V. Kokoouline, and C. H. Greene, “Theory of dissociative recombination of a linear triatomic ion with permanent electric dipole moment: Study of hco+,” *Physical Review A*, vol. 80, no. 6, p. 062712, 2009.
- [98] [https://en.wikipedia.org/wiki/Table\\_of\\_spherical\\_harmonics](https://en.wikipedia.org/wiki/Table_of_spherical_harmonics).
- [99] L. D. Landau and E. M. Lifshitz, *Quantum mechanics: non-relativistic theory*, vol. 3. Elsevier, 2013.
- [100] [http://www-stone.ch.cam.ac.uk/cgi-bin/wigner.cgi?symbol=3j&j1=0&j2=1&j3=1&m1=0&m2=0&m3=0/en.wikipedia.org/wiki/Table\\_of\\_spherical\\_harmonics](http://www-stone.ch.cam.ac.uk/cgi-bin/wigner.cgi?symbol=3j&j1=0&j2=1&j3=1&m1=0&m2=0&m3=0/en.wikipedia.org/wiki/Table_of_spherical_harmonics).
- [101] H. Liu, S. F. dos Santos, C. H. Yuen, P. Cortona, M. Ayouz, and V. Kokoouline, “Vibrational excitation of n 2 o by an electron impact and the role of the renner-teller effect in the process,” *Physical Review A*, vol. 102, no. 3, p. 032808, 2020.
- [102] L. M. Ziurys, A. Apponi, J. Hollis, and L. Snyder, “Detection of interstellar N<sub>2</sub>O: A new molecule containing an NO bond,” *The Astrophysical Journal*, vol. 436, pp. L181–L184, 1994.

- [103] C. S. Jamieson, C. J. Bennett, A. M. Mebel, and R. I. Kaiser, "Investigating the mechanism for the formation of nitrous oxide  $\text{N}_2\text{O}$  ( $X1\Sigma^+$ ) in extraterrestrial ices," *The Astrophysical Journal*, vol. 624, no. 1, p. 436, 2005.
- [104] W.-C. Wang and N. D. Sze, "Coupled effects of atmospheric  $\text{N}_2\text{O}$  and  $\text{O}_3$  on the Earth's climate," *Nature*, vol. 286, no. 5773, pp. 589–590, 1980.
- [105] N. Gherardi, S. Martin, and F. Massines, "A new approach to  $\text{SiO}_2$  deposit using a  $\text{N}_2$ - $\text{SiH}_4$ - $\text{N}_2\text{O}$  glow dielectric barrier-controlled discharge at atmospheric pressure," *Journal of Physics D: Applied Physics*, vol. 33, no. 19, p. L104, 2000.
- [106] Í. O'Sullivan and J. Benger, "Nitrous oxide in emergency medicine," *Emergency medicine journal*, vol. 20, no. 3, pp. 214–217, 2003.
- [107] A. Zecca, I. Lazzizzera, M. Krauss, and C. Kuyatt, "Electron scattering from  $\text{NO}$  and  $\text{N}_2\text{O}$  below 10 eV," *The Journal of Chemical Physics*, vol. 61, no. 11, pp. 4560–4566, 1974.
- [108] R. I. Hall, A. Chutjian, and S. Trajmar, "Electron impact excitation and assignment of the low-lying electronic states of  $\text{N}_2\text{O}$ ," *J. Phys. B: At. Mol. Opt. Phys.*, vol. 6, 01 1974.
- [109] E. Märk, T. D. Märk, Y. B. Kim, and K. Stephan, "Absolute electron impact ionization cross section from threshold up to 180 eV for  $\text{N}_2\text{O}+e^- \rightarrow \text{N}_2\text{O}^++2e^-$  and the metastable and collision induced dissociation of  $\text{N}_2\text{O}^+$ ," *J. Chem. Phys.*, vol. 75, no. 9, p. 4446, 1981.
- [110] C. K. Kwan, Y.-F. Hsieh, W. Kauppila, S. J. Smith, T. Stein, M. Uddin, and M. Dababneh, "Total-scattering measurements and comparisons for collisions of electrons and positrons with  $\text{N}_2\text{O}$ ," *Physical review letters*, vol. 52, no. 16, p. 1417, 1984.
- [111] C. Szmytkowski, G. Karwasz, and K. Maciag, "Absolute total electron-scattering cross sections of  $\text{N}_2\text{O}$  and  $\text{OCS}$  in the low-energy region," *Chemical physics letters*, vol. 107, pp. 481–484, 1984.

- [112] L. Andric and R. Hall, "Vibrational excitation of N<sub>2</sub>O by electron impact via resonant processes in the 2 eV region: an angular study," *Journal of Physics B: Atomic and Molecular Physics*, vol. 17, no. 13, p. 2713, 1984.
- [113] D. Cubric, D. Cvejanovic, J. Jureta, S. Cvejanovic, P. Hammond, G. C. King, and F. H. Read, "Threshold electron impact spectrum of N<sub>2</sub>O," *J. Phys. B: At. Mol. Phys.*, vol. 19, pp. 4225–4239, dec 1986.
- [114] B. Marinkovic, C. Szmytkowski, V. Pejcev, D. Filipovic, and L. Vuskovic, "Differential cross sections for elastic and inelastic scattering of electrons by N<sub>2</sub>O in the range from 10 to 80 eV," *Journal of Physics B: Atomic and Molecular Physics*, vol. 19, no. 15, p. 2365, 1986.
- [115] W. Johnstone and W. Newell, "Absolute elastic cross sections for electron scattering from N<sub>2</sub>O," *Journal of Physics B: Atomic, Molecular and Optical Physics*, vol. 26, no. 1, p. 129, 1993.
- [116] A. Zecca, J. C. Nogueira, G. P. Karwasz, and R. S. Brusa, "Total cross sections for electron scattering on NO<sub>2</sub>, OCS, SO<sub>2</sub> at intermediate energies," *J. Phys. B: At. Mol. Opt. Phys.*, vol. 28, no. 3, p. 477, 1995.
- [117] I. Iga, M. V. V. S. Rao, and S. K. Srivastava, "Absolute electron impact ionization cross sections for N<sub>2</sub>O and NO from threshold up to 1000 eV," *J. Geophys. Res. E*, vol. 101, no. E4, p. 9261, 1996.
- [118] M. Kitajima, Y. Sakamoto, S. Watanabe, T. Suzuki, T. Ishikawa, H. Tanaka, and M. Kimura, "Absolute elastic differential cross-sections for electron scattering by N<sub>2</sub>O at 1.5–100 eV," *Chem. Phys. Letts.*, vol. 309, no. 5, pp. 414 – 420, 1999.

- [119] M. Kitajima, Y. Sakamoto, R. J. Gulley, M. Hoshino, J. C. Gibson, H. Tanaka, and S. J. Buckman, "Electron scattering from N<sub>2</sub>O: absolute elastic scattering and vibrational excitation," *J. Phys. B: At., Mol. Opt. Phys.*, vol. 33, no. 9, p. 1687, 2000.
- [120] A. Zecca, G. P. Karwasz, R. S. Brusa, and T. Wroblewski, "Low-energy electron collisions in nitrogen oxides: a comparative study," *Int. J. Mass Spectrom.*, vol. 223-224, p. 205, 2003.
- [121] M. Allan and T. Skalický, "Structures in elastic, vibrational, and dissociative electron attachment cross sections in N<sub>2</sub>O near threshold," *Journal of Physics B: Atomic, Molecular and Optical Physics*, vol. 36, no. 16, p. 3397, 2003.
- [122] Y. Nakamura, "Electron swarm parameters in pure N<sub>2</sub>O and in dilute N<sub>2</sub>O-Ar mixtures and electron collision cross sections of N<sub>2</sub>O molecule," *Proc. of the 28th ICPIG*, pp. 224–6, 2007.
- [123] H. Kawahara, D. Suzuki, H. Kato, M. Hoshino, H. Tanaka, O. Ingólfsson, L. Campbell, and M. J. Brunger, "Cross sections for electron impact excitation of the C<sup>1</sup>Π and D<sup>1</sup>Σ<sup>+</sup> electronic states in N<sub>2</sub>O," *J. Chem. Phys.*, vol. 131, 09 2009.
- [124] Y. Itikawa, "Momentum-transfer cross sections for electron collisions with atoms and molecules," *At. Data Nucl. Data Tables*, vol. 14, no. 1, pp. 1 – 10, 1974.
- [125] M. Kumar, Y. Kumar Kumar, N. Tiwari, and S. Tomar, "Total ionization cross sections of NO<sub>2</sub>, CO and CS molecules due to electron impact," *J. At. Mol. Sci.*, vol. 4, p. 30, 02 2013.
- [126] D. Nandi, V. S. Prabhudesai, and E. Krishnakumar, "Dissociative electron attachment to N<sub>2</sub>O using velocity slice imaging," *Phys. Chem. Chem. Phys.*, vol. 16, pp. 3955–3963, 2014.
- [127] B. K. Sarpal, K. Pfingst, B. M. Nestmann, and S. D. Peyerimhoff, "Study of electron scattering by using the polyatomic R-matrix method," *Journal of Physics B: Atomic, Molecular and Optical Physics*, vol. 29, no. 4, p. 857, 1996.

- [128] M. Bettega, C. Winstead, and V. McKoy, "Low-energy electron scattering by  $\text{N}_2\text{O}$ ," *Physical Review A*, vol. 74, no. 2, p. 022711, 2006.
- [129] M. Hayashi and K. Akashi, "Handbook of plasma material science," 1992.
- [130] M.-Y. Song, J.-S. Yoon, H. Cho, G. P. Karwasz, V. Kokoouline, Y. Nakamura, and J. Tenynson, "Cross sections for electron collisions with  $\text{NO}$ ,  $\text{N}_2\text{O}$ , and  $\text{NO}_2$ ," *J. Phys. Chem. Ref. Data*, vol. 48, no. 4, p. 043104, 2019.
- [131] S. Fonseca dos Santos, N. Douguet, V. Kokoouline, and A. Orel, "Scattering matrix approach to the dissociative recombination of  $\text{HCO}^+$  and  $\text{N}_2\text{H}^+$ ," *The Journal of chemical physics*, vol. 140, no. 16, p. 164308, 2014.
- [132] V. Kokoouline, M. Ayouz, J. Z. Mezei, K. Hassouni, and I. F. Schneider, "Theoretical study of dissociative recombination and vibrational excitation of the ion by an electron impact," *Plasma Sources Science and Technology*, vol. 27, no. 11, p. 115007, 2018.
- [133] G. Herzberg, *Electronic spectra and electronic structure of polyatomic molecules*, vol. 2. Krieger Publishing Company, 1991.
- [134] R. A. Kendall, T. H. Dunning Jr, and R. J. Harrison, "Electron affinities of the first-row atoms revisited. Systematic basis sets and wave functions," *J. Chem. Phys.*, vol. 96, no. 9, pp. 6796–6806, 1992.
- [135] A. Moradmand, A. Landers, and M. Fogle, "Momentum imaging of dissociative electron attachment to  $\text{n}_2\text{o}$  at the 2.3-eV shape resonance," *Phys. Rev. A*, vol. 88, no. 1, p. 012713, 2013.
- [136] I. A. Mikhaylov, V. Kokoouline, A. Larson, S. Tonzani, and C. H. Greene, "Renner-Teller effects in  $\text{HCO}^+$  dissociative recombination," *Phys. Rev. A*, vol. 74, p. 032707, 2006.

- [137] N. Douguet, V. Kokoouline, and C. H. Greene, “Theoretical rate of dissociative recombination of  $\text{HCO}^+$  and  $\text{DCO}^+$  ions,” *Phys. Rev. A*, vol. 77, p. 064703, 2008.
- [138] N. Douguet, V. Kokoouline, and C. H. Greene, “Theory of dissociative recombination of a linear triatomic ion with permanent electric dipole moment: Study of  $\text{HCO}^+$ ,” *Phys. Rev. A*, vol. 80, p. 062712, 2009.
- [139] N. Douguet, A. Orel, I. Mikhailov, I. F. Schneider, C. H. Greene, and V. Kokoouline, “The role of the Jahn-Teller coupling in dissociative recombination of  $\text{H}_3\text{O}^+$  and  $\text{H}_3^+$  ions,” *J. Phys. Conf. Ser.*, vol. 300, no. 1, p. 012015, 2011.
- [140] N. Douguet, S. Fonseca dos Santos, V. Kokoouline, and A. Orel, “Simplified model to describe the dissociative recombination of linear polyatomic ions of astrophysical interest,” *EPJ Web Conf.*, vol. 84, p. 07003, 2015.
- [141] D. G. Hopper, A. C. Wahl, R. L. Wu, and T. O. Tiernan, “Theoretical and experimental studies of the  $n2o^-$  and  $n2o$  ground state potential energy surfaces. implications for the  $o^- + n2 \rightarrow n2o + e$  and other processes,” *J. Chem. Phys.*, vol. 65, no. 12, pp. 5474–5494, 1976.
- [142] G. S. Tschumper and H. F. Schaefer III, “Predicting electron affinities with density functional theory: Some positive results for negative ions,” *J. Chem. Phys.*, vol. 107, no. 7, pp. 2529–2541, 1997.
- [143] H. Hotop, M.-W. Ruf, M. Allan, and I. Fabrikant, “Resonance and threshold phenomena in low-energy electron collisions with molecules and clusters,” in *Advances in atomic, molecular, and optical physics*, vol. 49, pp. 85–216, Elsevier, 2003.
- [144] I. I. Fabrikant, S. Eden, N. J. Mason, and J. Fedor, “Recent progress in dissociative electron attachment: from diatomics to biomolecules,” in *Advances in atomic, molecular, and optical physics*, vol. 66, pp. 545–657, Elsevier, 2017.

- [145] O. May, J. Fedor, and M. Allan, "Isotope effect in dissociative electron attachment to acetylene," *Physical Review A*, vol. 80, no. 1, p. 012706, 2009.
- [146] E. Krishnakumar, S. Kumar, S. Rangwala, and S. Mitra, "Dissociative-attachment cross sections for excited and ground electronic states of SO<sub>2</sub>," *Physical Review A*, vol. 56, no. 3, p. 1945, 1997.
- [147] D. Nandi, V. S. Prabhudesai, E. Krishnakumar, and A. Chatterjee, "Velocity slice imaging for dissociative electron attachment," *Review of scientific instruments*, vol. 76, no. 5, p. 053107, 2005.
- [148] D. Rallis and J. Goodings, "Dissociative electron attachment processes in SO<sub>2</sub> and NO<sub>2</sub>," *Canadian Journal of Chemistry*, vol. 49, no. 9, pp. 1571–1574, 1971.
- [149] R. Abouaf and F. Fiquet-Fayard, "Dissociative attachment in SO<sub>2</sub> and OCS: evidence for vibrational excitation of the SO, O<sub>2</sub> and CO fragments," *Journal of Physics B: Atomic and Molecular Physics*, vol. 9, no. 11, p. L323, 1976.
- [150] J. J. Munro, S. Harrison, M. M. Fujimoto, and J. Tennyson, "A dissociative electron attachment cross-section estimator," in *J. Phys. Conf. Ser.*, vol. 388, p. 012013, 2012.
- [151] R. Abouaf, R. Paineau, and F. Fiquet-Fayard, "Dissociative attachment in NO<sub>2</sub> and CO<sub>2</sub>," *Journal of Physics B: Atomic and Molecular Physics*, vol. 9, no. 2, p. 303, 1976.
- [152] J. Bardsley, "The theory of dissociative recombination," *Journal of Physics B: Atomic and Molecular Physics*, vol. 1, no. 3, p. 365, 1968.
- [153] J. Bardsley, "Configuration interaction in the continuum states of molecules," *Journal of Physics B: Atomic and Molecular Physics*, vol. 1, no. 3, p. 349, 1968.
- [154] J. Bardsley and M. Biondi, "Dissociative recombination," in *Advances in Atomic and Molecular Physics*, vol. 6, pp. 1–57, Elsevier, 1970.

- [155] T. F. O'Malley, "Theory of dissociative attachment," *Physical Review*, vol. 150, no. 1, p. 14, 1966.
- [156] J. Bardsley, A. Herzenberg, and F. Mandl, "Vibrational excitation and dissociative attachment in the scattering of electrons by hydrogen molecules," *Proceedings of the Physical Society*, vol. 89, no. 2, p. 321, 1966.
- [157] J. C. Chen, "Dissociative attachment in rearrangement electron collision with molecules," *Physical Review*, vol. 148, no. 1, p. 66, 1966.
- [158] X. Jiang, C. H. Yuen, P. Cortona, M. Ayouz, and V. Kokoouline, "Cross sections for vibronic excitation of  $\text{CH}^+$  by low-energy electron impact," *Physical Review A*, vol. 100, no. 6, p. 062711, 2019.
- [159] B. P. Pritchard, D. Altarawy, B. Didier, T. D. Gibson, and T. L. Windus, "New basis set exchange: An open, up-to-date resource for the molecular sciences community," *Journal of chemical information and modeling*, vol. 59, no. 11, pp. 4814–4820, 2019.

**Titre:** Etude théorique des collisions d'électrons avec les molécules de NO<sub>2</sub> et N<sub>2</sub>O pour le contrôle et la réduction de la pollution atmosphérique

**Mots clés:** Méthode R-matrix, Diffusion d'électrons-NO<sub>x</sub>, Transformation du cadre vibratoire, excitation vibrationnelle, Attachement dissociatif d'électrons

**Résumé:** Cette thèse présente des recherches théoriques sur la diffusion électronique avec deux molécules polyatomiques d'intérêt pour la pollution atmosphérique, les molécules NO<sub>2</sub> et N<sub>2</sub>O. En ce qui concerne la molécule NO<sub>2</sub>, nous étudions l'excitation vibrationnelle entre les niveaux les plus bas des états électroniques fondamentaux de cette molécule. Le calcul est effectué par une approche qui combine l'approximation des modes normaux pour les états vibrationnels du NO<sub>2</sub>, le code de la UK R-matrice pour obtenir la électron-molécule S-matrice pour les géométries fixes de la cible et la « vibrational frame transformation » pour évaluer les matrices de diffusion pour les transitions vibrationnelles. En ce qui nous concerne, les sections efficaces d'excitation vibrationnelle calculées dans cette thèse est rapportée pour la première fois pour la molécule NO<sub>2</sub>. L'estimation de l'incertitude des résultats est ainsi réalisée pour valider la présente approche théorique.

De même, les sections efficaces d'excitation vibrationnelle de la molécule de N<sub>2</sub>O sont déterminées. Les résultats obtenus sont en accord raisonnable avec les données expérimentales. Les rate coeffi-

cient d'excitation vibrationnelle sont obtenus à partir des sections efficaces pour la plage de températures de 10K à 10000 K. La structure rotationnelle des molécules neutres cibles est négligée dans la présente approche, ce qui implique que les sections efficaces et les rate coefficient obtenus doivent être considérés comme une moyenne sur états de rotation initiaux et additionnés sur les états de rotation finaux des niveaux vibrationnels initial et final correspondants.

Enfin, l'attachement dissociatif aux électrons (DEA) du NO<sub>2</sub> est également étudié dans cette thèse. Ce processus est en concurrence avec l'excitation vibrationnelle dans la plage d'énergie de diffusion en dessous du premier état électronique excité de la cible. La DEA sections efficaces est calculée par la méthode basée sur la théorie de Bardsley-O'Malley développée pour les molécules diatomiques et généralisée aux molécules polyatomiques complexes par Chi Hong Yuen *et al.* par la suite par rapport aux mesures expérimentales disponibles. Les résultats obtenus pourraient être utilisés dans la modélisation du plasma pour le contrôle et la réduction de la pollution atmosphérique.

**Title:** Theoretical study of electron collisions with NO<sub>2</sub> and N<sub>2</sub>O molecules for control and reduction of atmospheric pollution

**Keywords:** R-matrix method, Electron-NO<sub>x</sub> scattering, Vibrational frame transformation, Vibrational excitation, Dissociative electron attachment

**Abstract:** This thesis presents theoretical investigations on electron scattering with two polyatomic molecules of atmospheric pollution interest, the NO<sub>2</sub> and N<sub>2</sub>O molecules. Regarding the NO<sub>2</sub> molecule, we study the vibrational excitation between the lowest levels within the ground electronic states of this molecule. The calculation is carried out by an approach that combines the normal modes approximation for the vibrational states of the NO<sub>2</sub>, the UK R-matrix code to obtain electron-molecule S-matrix for fixed geometries of the target and the vibrational frame transformation to evaluate the scattering matrices for vibrational transitions. To our knowledge, the vibrational excitation cross section calculated in this thesis is reported for the first time for NO<sub>2</sub> molecule. The uncertainty estimation of the results is thus performed to validate the present theoretical approach.

Similarly, the vibrational excitation cross sections of N<sub>2</sub>O molecule are determined. The obtained results are in reasonable agreement with experimen-

tal data. The rate coefficient of vibrational excitation are obtained from the cross-sections for temperatures in the 10–10000 K range. The rotational structure of the target neutral molecules is neglected in the present approach, which implies that the obtained cross-sections and rate coefficients should be viewed as averaged over initial rotational states and summed over final rotational states of the corresponding initial and final vibrational levels.

Finally, the dissociative electron attachment (DEA) of NO<sub>2</sub> are also studied in this thesis. This process competes with vibrational excitation at the scattering energy range below the first electronic excited state of the target. The DEA cross section is calculated by the method based on the Bardsley-O'Malley theory developed for diatomic molecules and generalized to complex polyatomic molecules by Chi Hong Yuen *et al.* afterwards compared with available experimental measurements. The obtained results could be used in plasma modeling for control and reduction of atmospheric pollution.

